UNIVERSITAT POLITÈCNICA DE CATALUNYA BARCELONATECH

Mesoporous material systems for catalysis and drug delivery

Aylin Atakan

Linköping Studies in Science and Technology
Dissertation No. 1927

Mesoporous material systems for catalysis and drug delivery

Aylin Atakan

Nanostructured Materials Group
Department of Physics, Chemistry and Biology (IFM)
Linköping University
SE-581 83 Linköping, Sweden.

Biomaterials, Biomechanics and Tissue Engineering Group
Department of Materials Science and Metallurgical Engineering
Universitat Politécnica de Catalunya
08034 Barcelona, Spain.

Part of

The Joint European Doctoral Programme in Materials Science and Engineering (DocMASE)

Linköping 2018

Thesis Supervisors

Prof. Maria Pau Ginebra, Universitat Politècnica de Catalunya, Barcelona, Spain

Dr. Cristina Canal, Universitat Politècnica de Catalunya, Barcelona, Spain

Prof. Magnus Odén, Linköping University, Linköping, Sweden

Printed in Sweden by LIU-Tryck, Linköping 2018

ISSN 0345-7524

ISBN 978-91-7685-330-6

Abstract

Hybrid material systems possess multi-functional properties which make them intriguing for the materials science community since very early dates. However, it is not straightforward to produce such material systems. A smart and efficient approach is necessary to extract the desired properties of each component under the desired conditions. This study evolved to its last form primarily around this notion, where the development of a hybrid material is the core of the work. This hybrid material is then further explored for two different applications in the catalysis and drug delivery fields.

A nanoassembly was established around a mesoporous silica support. SBA-15 was picked as this support among the other mesoporous silica due to its well-defined pore structure and accessible pore volume. The silica framework was doped with Zr atoms and the pores were partly infiltrated with Cu nanoparticles resulting in a hybrid material with tunable properties. SBA-15 was synthesized by a sol-gel method where a micellar solution was employed as a template for the silica framework. To achieve the doped version, a Zr precursor was added to the synthesis solution. The effects of different synthesis conditions, such as the synthesis catalyst (F^- or a Cl^- salt) and the Si source (tetraethyl orthosilicate (TEOS) or sodium metasilicate (SMS)) on the characteristics of the final material were investigated. It was observed that these changes in the synthesis conditions yielded different particle morphology, pore size (11-15 nm), and specific surface area (400-700 m^2/g). Cu nanoparticles (NPs) were grown in the (Zr-)SBA-15 support using infiltration (Inf) or evaporation induced wetness impregnation (EIWI) methods. The infiltration method is based on functionalizing the (Zr-)SBA-15 support surfaces before the Cu ion attachment whereas EIWI is based on slow evaporation of the liquid from the (Zr-)SBA-15 - Cu aqueous suspension. Both methods are designed to yield preferential growth of Cu NPs in the pores with a diameter smaller than 10 nm and in oxidized form. However, depending on the loading method used, different chemical states of the final material were achieved, i.e. Zr content and porous network properties are different.

Cu-Zr-SBA-15 nanoassemblies produced under various synthesis conditions were used for the catalytic conversion of CO_2 into valuable fuels such as methanol and dimethyl ether (DME). The effect of different chemical states of the catalyst arising from variations in the synthesis parameters was investigated. It was found that the Si precursor (TEOS or SMS) had a considerable impact on the overall performance of the catalyst whereas the Cu

loading method (Inf or EIWI) changed the catalytic selectivity between DME and methanol. The activity of the catalyst was further investigated in a time-evolution study where the accumulation of each product in the gas phase and the molecular groups attached to the catalyst surface were recorded over time. Accordingly, thermodynamic equilibrium was achieved on the 14th day of the reaction under 250°C and 33 bar. The resulting total CO_2 conversion was 24%, which is the thermodynamically highest possible conversion, according to theoretical calculations. It was also concluded from the experimental results that, DME is formed by a combination of two methoxy surface groups. Additionally, the formation of DME boosts the total CO_2 conversion to fuels, which otherwise is limited to 9.5%.

The design of Cu-Zr-SBA-15 was also investigated for drug delivery applications, due to its potential as a biomaterial, e.g., a filler in dental composites, and the antibacterial properties of Cu. Also, the bioactivity of SiO_2 and ZrO_2 was considered to be an advantage. With this aim, Cu infiltrated Zr doped SBA-15 material was prepared by using TEOS as the silica precursor and the Inf-method to grow Cu NPs. The performance of the final material as a drug delivery vehicle was tested by an in-vitro delivery study with chlorhexidine digluconate. The nanoassemblies show a drug loading capacity of 25-40% [mg drug / mg (drug+carrier)]. The drug release was determined to be composed of two steps. First, a burst release of the drug molecules that are loosely held in the voids of the mesoporous carrier followed by the diffusion of the drug molecules that are attached to the carrier surface. The presence of Zr and Cu limits the burst release and beneficially slows down the drug release process.

The effect of pore properties of SBA-15 was explored in a study where the antibiotic doxycycline hyclate was loaded in SBA-15 materials with different pore sizes. It was observed that the pore size is directly proportional to the drug loading capacity [mg drug / mg (drug+carrier)] and the released drug percentage (the released drug amount/total amount of loaded drug). The drug release was fast due to its weak interactions with the SBA-15 materials.

In summary, this work demonstrates the multifunctional character of a smart-tailored nanoassembly which gives valuable insights for two distinct applications in catalysis and drug delivery.

Populärvetenskaplig sammanfattning

Hybridmaterial består av minst två komponenter, vilket ger dem mångfacetterade egenskaper. Detta har gjort att denna typ av material attraktiva sedan länge. Det är dock inte enkelt att tillverka dessa materialsystem. Ett enkelt och effektivt tillvägagångssätt behövs för att tillvara ta de önskade egenskaperna hos varje komponent och få dem att samverka. Denna avhandling bygger huvudsakligen på utvecklingen av ett hybridmaterial. Materialet testas sedan i två olika tillämpningar: katalys och läkemedelstransport.

Ett hybridmaterial med en sammansättning bestämd på nanonivå, tillverkades med mesoporös kiseldioxid, SBA-15, som stomme. SBA-15 valdes framför andra typer av mesoporös kiseldioxid på grund av dess väldefinierade porstruktur och stora, tillgängliga porvolym. Kiseldioxiden dopades med zirkoniumatomer och porerna fylldes delvis med kopparnanopartiklar, vilket resulterade i ett hybridmaterial med egenskaper som kunde varieras. SBA-15 tillverkades via en våtkemisk metod där en micellösning används som mall för kiseldioxidens struktur. Vid dopningen tillsätts en zirkoniumkälla till synteslösningen. Effekterna av olika tillverkningsparametrar, till exempel salter med katalytiska egenskaper (salter med F- eller Cl-), olika kiselkällor (tetraetyl ortosilikat eller natriummetasilikat), på materialens egenskaper studerades. Variationer av dessa parametrar ger material med olika form, porstorlekar (11 – 15 nm) och specifik yta (400 – 700 m^2/g). Kopparnanopartiklar växtes i (Zr-)SBA-15-stommarna med två metoder: infiltration (Inf) eller indunstningsinducerad våtimpregnering (EIWI). Inf baseras på funktionalisering av (Zr-)SBA-15-stommen innan kopparjoner fick reagera med ytan. EIWI bygger på en blandning av (Zr-)SBA-15 och kopparsalt i en lösning där vätskan långsamt får avdunsta. Båda metoderna är designade för framställning av oxiderade kopparnanopartiklar, mindre än 10 nm i diameter, som ska växa i stommens porer. Dock påverkar infiltrationsmetoden den kemiska sammansättningen hos det slutliga materialet då Zr-koncentrationen och porositeten i stommen ändras.

Cu-Zr-SBA-15-sammansättningar, tillverkade med varierande syntesparametrar, användes som katalysatorer för omvandling av CO_2 till bränslen såsom metanol och dimetyleter (DME). Resultaten visar att valet av kiselkälla har en stor inverkan på katalysatorns prestanda, samt att metoden för att introducera koppar ändrar den katalytiska selektiviteten mellan DME och metanol. Katalysatorns aktivitet undersöktes även över tid. Ackumuleringen av varje produkt, både i gasfas och på katalysatorns yta, registrerades över tid. Termodynamisk jämvikt nåddes efter att reaktionen fortgått i fjorton dagar vid 250 °C och 33 bar. Den totala CO_2-omvandlingen var 24 %, vilket, enligt

teoretiska beräkningar, är den termodynamiskt högsta möjliga omvandlingen. Det observerades att DME bildas genom en kombination av två metoxygrupper på katalysatorns yta, samt att bildandet av DME ökar den totala omvandlingen av CO_2 till bränsle, vilken annars är begränsad till 9.5 %.

Cu-Zr-SBA-15-sammansättningen användes även i läkemedelstillämpningar. De kan användas som biomaterial, e.g., fyllnadsmaterial i tandkompositer, och koppar har antibakteriella egenskaper. Dessutom kan kiseldioxid och zirkoniumdioxid vara bioaktiva vilket ses som en fördel. För denna tillämpning tillverkades Cu-Zr-SBA-15 med TEOS som kiselkälla och Inf-metoden för att växa kopparnanopartiklar. Cu-Zr-SBA-15 lämplighet som bärare av läkemedelet klorhexidindiglukonat testades in vitro. I detta fall uppvisar bäraren en laddningskapacitet [massa laddat läkemedel/(massa laddat läkemedel +massa bärare)] på 25 – 40 %. Frisättningen av läkemedel skedde i två steg. Först frisattes en stor mängd läkemedelsmolekyler. Dessa var löst placerade i håligheter i de mesoporösa stommarna. Därefter frisattes läkemedel via diffusion av molekyler som bundit till stommens yta. De två stegen representerar växelverkan mellan läkemedel – läkemedel- och läkemedel – bärare. Närvaron av zirkonium och koppar begränsar den första frisättningen och förlänger den aktiva tiden, vilket är fördelaktigt ur tillämpningsperspektiv.

Effekten av porstorlek hos SBA-15 vid läkemedelsfrisättning undersöktes också i en studie där SBA-15 fylldes med doxycyklinhyklat. Laddningskapaciteten och mängden frisatt läkemedel och andelen av laddat läkemedel som frisätts var båda direkt proportionella mot porstorleken där frisättningen av doxycyklinhyklat dominerades av läkemedel – läkemedelsväxelverkan. Doxycyklinhyklat är en mindre molekyl jämfört med klorhexidindiglukonat och växelverkar svagare med SBA-15 på grund av sin mer anjoniska natur.

Sammanfattningsvis visar arbetet den multifunktionella karaktären hos en skräddarsydd nanosammansättning, vilket ger värdefulla insikter i två användningsområden: katalys och läkemedelstransport.

Resumen

Los sistemas de materiales híbridos poseen propiedades multifuncionales, lo que ha suscitado el interés de la comunidad científica de materiales desde fechas muy tempranas. Sin embargo, no es sencillo producir dichos materiales. Es necesario un enfoque inteligente y eficiente para extraer las propiedades deseadas de cada componente, en las condiciones deseadas. Este estudio evoluciona en torno a esta noción, siendo el desarrollo de un material híbrido el núcleo del trabajo. Adicionalmente, este material híbrido se explora para dos aplicaciones diferentes que son la catálisis y la administración de fármacos.

En este trabajo se desarrolló un nanoensamblaje alrededor de un soporte de sílice mesoporoso. Como soporte se seleccionó SBA-15 debido a su estructura de poro bien definida y volumen de poro accesible. La matriz de sílice fue dopada con átomos de Zr y los poros se infiltraron parcialmente con nanopartículas de Cu dando como resultado un material híbrido con propiedades ajustables. La síntesis de SBA-15 se realizó mediante un método de sol-gel en el que se empleó una solución micelar como plantilla para el sílice. Para lograr la versión dopada, se añadió un precursor de Zr a la solución de síntesis. Se investigaron los efectos de diferentes condiciones de síntesis, como el catalizador (sales de F o de Cl) así como la fuente de Si (ortosilicato de tetraetilo (TEOS) o metasilicato sódico (SMS)) en las características del material final. Se observó que los cambios en estas condiciones de síntesis dieron lugar a partículas con distinta morfología, tamaño de poro (11-15 nm) y área superficial específica (400-700 m^2/g). Las nanopartículas de Cu (NP) se hicieron crecer en el sustrato (Zr-) SBA-15 usando los métodos de infiltración (Inf) o de impregnación húmeda inducida por evaporación (EIWI). El método de infiltración se basa en funcionalizar las superficies de soporte (Zr-) SBA-15 antes de la unión del ion Cu, mientras que EIWI se basa en la evaporación lenta del líquido de la suspensión acuosa (Zr-) SBA-15-Cu. Ambos métodos se han diseñado para producir un crecimiento preferencial de Cu NP en los poros con un diámetro inferior a 10 nm y en forma oxidada. Sin embargo, dependiendo del método de infiltración utilizado, se logran diferentes estados químicos del material final, es decir, el contenido de Zr y las propiedades de red porosa son diferentes.

Los nanoensamblajes de Cu-Zr-SBA-15 producidos bajo diversas condiciones de síntesis se usaron para la conversión catalítica de CO_2 en combustibles valiosos tales como

metanol y dimetil éter (DME). Se investigó el efecto de diferentes estados químicos del catalizador obtenidos modificando los parámetros de síntesis. Se encontró que el precursor de Si (TEOS o SMS) tuvo un impacto considerable en el rendimiento global del catalizador mientras que el método de carga de Cu (Inf o EIWI) cambió la selectividad catalítica entre DME y metanol. Por otra parte, la actividad del catalizador se investigó evaluando la acumulación de cada producto en la fase gaseosa y los grupos moleculares unidos a la superficie del catalizador a lo largo del tiempo. Se llegó al equilibrio termodinámico en el día 14 de la reacción a 250 ° C y 33 bar. La conversión total resultante de CO_2 fue del 24%, que es la conversión termodinámicamente más alta posible, según los cálculos teóricos. También se concluyó a partir de los resultados experimentales que, el DME está formado por una combinación de dos grupos superficiales metoxilados. Asimismo, la formación de DME también aumenta la conversión total de CO_2 en los combustibles, que de lo contrario se limita al 9,5%.

El material híbrido sintetizado Cu-Zr-SBA-15 también se investigó para aplicaciones de administración de fármacos, debido a su potencial como material de relleno en compuestos dentales y las propiedades antibacterianas del Cu. Por otra parte, la bioactividad de SiO_2 y ZrO_2 podría ser ventajosa para esta aplicación. Con este objetivo, se preparó SBA-15 dopado con Zr e infiltrado con Cu utilizando TEOS como el precursor de sílice y el método Inf para cultivar Cu NP. El rendimiento del material final como vehículo de administración de fármacos se probó mediante un estudio de liberación in vitro con digluconato de clorhexidina. Los materiales desarrollados muestran una elevada capacidad de carga de fármaco (25-40%). Los perfiles de liberación del fármaco muestran dos etapas: una primera etapa de liberación rápida de las moléculas del fármaco unidas con interacciones más débiles al sustrato mesoporoso, seguida por la difusión de las moléculas del fármaco que están unidas a la superficie del portador. La presencia de Zr y Cu limita la liberación inicial y reduce la velocidad de liberación del fármaco.

En otro estudio se evaluó el efecto del tamaño de poro de SBA-15 en la liberación del antibiótico hiclato de doxiciclina. Se observó que el tamaño de poro es directamente proporcional a la capacidad de carga de fármaco, el porcentaje y la cantidad de fármaco liberado. En este estudio el perfil de liberación fue rápido, debido a las interacciones débiles del fármaco con el SBA-15 y el menor tamaño de molécula del fármaco en relación al digluconato de clorhexidina del estudio anterior.

En resumen, este trabajo demuestra el carácter multifuncional de una nanomatriz diseñada a medida que proporciona información valiosa para dos aplicaciones en catálisis y liberación de fármacos.

Preface

This thesis is the result of my doctoral studies conducted within the framework of the Joint European Doctoral Program in Material Science and Engineering (DocMASE) between September 2012 and October 2017. Starting from October 2015, 33% of the Ph.D. time was devoted to a part-time job with Nanolith Sverige AB until October 2017 after which this employment became full time.

This thesis shows different production methods for an advanced functional material on a complex matrix to be able to serve selected applications in catalysis and drug delivery areas. These application areas may seem very different, but similar nanostructures can be favorable for both, in various ways. Thus, the focus evolved around the material characteristics and synthesis optimization. The key results are presented in the appended papers.

The part of the work related to material synthesis and catalysis was performed in Nanostructured Materials Group at the Department of Physics, Chemistry and Biology (IFM) at Linköping University, Linköping, Sweden and the part related to drug delivery was performed in Biomaterials, Biomechanics and Tissue Engineering Group at the Department of Materials Science and Metallurgical Engineering of the Universitat Politècnica de Catalunya, Barcelona, Spain.

This work was financially supported by EU (DocMASE), Vinnova (FunMat-II), Swedish Energy Agency, and Knut and Alice Wallenberg Foundation.

Included Papers

Paper 1

Synthesis of a Cu-infiltrated Zr-doped SBA-15 catalyst for CO_2 hydrogenation into methanol and dimethyl ether

A. Atakan, P. Mäkie, F. Söderlind, J. Keraudy, E.M. Björk, and M. Odén

Phys. Chem. Chem. Phys. 19 (2017) 19139

DOI: 10.1039/C7CP03037A

Paper 2

Effects of the chemical state of mesoporous CuO_x-Zr-SiO_2 catalysts on CO_2 hydrogenation

A. Atakan, J. Keraudy, P. Mäkie, C. Hulteberg, E.M. Björk, and M. Odén

Submitted for publication

Paper 3

Time evolution of the CO_2 hydrogenation to fuels over Cu-Zr-SBA-15 catalysts

A. Atakan, E. Erdtman, P. Mäkie, L. Ojamäe, and M. Odén

J. Catal. 362 (2018) 55

DOI: 10.1016/j.jcat.2018.03.023

Paper 4

Cu and Zr modified SBA-15 as drug carriers

A. Atakan, C. Canal, P. Mäkie, M. Odén, and M. Ginebra

Submitted for publication

Paper 5

Tuning the pore size of a mesoporous carrier as means for control of antibiotic release

A. Atakan, C. Canal, P. Mäkie, M. Odén, and M. Ginebra

In manuscript

Related, Not Included Papers

Paper 6

Formation of block-copolymer-templated mesoporous silica

E.M. Björk, P. Mäkie, L. Rogström, A. Atakan, Norbert Schell, and M. Odén

J Colloid Interface Sci 521 (2018) 183

DOI: 10.1016/j.jcis.2018.03.032

Contribution to the Included Papers

Paper 1

I planned the study, performed the material synthesis, conducted the GC-MS measurements, analyzed all the results and wrote the first draft of the paper. I also took part in the material characterization, catalytic reactions, and DRIFTS analysis.

Paper 2

I planned the study, performed the material synthesis, conducted the GC-MS measurements, analyzed all the results and wrote the first draft of the paper. I also took part in the material characterization, catalytic reactions, and DRIFTS analysis.

Paper 3

I planned the study, performed the material synthesis, conducted the GC-MS measurements, analyzed all the results and wrote the first draft of the paper. I also took part in the material characterization, catalytic reactions, and DRIFTS analysis.

Paper 4

I performed the material synthesis, drug delivery tests, analyzed the results and wrote the first draft of the paper. I also took part in the planning of the study and antibacterial tests.

Paper 5

I performed the material synthesis, drug delivery tests, antibacterial tests, analyzed all the results and wrote the first draft of the paper. I also took part in the planning of the study.

Acknowledgements

I would like to thank all the people who were, willingly or not, involved in my Ph.D. studies. In particular,

My supervisor Prof. Magnus Odén for giving me the opportunity to work in this project, and for all the support, guidance, and patience when I get 'dramatic'..
My supervisor Prof. Maria Pau Ginebra for letting me a part of her research group in UPC, the opportunity to work in drug delivery and all your support during this time.
My co-supervisor Dr. Cristina Canal for supporting me in my studies in UPC, and teaching me the 'bio' side of materials science.
My co-supervisor Dr. Fredrik Söderlind for the support and guidance especially in operating the GC-MS.
Peter Mäkie for being a great help and support for many years in Ph.D. and my 'calm down' person to help me step down on earth. I will forever be grateful!
Emma Björk for all the guidance and input, especially for during paper-writing stages and of course for teaching me how to synthesize SBA-15. I appreciate your encouragement to keep pushing in my Ph.D. studies.
Sven Andersson for helping with technical issues numerous times and supporting me in abandoning my 'forever leak-source' reactor.
My dear friends, I got during the last six years, especially Isabella, Fei and the members of the 9 o'clock coffee club: Mathias, Sebastian, Daniel, Eric. Special thanks to Lida and Mercan for your sincere and comforting friendship. Without you, I wouldn't be able to 'keep my cool' during Ph.D.
All my colleagues in the Nanostructured Materials in Linköping as well as in the Biomaterials, Biomechanics and Tissue Engineering Group group in Barcelona.
My mother Şirin Atakan, my father Erol Atakan, and my sister Simay Atakan for being my biggest emotional and technical support despite the kilometers between us.
I am forever grateful to my beloved husband Julien Keraudy for his guidance and patience. (especially the patience ☺). Even at the most stressful times, he managed to put a smile on my face.

Symbols and abbreviations

λ	wavelength
θ	scattering angle
μ	chemical potential
ATR	attenuated total reflectance
BASF	Baden aniline and soda factory
BJH	Barret-Joyner-Halenda pore size distribution determination method
c_{ini}	initial drug concentration
c_s	drug solubility
CHX	chlorhexidine digluconate
CRI	Carbon Recycling International
D	diffusion coefficient
d_{hkl}	lattice spacing
DME	dimethyl ether
DMFC	direct methanol fuel cells
Doxy	doxycycline hyclate
DRIFTS	in situ diffuse reflectance infrared Fourier transform spectroscopy
EDS/EDX	energy dispersive x-ray spectroscopy
FID	flame ionization detector
FTIR	Fourier transform infrared spectroscopy
H	enthalpy
G	Gibbs free energy
GC	gas chromatography
ICI	Imperial Chemical Industries
IUPAC	International Union of Pure and Applied Chemistry
k	drug release rate constant
k_0	zero order drug release constant
k_H	Higuchi dissolution constant
KJS	Kruk-Jaroniec-Sayari pore size correction method
LPG	liquefied petroleum gas
MeOH	methanol
M_0	initial drug amount
M_t	amount of drug released in time t
M_∞	amount of drug released in time infinity
MEC	minimum effective concentration
MS	mass spectrometry
MTC	minimum toxic concentration
P123	PPO-PEO-PPO triblock copolymer
P_1 and P_2	the percentage of the drug released during phase 1 and 2
PEO	polyethylene oxide
PPO	polypropylene oxide
RWGS	reverse water gas shift reaction

SEM	scanning electron microscopy
TEOS	tetraethyl orthosilicate
TG	thermogravimetry
TMOS	tetramethyl orthosilicate
UV/vis	ultraviolet-visible spectroscopy
WGS	water gas shift reaction
XPS	x-ray photoelectron spectroscopy
XRD	x-ray diffraction
t	time
t_l	lag time
T	temperature
TCD	thermal conductivity detector
TEM	transmission electron microscopy

Table of Contents

1

INTRODUCTION

Modifying materials for achieving certain functionalities goes back to the prehistoric ages where men first used stone as a tool for different purposes such as modifying surfaces, farming or hunting. These ages of humanity are named after their primary source of tool materials: 1) stone, 2) bronze and 3) iron age. The first use of ceramics was during the stone age with flint, whereas the glass was not produced until late iron age. Until this day, tremendous progress was made in synthesis, processing, modifying, and analysis of many material types and the field has evolved around metals, ceramics, polymers and different composites.

Materials science serves many application areas such as energy, medicine, electronics, and machinery and it is typically multidisciplinary where a material can be investigated for many different purposes. It is quite remarkable that a material with certain properties can have various functions and thus have different identities such as a catalyst, a drug carrier, a nano-mold or a coating. Therefore, a cross-disciplinary outlook on different application fields of materials is a source for further improvement of material properties.

1.1 Motivation

The motivation of this thesis lies in the multidisciplinary character of materials science. The focus is to modify a mesoporous silica, SBA-15, to gain advantageous properties for two different applications areas: catalysis and drug delivery. SBA-15 is a type of mesoporous silica characterized by a large pore volume, considerably large pore size, and

robustness in terms of hydrothermal and chemical stability allowing it to maintain its hexagonal pore packing structure under rather harsh conditions. Thus, it can serve these two areas very well and be a perfect complementary material for many active substances.

In the field of **catalysis**, SBA-15 can be used as a support and a promoter for the catalytically active phase. It has been shown to support active metal phases, such as Cu, especially during heterogeneous catalysis of a gas phase reaction. In this work, such a catalyst system was prepared by growing Cu nanoparticles on a Zr-doped SBA-15 support. This material was later used for CO_2 hydrogenation reaction to convert one of the most significant anthropogenic greenhouse gas CO_2 to valuable fuels such as methanol and DME. Although CO_2 hydrogenation into methanol has been studied earlier, the search for a suitable catalyst is an on-going process due to the thermodynamic limits. On the other hand, CO_2 hydrogenation to DME is a considerably new field, and the findings so far indicate that it requires a complex catalyst that can catalyze both CO_2 hydrogenation to methanol and methanol dehydration to DME.

Another field where SBA-15 has been recognized and used is **drug delivery**. Due to its favorable porous structure, it can accommodate many different sizes of drug molecules and thus can be used as a drug carrier. Its large pore volume can host a drug amount higher than the minimum effective concentration of a chosen drug. Cu is a common antibacterial agent and in this thesis, it is investigated as nanoparticles embedded in the mesopores of an SBA-15 framework with the aim of prolonged ion release. Moreover, Cu nanoparticles can form obstacles in the pores and can cause partial blockage, which results in prolonged ion release. Zirconia, as a bioactive material, was also used as a complementary unit to the SBA-15 framework in order to improve the number of active sites on the surface contributing to the drug loading.

The aim of this project was to produce a Cu-Zr-SBA-15 material by doping Zr into the SiO_2 framework and loading Cu nanoparticles into the mesoporous structure. This material was then tested as a high-performance catalyst for CO_2 hydrogenation as well as a favorable drug carrier for in-vitro delivery of Chlorhexidine digluconate (an antiseptic agent) and Doxycycline hyclate (an antibiotic) for dental applications such as implantation or dental composites.

1.2 Outline

In this thesis, a general overview of SBA-15 synthesis and modification is presented in Chapter 2, where its structural properties, synthesis mechanisms, and modification methods are discussed. Environmental significance of CO_2 utilization is described in Chapter 3 where the mechanisms behind the CO_2 hydrogenation to methanol and DME and the applicability of these two fuels in the industry are explained. Chapter 4 is dedicated to the general aspects of drug delivery, drug delivery systems, drug release profiles and models and lastly nanostructured drug carriers. Chapter 5 includes short information regarding the analysis methods used during this work. Chapter 6 summarizes the results and discussions of the appended papers and in Chapter 7 conclusions and future work is discussed. At last, papers are appended.

2

MESOPOROUS SILICA

2.1 Porous materials

Porous materials are solid materials with voids within their structural configuration. The voids which are deeper than they are wide are called pores, and they have a great range of morphologies that are typically channels but also cavities and interstices. The pores can have an open or closed nature. The closed pores can be used for altering the overall material properties (e.g., density), mechanical properties (e.g. hardness and elasticity), and conductivity. On the other hand, open porosity provides extra surface and inner volume to the material improving its carrier properties for guest molecules[1].

Pores, according to IUPAC's definition, can be classified into three groups: macropores with the pore width larger than 50 nm, mesopores with the pore width between 2 and 50 nm and micropores with the pore width smaller than 2 nm[2]. Among the unlimited possibilities of the porous world, mesoporous materials, amorphous or crystalline, have gained a significant amount of attraction due to their large internal surface and pore volume allowing them to host molecules of various morphologies and sizes[3].

Mesoporous silica was first reported by researchers at Mobil Corporation in 1992[4], and they named this 'first of its kind' mesoporous silica MCM-X where MCM represents 'Mobil Crystalline Material' and X represents different structural properties within the same material group. The ordered porosity of this silica material was obtained by a liquid-

crystal templating approach that enables the formation of silicate walls between the surfactant micelles with an ordered hexagonal pattern. As a result, cylindrical pores between the walls with a narrow pore size distribution are obtained[3,4]. Moreover, with its large surface and pore volume, mesoporous silica is very suitable for hosting various molecules and particles, and thus it is used in many applications such as catalysis, drug delivery, sensing, and separation[5,6]. The uniform and organized pores enable controlled loading and release of guest molecules depending on the nature of the attachment between the guest and the host[5–9]. They also show high thermal, chemical[10] and mechanical stability and are therefore favorable for applications that require extreme conditions[11].

2.2 SBA-15

SBA-15 was the next breakthrough in the field of mesoporous silica synthesis after MCM. This type of mesoporous silica was first reported in 1998 by Zhao *et al.* and named as SBA-X where SBA stands for 'Santa Barbara Amorphous' and X stands for different pore structures and surfactants[12]. SBA-15 has similar hexagonal pore packing structure as MCM-41, but a larger tunable pore width and higher hydrothermal and chemical stability due to its thicker walls. These features make SBA-15 more popular compared to its MCM ancestors[6,12,13]. Also among all the other SBA materials, SBA-15 is particularly attractive due to its highly stable structure offering flexibility in the synthesis conditions and possibilities to affect structural parameters such as particle morphology and pore size without destroying the SBA-15 structure[14].

The morphologies of SBA-15 reported so far include rods[15], fibers[16], sheets[17], spheres[18] and hollow spheres[10] (Figure 1). It has cylindrical pores with a cross-sectional diameter between 5-30 nm, although pore size above 11 nm is rare[12,19]. Its mesopores are interconnected with micropores, which can constitute a significant portion of the total pore volume. For example, a microporosity of 50% has been reported by Hartmann *et.al.* and 15-30% by Björk *et.al.*[14,20,21]. SBA-15 has been successfully used in various applications because of its combination of these interesting characteristics, e.g., a template, catalyst support, drug carrier, selective adsorbent etc[11,14].

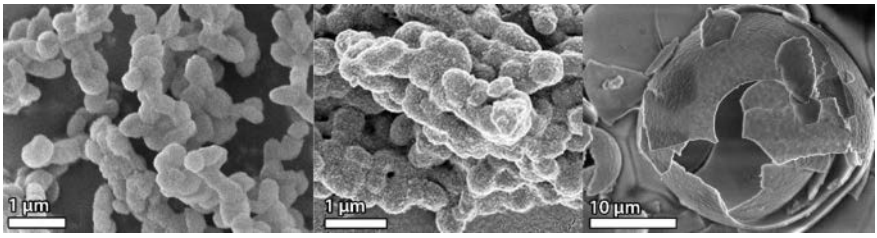

Figure 1. Different particle morphologies of SBA-15: small particles (left), long fibers (middle), sheets (right)[16].

2.2.1 SBA-15 synthesis

SBA-15 is typically synthesized via a sol-gel technique where a solution, *sol*, of templating micelles is prepared at a suitable pH and then mixed with a silica precursor. As a result, a silica network forms through a series of hydrolysis and condensation reactions constituting a *gel* that typically separates from the solution. During hydrolysis, silicon hydrolizes and become silicic acid and then condenses to form Si-O-Si framework as seen in Eq. 2.1 and 2.2[22].

During

Hydrolysis $\equiv\text{Si-OR} + \text{H}_2\text{O} \rightarrow \text{Si(OH)}_4 + \text{ROH}$ (2.1)

Condensation $\equiv\text{Si-OH} + \text{HO-Si}\equiv \rightarrow \text{Si-O-Si} + \text{H}_2\text{O}$ (2.2)

Upon condensation, a maturation period is typically needed and the final material is obtained after removal of the micelles.

For the modification of the morphological (pore or particle) characteristics, it is also possible to add salt and swelling agent into the synthesis solution.

The micellar solution is an aqueous solution of templating micelles which are based on surfactants. Surfactants are amphiphilic low molecular weight materials or block copolymers possessing a hydrophilic head group (ionic or non-ionic) and a hydrophobic non-polar chain. Due to this structure, they can self-assemble in an aqueous solution with a concentration that is above the critical micelle concentration. This self-assembly forms a liquid crystal in the end by creating water-oil interfaces within some degree of ordering[23,24].

For the synthesis of SBA-15, the surfactants mostly reported in the literature are Pluronics, CTAB, and PEO surfactants. Pluronics are non-ionic block polymers made up of a polypropylene oxide block $(PO)_x$ placed in the middle of two polyethylene oxide blocks $(EO)_x$. Pluronics, when combined with an acidic solution, form sphere-like micelles hiding the hydrophobic part in the center of the sphere and exposing the hydrophilic ends to the solution forming a corona[25]. Therefore the length of the chains can affect the shape and size of the micelles.

Among the pluronics, a symmetric block copolymer P123 (PEO-PPO-PEO) has been shown to yield a consistent and robust structure when synthesizing SBA-15 with different particle morphologies, including platelets and short rods with easily accessible pores[21]. In-situ SBA-15 synthesis studies have shown that P123 form spherical micelles which then open up to cylindrical structures as silica condensation proceeds and form cylindrical pores[15,22,26].

The **silica precursor** is typically chosen from alkoxides, which is mostly tetramethyl orthosilicate (TMOS) and tetraethyl orthosilicate (TEOS). Some studies also have reported sodium metasilicate to form the hexagonal SBA-15 structure[20].

Additives can be used in the synthesis of SBA-15 and are typically salts or oils.

Salts can act as catalysts for SBA-15 synthesis affecting the reaction rate by changing the cloud point, and it can also decrease the critical micelle temperature. This occurs because a salt can change the solubility of the surfactants by its salting out or salting in effect. For example, when an anion, such as F^-, is released to the synthesis medium by compound dissolution, it demonstrates salting out effect that leads to partial dehydration of EO chains and causes hydrophobic core enlargening inside the micelles[16,25]. Cations were shown to demonstrate a similar but weaker effect[27]. The salting out effect during SBA-15 synthesis is typically achieved with F^-, Cl^- or I^- by using NH_4F or NaI salts and it leads to increased pore size[25,28].

Swelling agents are organic materials such as alkanes, amines or substituted benzene compounds[29,30]. When added to the synthesis solution, they can penetrate into the micellar structures and settle in the hydrophobic centre causing micelle swelling. During SBA-15 synthesis, since the micelle size determines the pore size, an addition of a swelling agent can directly affect the pore size[31]. Alkanes can increase the pore size to around 26 nm while maintaining the hexagonal pore order[32]. By changing the pore order, e.g., changing to

MCF (mesostructured cellular foam), much wider pores can be obtained[31]. It was also shown that heptane could increase the pore size above 12 nm when used in a low temperature synthesis of SBA-15 together with NH_4F salt[21].

Hydrothermal treatment or aging, constitutes the maturation period of SBA-15. Hydrothermal treatment is a post-synthesis re-structuring procedure typically required in case of using non-ionic oligomeric surfactants, such as P123. Aging at high temperature, which is typically around 100°C, causes dissolution-reprecipitation of Si atoms to the formed walls. During reprecipitation of the silicate species, they get rearranged to a more thermodynamically favorable position minimizing the surface energy, i.e., become smoother[33].

Surfactant removal can be performed by a chemical assisted extraction method that involves stirring the freshly prepared SBA-15 with an oxidizing agent. However, a more straightforward method is calcination where the polymer is decomposed and combusted with air at high temperature, typically higher than 500°C [34].

2.2.2 SBA-15 modification routes

SBA-15 has been modified with numerous types of different atoms, molecules and molecular groups as described in earlier reports. Many earlier studies focusing on modification of SBA-15 are based on physical mixing[35], however, improved procedures can improve the interface between different components of hybrid materials that promote their activity in the target application[36–38]. The most common methods are in-situ incorporation[39–43], co-precipitation / deposition-precipitation[44–48], post-grafting[49,50], impregnation[51–55], incipient wetness impregnation[31,42,56–58], and infiltration[59,60]. A crucial issue for almost all of these methods is to obtain uniform distribution of the modifier throughout the catalyst[61]. The selection of the proper method depends on the desired characteristics of the catalyst. For example, to prepare a Zr doped SBA-15, an in-situ incorporation technique can be used.

In-situ incorporation[62–66] can be performed by adding the relevant precursor into the synthesis batch of a chosen material to induce doping. It is typically used to add functional groups or atoms into the framework of a matrix such as SBA-15. It was also shown for polymer growth in SBA-15 porous network[67]. For example, adding a precursor into the

synthesis solution of SBA-15 right before the gel formation leads to a mesoporous heteroatomic network with Si, O, and the additional atom obtained from the precursor.

The impregnation[67–69] method includes stirring of the main supporting matrix, e.g., SBA-15, MCM-41, H-ZSM-15 with a precursor solution (e.g., a sulfate or nitrate salt), filtration, washing, and drying.

The Incipient Wetness Impregnation[66,70,71] is a modified version of impregnation; however, due to the high level of interest by the research community and many reports focusing on this method, it deserves to be mentioned separately. It is, indeed, performed in a very similar way to impregnation technique except for the part where the same volume of precursor solution of the metal salt as the pore volume of the relevant porous material is used. The aim is to direct the metal ions into the pores such that out-of-particle aggregation is minimized.

Post-grafting[49,65,66,71,72] takes place when the SBA-15 is suspended in a precursor solution typically with a solvent like ethanol or toluene, stirred for a long time under high temperature, filtered, washed with the same solvent and dried at high temperature. The most significant differences between grafting and impregnation appears in the surface properties. During grafting the attachment of the guest to host occurs on a molecular level where chemical bonds are formed, while impregnation only causes deposition of the guest on the surface of the porous host. Grafting can be referred as a post-synthesis surface doping method.

Infiltration[59,73] is a technique that focuses on the minimization of the outer-mesoporous particle attachment of the metal nanoparticles. For that purpose, the outer surface of the mesoporous particles is first passivated, and then the inner surface of the mesopores is activated with functional groups. The functionalization enables the metal ions to attach to the inner functional groups so the nanoparticles can grow only on the inside the pores. However, it is a challenging process, and in some cases, metal nanoparticles are still obtained on the outer surface of the mesoporous particles.

3

CATALYSIS

3.1 Industrial revolution and greenhouse gases

The industrial revolution started in the 1760s in Britain with the discovery of new fuel sources and the development of new industrial processes replacing the hand-based production methods. This revolution was triggered by the invention of the steam engine by Thomas Newcomen in early 1700s, although there are records of using steam power for processing purposes in different parts of the world at earlier dates. The steam engine can provide steam power not only for industry but also for the transportation, and was typically achieved by burning fossil fuels such as coal, oil, and gas. A vast amount of energy could be released through the combustion of these fuels which were at that time abundant in nature. Consequently, the society became dependent on them. However, the fossil fuel combustion emits tons of CO_2 and H_2O to the atmosphere causing global warming and environmental changes[74–76]. Since that era, the concentration of CO_2 in the atmosphere has been increasing rapidly, from 280 ppm before 1750 to 400 ppm in 2016[77]. The high concentration of CO_2 can trap the heat and energy absorbed by earth from solar radiation and prevent the infrared radiation from earth back into space. This natural phenomenon is defined as the greenhouse effect, and it is well-known to be responsible for a rise in the earth's surface temperature, also referred to as global warming which leads to climate

change, constituting a real threat to human and nature[78–80]. Global warming is also known to cause increased acidity and thus decreased the efficiency of the carbon sinks classified as land, forests, and oceans, which ultimately results in increasing CO_2 accumulation and thus the global warming[78,81]. The probability of a catastrophe due to the greenhouse effect and global warming has triggered the society to take precautions and solid action plans for decreasing the concentrations of the greenhouse gases in the atmosphere. The most common greenhouse gases found in the nature are CO_2, water vapor, CH_4 and N_2O, chlorofluorocarbons (CFC) and hydrofluorocarbons (HFC)[82]. Among them, CO_2 became the main anthropogenic greenhouse gas due to human activity[83–87]. The critically rising trend of CO_2 concentration in the atmosphere can be reversed by adopting two types of strategies: (1) preventing the CO_2 emissions and (2) utilizing the CO_2 that is constantly being emitted by running processes, i.e., recycling[84,88]. The first strategy includes exchanging firmly established processes with new ones. This is a challenging task from a scientific (technical) point of view since it requires demolishment before rebuilding and therefore has high risks regarding industrial feasibility and financial balance of firms. The second strategy considered so far, has a better chance in surviving the economical limits of industry, since it includes only addition of a new process at the end of an existing production line in order to capture and convert CO_2 into different sustainable products.

3.2 CO_2 utilization

Elimination of CO_2 from the environment by recycling emissions has three stages of action: (1) capture, (2) storage and (3) consumption/expenditure[83,85,86,89,90].

CO_2 capture involves mainly separation[68] and collection of emitted CO_2 from an industrial site or a natural source such as geothermic wells and delivering to a facility where it can be stored, typically in geological structures underground which is a rather established issue in these days[76,89,91]. It was shown that capture of CO_2 on site has a higher efficiency than from the atmosphere because higher concentration facilitates capturing materials and techniques[62]. The capture is typically done with the use of adsorbents such as amine solutions or hydroxides[76,87]. Capture and storage of CO_2, as important as they are, do not constitute the ultimate solution of CO_2 elimination but provide more of 'swipe under the rug' type of solution. Therefore, it is a crucial task to develop and improve processes where CO_2 can be used up.

Consumption/expenditure of CO_2 as an eco-friendly, value-added chemical feedstock has attracted a great deal of attention among the scientific community to develop several innovative processes where CO_2 is recycled and employed as a building block for producing hydrocarbons and alcohols[68,82,92,93]. However, CO_2 is a poor reactant, and its activation is a challenging task due to its high thermodynamic stability originating from the fact that CO_2 is the highest oxidized state of carbon[68,87,94]. At this oxidation state, carbon does not have any tendency of changing its chemical environment. In order to transform CO_2, one needs to overcome its Gibbs energy of formation ($\Delta G^{o}_{298.15K}$ =-394.4 kJ mol^{-1}), which means that a considerable amount of energy is required to be applied [95]. Therefore, it is important to develop techniques to catalyze this type of reaction with a proper mechanism and a suitable catalyst.

Several methods have been developed to break down CO_2 through catalytic reactions and manufacture different organic compounds such as urea, salicylic acid, and various carbonates. CO_2 is also used in certain applications in the food industry, dry cleaning and decaffeination of tea and coffee and most of these processes are commercially implemented[82,87,91]. Another well-established process to use CO_2 as a reactant is RWGS (reverse water-gas shift) reaction where H_2 is used to convert CO_2 to CO (Eq. 3.1) which can then be used to produce several hydrocarbons like gasoline by employing the Fisher-Tropsch process[82].

A strong application candidate for CO_2 expenditure is through a hydrogenation reaction which follows through an artificial photosynthesis mechanism[76,96]. Syngas [$CO+CO_2+H_2$] is an established reactant mixture for creating hydrogenation mechanism to produce valuable fuel candidates such as methanol and dimethyl ether (DME)[74,75]. A similar mechanism can be used to convert pure CO_2 in the presence of H_2 and high pressure. During pure CO_2 hydrogenation the RWGS (reverse water-gas shift reaction)[68] also occurs due to its endothermic character causing formation of CO[83].

$$CO_2 + H_2 \leftrightarrow CO + H_2O \quad \textbf{(3.1)} \qquad \Delta H_{(298\,K)} = 41.2 \text{ kJ mol}^{-1}$$

The total reaction rate of CO_2 hydrogenation strictly depends on the water gas shift reaction due to forming CO and H_2O in the catalytic medium. The CO that is produced with RWGS can be a secondary C source for the targeted product (e.g., methanol), and can affect the reaction balance. H_2O is another product of the targeted methanol formation process so additional H_2O introduced by RWGS into the reaction environment

can inhibit the reaction which makes the product removal very important. Moreover, the formed CO and H_2O can be converted back to CO_2 and H_2 by a water-gas shift reaction (WGS), as the concentrations of the reactants decrease due to the main catalytic reaction, the WGS can be a reactant supplying mechanism. It was reported earlier by Skrzypek et al. that adding CO to the feed gas can increase the CO_2 conversion due to consumed H_2O and recovered CO_2 by RWGS[97].

The hydrogenation of CO_2 is a catalytic reaction and can be done in a single-phase (homogeneous catalysis) or multi-phase (heterogeneous catalysis) manner[98–100]. It was shown in earlier studies that homogeneous catalysts had higher CO_2 conversion performance compared to heterogeneous catalysts. However, the recovery and regeneration of homogeneous catalysts is much more difficult causing extra costs in larger scale, and thus not ideal[68].

CO_2 hydrogenation via heterogeneous catalysis typically follows three reaction steps: (1) reactant adsorption on the catalyst surface, (2) diffusion of the adsorbed molecules on the surface until attaching on an active site, (3) transformation until a stable phase is reached and (4) desorption of the final material. It is typically conducted in a fluidized bed, or fixed bed reactor, whereas batch reactor or stirred tank reactors are less common for this type of a reaction[99,101]. These reactions are typically conducted with metal-based catalysts such as Co, Fe, and Cu which is chosen according to the target product[91].

The existence of many possible reaction pathways of a $[CO_2+H_2]$ mixture makes it crucial to control the reaction environment carefully, especially by providing a suitable catalyst that would realize the primary aim. This way, it is possible to reach a specific target product such as methanol and DME[76].

3.2.1 Methanol

Methanol is an important and established chemical feedstock and solvent in different industries such as chemical, petrochemical, pharmaceutical, and polymer[80,102,103]. It is a critical alternative energy source which is not based on petroleum. It is a safe alternative fuel due to its soot or smoke-free burning characteristic. One risk of methanol to human life and health is its toxicity in case of oral consumption in large amounts[74–76,83]. Therefore

it can replace the traditional fuels or can be used as an additive to traditional diesel or gasoline fuels due to its high octane number (~105) [68,104].

Methanol, besides being a fuel, can also be used as a feedstock or intermediate for producing many different compounds. Another aspect of methanol has energy implications since it can be used to store hydrogen. Storage of hydrogen is otherwise a significant challenge due to a high risk of catastrophic combustion[75,105], hence methanol storage constitutes a more safe way to store hydrogen[83,104,106]. As a result, many research groups have started to investigate direct methanol fuel cells (DMFC)[76,102,107].

The first industrial-scale methanol synthesis used syngas as the feedstock for a hydrogenation process (BASF 1923)[106,108] and methanol production from syngas is still used in the industry by ICI[83]. For many years, scientists focused on producing methanol from syngas due to a constant supply of syngas via the burning of fossil fuels. However, it is not an easy challenge since methanol is the least probable (thermodynamically) product of CO and CO_2 hydrogenation. Typically higher alcohols and hydrocarbons demonstrate larger negative ΔG^0 values, and therefore they have a higher likelihood to be the final product of this type of reaction[109].

CO was known as the primary source of methanol, but it was also essential to have a small amount of CO_2 as a complementary to CO, making syngas a perfect feed mixture for methanol production[68,96,99,102,106,110]. However, later on, an isotope labeling study showed that CO_2 is the main carbon source of the synthesized methanol molecule and CO conversion to methanol proceeds through the CO_2 intermediate, as confirmed by also other studies[84,90,96,97,103,106,111]. Due to this reason, also considering with the environmental concerns mentioned in an earlier section, hydrogenation of pure CO_2 has become the focus of methanol production studies. During the CO_2 hydrogenation into methanol (Eq 3.2), RWGS also runs as a parallel reaction. The forming CO then can either converted back to CO_2 by water gas shift (WGS) reaction as in Eq 3.1 or can proceed with another route to form methanol[96]. The reaction mechanisms are shown in Eq 3.2 and 3.3.

$$CO_2 + 3H_2 \leftrightarrow CH_3OH + H_2O \quad \textbf{(3.2)} \qquad \Delta H_{(298\ K)} = -49.5\ kJ\ mol^{-1}$$

$$CO_{(produced\ by\ RWGS)} + 2H_2 \leftrightarrow CH_3OH \quad \textbf{(3.3)} \qquad \Delta H_{(298\ K)} = -90.8\ kJ\ mol^{-1}$$

These reactions may involve different intermediate steps and compounds depending on the reaction route driven by the catalyst surface. By using a catalyst consisting of **Cu** as the

main active phase, two main reaction routes for methanol synthesis from CO_2 hydrogenation are presented in the literature[106] which are *formate/formyl route* and *hydrocarboxyl route*[112].

Formate/formyl route[97,99,112–116] advances through the formation of HCOO (formate) by CO_2 and a hydrogen atom which then continues by further addition of H atoms at each step. Finally, it forms methoxy (CH_3O^-) and then methanol. Formyl route proceeds in a very similar manner to formate route, but with an additional first step of CO_2 conversion to CO by RWGS. In the next step, one molecule of CO merges with an H atom forming HCO (formyl) compound which is then further converted to methoxy and methanol. The basic schemes of these reaction routes can be found in Figure 3.1.

Hydrocarboxyl route[112,114,117] advances through the formation of COOH (carboxyl) by CO_2 and a hydrogen atom which then continues with the further addition of hydrogen atoms at each step. The basic schemes of these reaction routes are as below.

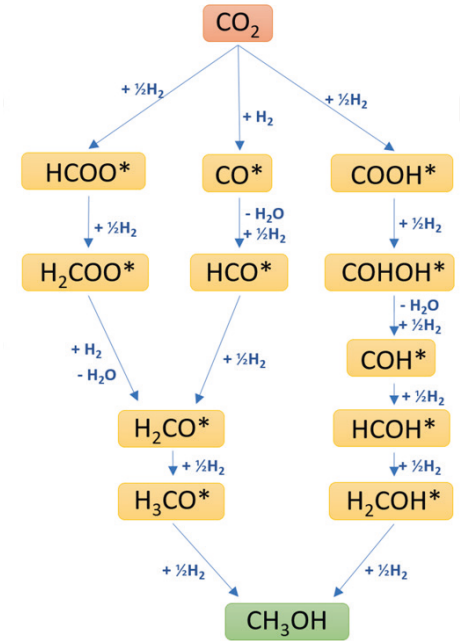

Figure 3.1– Formate/formyl and hydrocarboxyl routes of methanol formation from CO_2 hydrogenation

Among these two, formate route is the one that is mostly adopted in many studies since methoxy and formate were proven to be existent on the catalyst surface by infrared studies[68,111,118]. Moreover, it was theoretically shown that the energy barrier of the COOH formation is much higher than HCOO, making it less likely[112].

The methanol formation as a result of one CO_2 molecule merging with three H_2 molecules has a negative enthalpy indicating that it is an exothermic reaction[68]. Therefore, decreasing the reaction temperature, in principle, should favor the reaction to the products' side (methanol and water) but it is hardly the case due to the necessity of catalyst activation by a sufficiently high temperature[68]. The pressure, on the other hand, can be increased if one aims to increase the CO_2 conversion according to the Le Chatelier principle since every 4 moles of reactants $[CO_2+H_2]$ gives 2 moles of products $[CH_3OH+H_2O]$[105,114,119,120].

So far, the scientific studies which employed syngas as the reactant, obtain methanol at temperatures between 200-450 °C and 30-100 bar with a Cu-based catalyst[84,97,99,110]. The industrial-scale methanol production from syngas is performed by ICI (Imperial Chemical Industries, Ltd.)[121] at temperatures between 220-300 °C and pressure between 50-100 bars using a $Cu/ZnO/Al_2O_3$ catalyst[83,105,111,116]. An industrial-scale methanol production from captured CO_2 is currently conducted by at least two companies under similar conditions (temperature and pressure). The tow companies are CRI (Carbon Recycling International) in the George Olah facility on Iceland and Mitsui Chemicals Inc. in Osaka, Japan[89,122,123]. In this temperature range, thermodynamics is a limiting factor for this type of reaction due to its highly exothermic character. Without any recycling one-time pass CO_2 conversion to methanol by hydrogenation reaction is thermodynamically limited to a maximum of 25%[115] and similarly at 200 °C and 50 bars theoretical CO conversion to methanol is around 20%[116]. On the other hand, under milder conditions such as 250°C and 30 bar, the reported CO_2 conversion to methanol with a Cu based catalyst is typically between 5-15% [84,90,124–128]. The thermodynamic limitations can be overcome by making alterations on the process characteristics, such as removal of a product or recycling the unreacted feed gas. However, in order to accelerate the reaction, the most crucial element is the catalyst. The catalysts studied and used so far for methanol synthesis are typically Cu based material systems where Cu constitutes the active phase with a support and/or a promoter.

3.2.2 Dimethyl ether (DME)

Dimethyl ether (DME) is a significant feedstock for hydrocarbon manufacturing industry and an environmentally benign alternative fuel as a replacement or an additive to liquefied petroleum gas (LPG) which can be used in household utilities or internal combustion engines in the automative industry[76,82,85,129,130]. Although it is volatile, DME is not toxic, not carcinogenic or mutagenic and therefore is already in use as a propellant and coolant[74,101,104,131]. It has good combustion performance compared to traditional fossil fuels due to its high cetane index (around 55-60)[61,68,132]. Moreover, it burns by emitting a quite low amount of NO_x compound and without any soot or SO_2 and producing almost no smoke[68,101,130]. The properties of DME are similar to those of LPG, and thus the delivery and storage means that are or can be employed for LPG are also suitable for DME transportation[35,74,133]. As a result of this ready infrastructure, DME is a quite attractive alternative fuel.

The main synthesis route of DME is catalytic dehydration of methanol as shown in Eq 3.4 [85,134].

$$2CH_3OH \leftrightarrow CH_3OCH_3 + H_2O \quad \textbf{(3.4)} \qquad \Delta H_{(298\,K)} = -23.5\ kJ\ mol^{-1}$$

This reaction is typically catalyzed by a solid acid catalyst[135]. However, the surface acidity of a methanol dehydration catalyst is not a direct measure of the conversion to DME. It was determined that the acid site concentration could directly correlate to the value of methanol conversion to DME whereas this is not the case for the strength of these acid sites[132]. A high amount of moderate strength/weak acid sites can selectively produce DME whereas high strength of the acidic sites can further convert DME to other hydrocarbons[35,36,131,133]. Sites with strong acidity can accelerate water poisoning of the catalyst surface and also attract coke[35]. A considerable amount of sites with moderate acidity was reported to have a better catalytic performance compared to highly acidic sites[68]. It was also reported earlier that basic sites also play a role in methanol dehydration to DME along with the acidic sites[133].

DME can also be synthesized via a direct hydrogenation route from CO_2 or syngas[135,136]. This direct route, in reality, consists of two subsequent mechanisms. The first one is CO_2 hydrogenation to methanol, or its surface adsorbed form called methoxy (Eq 3.2 and 3.3) and the second one is the dehydration of methanol to DME (eq 3.4). Methanol dehydration is not only a convenient method to produce DME, but a way to overcome the

thermodynamic limits of methanol production from CO_2 hydrogenation by consuming methanol which eventually increases the amount of CO_2 converted to methanol[96,133,136]. However, direct DME production from CO_2 hydrogenation is not straightforward. A reason for this is the fact that the second step of this direct route, i.e., DME synthesis by methanol dehydration, requires higher reaction temperature compared to the CO_2 hydrogenation to methanol step. Another reason is that methanol synthesis from CO/CO_2 hydrogenation proceeds on a metallic (typically Cu based) catalyst whereas methanol dehydration to DME requires an acidic catalyst. The catalytically active sites for CO_2 hydrogenation to methanol are on the metal-metal oxide interfaces and the ones for methanol dehydration to DME are surface acid sites[36,61,68,82]. It was also shown in earlier works that the traditional methanol catalyst $Cu/ZnO/Al_2O_3$ is not sufficient for methanol dehydration to DME and it requires a more acidic component such as a zeolite[61]. As a result, a smart catalyst with dual functionality needs to be designed to carry out such a multi-site reaction[124,131,135,137].

It is suggested in some reports that for two methanol to dehydrate to one DME molecule, one methanol molecule needs to get adsorbed on the catalyst surface and become methoxy (CH_3O^-) on an acidic site. The second methanol molecule, on the other hand, needs to get protonated to form $CH_3OH_2^+$ on a basic site and then these two molecules merge to form DME[36,136,138]. However, it is still a topic of debate.

DME synthesis from methanol dehydration is typically performed under 250-400 °C temperature and pressures up to 10 bar[101,130,132]. Depending on the reaction conditions, the methanol conversion to DME can exceed 90%[35,70]. However, in a combined catalytic system which catalyzes both CO_2 hydrogenation to methoxy/methanol and methanol dehydration to DME reactions, the CO_2 conversion to DME strictly depends on the CO_2 conversion to methanol which is the limiting factor.

3.2.3 Catalysts for CO_2 hydrogenation

According to IUPAC, a catalyst is 'a substance that increases the rate of a reaction without modifying the overall standard Gibbs energy change in the reaction'[98]. A catalyst can be used in a reaction, and yet not consumed. Although it can accelerate the reaction in a particular direction, it cannot alter the thermodynamically most stable outcome. The main activity of a catalyst originates from its surface active sites and their affinity to the reactants

which leads to reactant adsorption on the catalyst surface irreversibly such that the desorption time is much longer than the reaction time[106] and this way it promotes their transformation into products[99]. The conversion of the reactants to products does not typically occur in one step but rather through a series of reactions via several unstable intermediates at the catalyst-reactant interphase. In the final step, the products are formed[99]. Besides being catalytically active, a catalyst also needs to be stable, easy-to-produce and cheap to maintain[87].

There are many catalytically active elements that have been studied for heterogeneous catalysis of CO_2 hydrogenation process, and the selection of one or two of these elements depend mostly on the desired product. Ru[100], Rh[139], Pd[59,88,140], Ir[59] and Pt[140] based catalysts have been investigated widely due to their high efficiency in dissociating H_2 and the fact that they are more coke resistant[59,68,80]. However, Cu, Ni and Co-based catalysts maintained their popularity due to their low cost-to-yield ratio[68]. As for the products of the CO_2 hydrogenation process, Cu based catalysts[46,53,59,84,86] can yield CO, various hydrocarbons such as gasoline, alcohols and fuels like methanol and dimethyl ether via methanol route[68] whereas Ni or Co-based catalysts mostly yield methane[68,141]. Dimethyl ether production mainly depends on the acidity of the final catalyst. Thus, the way of Cu couples with the other species in the material systems that constitute the catalyst such as supports and promoters is crucial.

The fabrication of combinations of different atoms or molecules that will act as the primary units of a catalyst assembly has been dominated by co-precipitation[37,46,61,120] technique, also referred to as deposition-precipitation. For example, in the case of producing a Cu catalyst together with a promoter such as ZnO, one has been typically chosen to prepare the catalysts by co-precipitation such that both phases are in contact as nanoparticles[61]. This method is typically used for an assembly with no inter-particular pores but instead intra-particular voids. It is done by stirring a batch of promoter in a solution of the relevant precursor using a predetermined amount corresponding to a monolayer of coverage. The final material is typically obtained by direct evaporation under vacuum. Co-precipitation is the most common method of preparing Cu/ZnO based catalyst for methanol production from syngas[83]. This method can be coupled with an ultrasonic treatment stage to improve the dispersion[131]. Deposition-precipitation is conducted via vigorous stirring of the support material with the relevant metal solution with an assisting material such as urea or ammonia, followed by solvent evaporation by heating and calcination. It can also

be referred to as evaporation-induced wetness impregnation in case water is used as solvent with no other chemical aid. On the other hand, in case of porous supporting material usage, different methods such as infiltration or impregnation can also be used as described in Section 2.2.2 where SBA-15 modification techniques were described.

Cu based catalysts, as clear by the name, contain Cu as their main component in combination with promoters and supports[68,81]. Cu, in metal form, was discovered to be active in adsorbing and dissociating CO_2 and thus it is catalytically active for methanol production through hydrogenation of CO_2[68,99,142]. Cu has shown the highest methanol yield from CO_2 hydrogenation among other metals[96]. On the other hand, Cu has been the focus of methanol synthesis studies not only due to this high catalytic activity but also due to its low price, ease of handling and low risk to human health (toxic effects appear only if it is ingested in large amounts)[52,68].

The catalytic activity of Cu was earlier attributed to its metal phase, and the metallic surface area of Cu was claimed to be directly proportional to the catalytic activity[68], however later it was discovered that also the +1 oxide state is required which corroborates with the metal phase for catalyzing CO_2 conversion due to their synergistic effect[84,143]. Freshly synthesized Cu nanoparticles are typically a mixture of various oxidized forms of Cu, and unlike the reduced Cu metallic state, oxides are stable upon exposure to air. Therefore, storing and transporting catalysts comprising of Cu nanoparticles in oxidized form is a good strategy from a stability point of view. The Cu oxides on the material can be reduced to get +1 oxide (Cu_2O) and metal forms right before usage in CO_2 hydrogenation reaction[102].

The phase of the catalytically active species is not the only yield-determining parameter. There are other factors contributing to the activeness of the catalyst such as metal-promoter relationship[46,83,84,131,144]. In the following section, promoter types will be reviewed.

Promoter[53,68,86,99] is a modifier which can enhance the activity of a catalyst material, either by enhancing the activity of each site or increasing the number of active sites. The synergistic effect of multi metal oxide systems can improve the number of the active sites on the catalyst by introducing additional interface[46,90,109,111,145]. It was reported earlier that pure Cu is not sufficiently active to catalyze methanol formation through CO/CO_2 hydrogenation [143,146]. Therefore, it is crucial, from the activity and selectivity point of view,

to complement Cu with a suitable promoter to boost the CO_2 conversion efficiency. The choice of the promoter depends on the type of reaction and the targeted yield, selectivity, and conversion. More than one promoter can be used for a synergetic effect. In some instances, one promoter can also show both textural and electronic effects on the active phase. The supporting materials investigated so far are mainly binary and ternary oxides with different composition and morphologies. The most common reported promoters for Cu active phase in a heterogeneous catalysis of CO_2 hydrogenation to methanol and DME are ZnO, Al_2O_3, TiO_2, zeolites, ZrO_2 and SiO_2[68,99].

Zinc oxide (ZnO) is the most preferred electronic promoter for the Cu active phase for CO_2 hydrogenation reaction due to reports indicating its high efficiency[136]. This promoter is currently used in the commercial Cu catalyst for methanol production from CO_2 hydrogenation and also used in many scientific studies due to its beneficial properties for Cu. ZnO was observed to increase the dispersion and stability of the Cu metal phase and also contribute to the catalytic activity since the Cu-Zn interface is active for this type of reaction[68,83]. However, this hydrophilic phase can be quickly inhibited due to water produced during methanol and DME synthesis[84,135].

Alumina (Al_2O_3), is the most common support used for Cu/ZnO catalyst system for CO_2 hydrogenation to methanol[36]. It provides stability to the metal/oxide compounds[83]. However, it was also reported that due to its high concentration of Lewis acid sites, it attracts water and causes early deactivation of the catalyst[90,136]. On the other hand, due to its high surface acidity, Al_2O_3 is also known to catalyze methanol dehydration to DME and other hydrocarbons[68].

Titania (TiO_2), is typically used as a photocatalyst due to its redox property in the photo-excited state inducing water splitting reaction[147–150]. TiO_2 has been reported to catalyze CO_2 hydrogenation to produce methanol, alone or, as a promoter to improve the selectivity towards methanol by contributing to active metal sites[81,96,151]. It was also used as an additive to Al_2O_3 to improve the catalytic activity by minimizing the coke formation during the reaction. However, it requires a quite high temperature to operate at its optimum and therefore was never the primary choice for this reaction[136].

H-ZSM-5 has been typically used for methanol dehydration to DME as well as hydrocarbon formation due to its surface acidity[36]. However, due to possessing small pore diameter, H-ZSM-5 has a limited diffusion into the porous network[136].

Zirconia (ZrO_2), with its high stability under severe conditions (such as high T and P, reducing and oxidizing environments), is a very promising binary oxide catalyst support[68]. ZrO_2 was also shown to increase the catalytic efficiency of the active Cu phase for producing methanol by both syngas and pure CO_2 hydrogenation reactions[37,120,136,142]. The promotive effect of zirconia is mainly due to its ability to increase the dispersion of Cu metal and improve the active surface by providing additional sites on the catalyst system, both acid and base[37,68,86,90,99,142,144,152,153]. Zirconia was also shown to be better catalyst support compared to alumina due to its lower hydrophilicity since water poisoning of the catalyst is a bottleneck of such a reaction[90]. It can also ease the reduction capacity of CuO[135], and it has an affinity to CO_2 and thus can chemisorb and coordinate. This CO_2 affinity leads to carbonate formation on the Zr surface, and therefore it constitutes the perfect couple for the hydrogen coordinating Cu[68,91,154].

According to earlier reports, the catalyst systems with ZrO_2 are typically composed of randomly shaped nanoparticles of oxides prepared with co-precipitation method and therefore has exhibited only up to 200 m^2/g specific surface area[86,144,152,155,156]. However, studies that focus on testing different morphologies and states of zirconia to improve the support/promoter properties are very rare.

Silica has been reported as a high stability support for Cu active phase to be used in various hydrogenation and dehydration reactions[46,68,99,157] and it was shown to increase the methanol yield through CO_2 hydrogenation by providing additional positive surface charge due to the Cu-SiO_2 bonds at the interface[106,158,159]. Mesoporous silica can be prepared with a very high specific surface area (can be more than 700 m^2/g) and uniform pore size distribution enabling improved dispersion and controllable particle size of the active phase nanoparticles[53,59,147]. High surface area of the support is beneficial not only to obtain a large catalytically active metal surface but also for keeping the active sites isolated from each other which can otherwise interact with each other instead of gas phase reactant molecules[99]. It was demonstrated in an earlier study the proximity between active sites can cause interaction hindrances and thus diminish the activity of the catalyst[118] and since metals such as Cu tend to agglomerate in order to minimize their surface energy, choosing a favorable environment such as mesoporous silica for supporting Cu is crucial. The pores of mesoporous silica act as nano-shelters for Cu nanoparticles to prevent melting and sintering under high temperature[46,68,145,160]. On the other hand, silica can also be functionalized or doped with different atoms or molecules enabling functional

modifications[99]. The most common mesoporous silica types reported as catalyst support for Cu are MCM-41 and SBA-15[46,51,52,57,59,71,158].

4

DRUG DELIVERY

The term 'drug delivery' describes the means and methods of drug administration into the body for a targeted therapeutic outcome. Controlled drug delivery has been in focus with increasing interest in the last decades due to the possibility to individualize therapies and ease dose compliance with the ultimate goal of ensuring patient comfort especially when they are life-long such as insulin administration for diabetes[161,162]. Controlled drug delivery primarily relies on ensuring the administration of the right amount of a chosen drug to a target organ with the right dosage by enabling gradual release over time[163].

A pharmaceutical drug is the formulation of an active ingredient (drug) in its suitable dosage form and selecting an efficient and safe drug delivery system for this dosage form is a crucial factor for determining the pharmacological action of a drug and thus tuning the therapeutic profile[164]. Administration of a drug delivery system should also be safe, reliable and repeatable[165]. Development of drug delivery systems, which can entrap the drug molecules within their structure due to their target-specific morphology, is considered as an important topic not only in the development of an effective disease therapy but also in different areas such as food/cosmetic industry as well as gene delivery[166]. In some applications, it is also possible to load the drug in a carrier and charge it on an implant which is then placed into the body, e.g., dental or hip implants[164,167].

A suitable carrier can improve the drug dissolution in the body[69,168] by modulating the three main parameters of a release: location of the relevant site, drug concentration at this site (i.e., release rate) and duration of a chosen drug concentration at this site[165,169]. The

drug concentration at the target site should be within the therapeutic range which is defined as the region between the minimum effective concentration (MEC) and the minimum toxic concentration (MTC)[165] against a particular microbiological agent. Drug support can also provide protection for this therapeutic molecule under severe conditions such as rapid pH change on the gastrointestinal tract[166] and for ensuring a shelf life of a minimum two years for the drug it is carrying.

Drug delivery mechanism of a carrier can be qualified by its drug loading capacity and drug release profile. **Drug loading capacity** represents the amount of drug held by the unit weight of its carrier under certain loading conditions. **Drug release profile** is the time-dependent evolution of accumulated drug concentration in a release medium.

4.1. Drug delivery systems

Drug delivery systems can be classified through different parameters. The classification can be made according to the physical state of the drug carriers which includes solid, semisolid (i.e., ointment), liquid or gaseous, or possibly multiphasic systems[165]. Drug delivery systems can also be classified according to their route of administration which can be oral, parenteral (intravenous or intramuscular), transdermal (topical or rectal) or aerosol[164]. Drug administration from implants is considered as parenteral administration route. This method presents a unique advantage by enabling local drug delivery straight to the therapeutical site, which overcomes several challenges related to the conventional administration routes. For example, oral administration is well known to require quite high dosages of the drug to be able to reach the target site at desired concentrations. Another type of classification is based on the release profiles (Figure 4.1) which can be separated into two main branches referred as *immediate release* and *modified release. Immediate release* is the most conventional type of release profile that occurs by dissolution of the drug to the medium in a single and rapid action causing the drug concentration to quickly reach a maximum in the blood plasma and then to decrease. This profile is typically found in conventional oral dosage forms (e.g., paracetamol pills). *Modified release*, on the other hand, involves the release of a drug in a delayed or extended manner. *Delayed release* allows the release of a drug with a certain delay after administration of the drug. *Extended release* can be performed by either *sustained release* which enables release over time or by *controlled release* which extends the release in such a way that the drug concentration level in the plasma stays constant during a chosen duration[165].

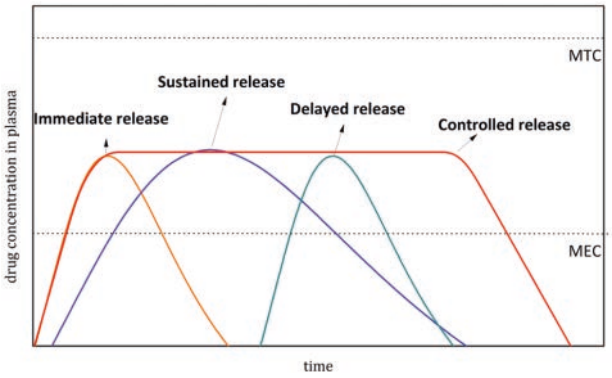

Figure 4.1. Drug release profiles

Controlled drug delivery systems are capable of maintaining a constant drug concentration in the release medium, i.e., relevant site of the body, for the adequate time frame required for the therapy. Thus, a significant amount of research on pharmaceutical technology has been devoted to this issue. The controlled drug delivery has been mostly concentrated on polymeric materials and also some hybrid inorganic material systems[5].

In controlled drug release, many strategies have been employed such as varying the morphology or physicochemical properties of the drug carrier to achieve good control over the release kinetics. Also functionalizing drug carriers is a significant strategy for enhancement of the drug-carrier interactions and thus limiting the drug release rate[166].

4.2. Drug release models

Drug release profiles strictly depend on the behaviour of the drug carrier in the release medium which can either be biodegradable or biostable (un-dissolving)[170]. The diffusion-controlled systems typically employ un-dissolving drug carrier[171], and several theories/kinetic models can be used to describe this type of release from immediate and modified release dosage forms[172]. Most of these models are based on Fick's diffusion equation under proper boundary conditions, and the most significant models for non-degrading drug delivery systems include zero-order release, first-order release, Higuchi, Korsmeyer-Peppas, and Weibull[170].

Zero-order release[173] is only valid when the drug release rate is constant, i.e., release rate is independent of the drug concentration in the release medium. It represents a linear drug accumulation over time where the release time is 'infinitive' [171].

$$M_0 - M_t = k_0 t \qquad (4.1)$$

where the M_t is the amount of drug released in time t, M_0 the initial drug amount, and k_0 the zero order release constant.

First-order release[173] is valid when the release rate is dependent only on the drug concentration in the release medium.

$$ln(\frac{M_0}{M_t}) = kt \qquad (4.2)$$

where the M_t is the amount of drug released in time t, M_0 the initial drug amount, and k the first order release constant.

Higuchi model[5,170,174] is valid when the drug is homogeneously distributed in a nondegradable drug delivery system which acts as a planar surface (monolithic delivery). It is good at estimating the cases where the drug concentration is much higher than the solubility limit of the drug.

$$M_t = k_H t^{1/2} \qquad (4.3)$$
$$k_H = [2Dc_{ini}c_s]^{1/2} \qquad (4.4)$$

where the M_t is the amount of drug released in time t, k_H the Higuchi dissolution constant, D the diffusion coefficient, c_{ini} the initial drug concentration in the medium and c_s the drug solubility.

Korsmeyer-Peppas model[5,170,173] is a more comprehensive model for drug release from a matrix. It represents diffusional release and typically used for polymeric systems.

$$\frac{M_t}{M_\infty} = kt^n \qquad (4.5)$$

where the M_t is the cumulative released drug mass at a time t, M_∞ the cumulative released drug mass at the time infinity (maximum released amount), k the release rate constant, t release time, and n the release exponent. The release exponent here mentioned hints whether the release follows Fick's law or displays a more complex behavior.

Finally, **Weibull model**[175,176] is typically suitable for drug release from a matrix where the diffusion is in effect. It was earlier shown that this model can fit a release profile from mesoporous silica materials where not only diffusional release took place, but also desorption[177].

$$\frac{M_t}{M_\infty} = 1 - e^{-k(t-t_l)} \qquad (4.6)$$

where the M_t is the cumulative released drug mass at a time t, M_∞ the cumulative released drug mass at the time infinity (maximum released amount), k the rate constant, and t_l the lag time for a dissolution process.

4.3. Drug supports: nanocarriers and antibacterial agents

Pharmaceutical nanotechnology is a new area focusing on the development of drug delivery vehicles with advanced properties[178] in nano-level, i.e., nanocrystalline and nanostructured materials.

One of the main aims of this discipline is to achieve nano-sized or atomic level modifications to the previously studied drug delivery systems in order to improve drug bioavailability and develop more patient-friendly treatments by reducing the total dosage and side effects[7,164,179]. There are many nanotechnological drug delivery systems studied so far, including inorganic materials (such as silica, carbon, metals or polymers) as well as biological agents (such as chitosan)[180].

Nanoparticles, meanwhile, came to attention of the scientific community due to their high stability in the release medium[5,181], high surface-to-volume ratio leading to high adsorption capacity not only for drugs but also for genes, proteins, and probes[7,182], small enough size to penetrate into the smallest blood vessels and cells and still deliver a suitable amount of drug[164,169,180], controllable morphology and surface properties, and their biocompatibility[164,180]. Economically they are favorable too since the same nanoparticle synthesis method can be used to produce different morphological properties and also they might be applied in many drug administration routes including oral, intravenous or topical and even for drug storage[69,161,165].

Mesoporous materials became popular as drug delivery matrices due to their high surface area and pore volume, narrow pore size distribution and pore size range of 2-50 nm which is suitable for hosting many different sized drug molecules[183,184]. They are not only suitable for drug delivery, but also for long-term drug storage[5].

Mesoporous silica has been proposed as an active drug delivery system due to its biocompatibility[65,176,183]. Its ordered network of bi-axially aligned pores covered with

silanol groups provide controllable mass transfer of fluids into and out of the ordered network, enabling good control of drug loading and release[8,183].

Silica sol was primarily studied as a drug carrier. However, mixing the drug molecules yielded unhomogeneous distribution of the drug in the carrier which resulted in inconsistent release profiles between different batches[5,185]. Mesoporous silica has been a good biocompatible alternative to the traditional systems due to its high hydrolytic stability[186].

The use of mesoporous silica for drug delivery studies was pioneered by Vallet-Regi et al. with a report from 2001 where they showed the drug delivery feature of MCM-41[185]. Mesoporous silica is a suitable candidate as a drug delivery system due to its ordered pore packing structure, high specific surface area, and large pore volume as well as its convenience of surface functionalization due to silanol rich domain[183]. They can accommodate drugs with a hydrophobic and unstable character as well as the ones for which the cellular uptake is a challenge, such as the cancer drugs[7]. They are also favorable candidates for targeted delivery by functional groups which require the porous system in an entirely homogenous structure[183]. After MCM-41, larger pore mesoporous silica types such as SBA-15, SBA-16, and SBA-1, as well as hollow mesoporous silica spheres were evaluated as drug carriers, but due to good control over the characteristics, the focus stayed on SBA-15[5].

SBA-15 is a bioactive molecule with a pore size range of 5-15 nm and therefore has a considerable potential for hosting large drug molecules[5,183]. Its well-defined cylindrical pores are packed in a hexagonal order, and they run parallel to each other which is a perfectly aligned morphology for controlling the drug loading and release behaviour[65,177,182]. These properties are similar for MCM-41, which was the start of many drug release studies. However, there are some reports suggesting lack of bioactive property of MCM-41[5] unless functionalized with a biocompatible element such as phosphorus[5,187]. Moreover, the presence of –OH end groups on the well-defined surface of the SBA-15, its high specific surface area, and pore-connectivity make SBA-15 favorable for loading and controlled release of a drug depending on the ionic attractions[5,184,188]. SBA-15 has especially shown to interact with positively charged molecules, but even without strong electrostatic forces, it can still hold a considerable amount of a drug by physical mixing and capillary forces due to its extensive porous network[7,69,189]. Therefore SBA-15 is quite advantageous for drug delivery applications. SBA-15 has good hydrothermal and chemical

stability which enables long-term survival under harsh body conditions such as rapidly changing pH[5]. Bulky mesoporous structures were earlier determined to be limited to their capacity of the drug amount they can carry. For this reason, some studies are leaning towards hollow mesoporous spheres which perform as a reservoir system during the diffusional drug release[171,183]. Therein, a high pore volume and large SSA material such as SBA-15[190] with homogenous monodispersed rod morphology can spare the scientists from developing hollow structures which typically have exhaustive multi-step synthesis routes and a great challenge to have a good synthesis yield with homogeneous powder morphology[191,192].

It has been shown in earlier studies[16,21] that there are several ways of modifying the adsorption performance of SBA-15 by altering physicochemical properties of SBA-15, and this can provide good control over the drug release kinetics. Moreover attaching functional groups on its –OH terminating surface is a very convenient way to increase the drug attachment[193]. One very significant functional group studied so far is amine group (NH_2^-) which has influence on the drug loading potential and release behavior of SBA-15[5,188,194,195]. It was shown before that amino functionalized SBA-15 is capable of a zero-order release which can be favorable especially for local delivery of drugs to repair bone defects[183]. In some cases, functionalization can be comprised of certain chemical groups that control the pore openings and regulate the encapsulation as well as the release of the drug loading[190]. These chemical groups can respond to different stimuli such as lights, pH or temperature and can change their configuration and they are referred as gate-keepers or gate-like ensembles[65,183,196,197]. This type of functionalization can become quite critical when a sensitive tuning in targeted delivery is required, especially in treatments such as cancer[186].

Moreover, SBA-15 is a potential dental filler which is promising for local delivery in dental applications involving dental composites[198]. It has been a common practice to utilize spherical nonporous silica particles as dental fillers in the composite materials[199]. The idea of using porous glass fillers was first introduced in 1976 by Bowen *et.al.*[200]. Later it came to attention that the large pores of SBA-15 can host molecules with a wide range of sizes and morphologies and can release them into a suitable medium by diffusion[5]. The high pore volume and large specific surface area of SBA-15 allow minimization of the amount of SBA-15 powder to be loaded in a dental composite since this concentration variable is also directly proportional to the collective toxicity of the drug delivery system[183]. Also, it was

shown earlier that SBA-15 and MCM-48 allow the formation of an apatite-like layer which also indicates a potential use in implantology[10,167].

The kinetics of the release from a mesoporous network depends a lot on the morphology and physical properties of the carrier material. Although this was investigated in earlier studies, some more research devoted to this is of interest, since kinetics can be much different when the material demonstrates considerably larger pores but also the high specific surface area. There is no universal view in the literature regarding the drug release kinetics of mesoporous silica, and earlier reports have revealed different release profiles. In these studies, it has been shown that the kinetics of the drug release from mesoporous silica can follow Korsmeyer-Peppas model[5], zero order release[201] or Higuchi model[5] depending on the system. On the other hand, there are also many studies which indicate that there are two phases of drug release from mesoporous silica and therefore such a model needs two exponential terms to form the formula to represent different phases. The first phase is typically a burst release of the drug molecules that are free in bulk form within the carrier without being adsorbed to the carrier (physically encapsulated molecules) and the second phase is where the adsorbed molecules of the silica walls are desorped (chemically encapsulated molecules)[163,202,203]. The drug-drug interactions are dominant in the first phase whereas drug-carrier interactions become dominant in the second phase[203]. Depending on the electrostatic attraction between the drug and the carrier mesoporous silica, the significance of these phases can change, e.g., with a type of a drug weakly attached on the silica surface, the second phase can be ignored or not existent[202]. A double exponential function (Eq. 4.7) was reported by Demuth *et al.,* which can be observed to be based on Weibull model, to explain this two-phase behavior for a cationic dye attached on a mesoporous silica[5,203].

$$\frac{M_t}{M_\infty} = P_1(1 - e^{-k_1 t}) + P_2(1 - e^{-k_2 t}) \quad (4.7)$$

where the M_t is the cumulative released drug mass at a time t, M_∞ is the cumulative released drug mass at the time infinity (maximum released amount), P_1 and P_2 are the percentages released during phase 1 and 2, k_1 and k_2 are the release rate constant of phase 1 and 2[203]. It was also observed earlier that for certain mesoporous silica-drug molecule coupling, the absorption could be strong enough not to allow full release of the loadings[5].

Zirconia (ZrO_2) is a biocompatible inorganic ceramic material which shows high stability under high temperature, pressure, oxidizing environments and changing pH conditions

and thus it is being investigated for bone implant applications as well as dentistry and dental implantology[168,204]. Moreover, it was studied as a drug and gene carrier[168,205]. Zirconia is currently in clinical use for the preparation of hip implants and suggested as a new generation of dental implants to replace or complement titanium to form hybrid implants for the clinical practice. This function of zirconia originates from the fact that it is osteoconductive, i.e., promotes bone formation when it becomes in contact with the injured bone, it helps to inhibite plaque formation, and improves soft tissue interactions, thus promotes periointegration[204].

On the other hand, when zirconia enters the body, it can get reduced in the cells by mitochondria and therefore can cause an increase in the ROS (reactive oxygen species) such as superoxide $^{*}O_2^-$, and hydrogen peroxide H_2O_2. These species can cause cytotoxicity, therefore, the form and amount of ZrO_2 taken into the body are crucial[205–207]. The ZrO_2 concentration limit that can cause toxicity in the cells due to elevated oxidative stress was earlier published as 250 μg/ml[168,205]. The literature results have no common ground on the toxicity of Zr, and the debate is still going on. However, it became explicit that, the toxicity differs with test conditions as well as the physical form of zirconia which effects its oxidizing (getting reduced) properties[204]. For example, nanoparticle morphology can cause higher toxicity than the case where it is doped in the framework of a stable amorphous matrix. Doping method can overcome the oxidizing tendency. However, literature is lacking these type of trials. On the other hand, the oxidizing properties of ZrO_2 can be additionally advantageous in the drug delivery applications due to its contribution to antibacterial effect[206,208].

Copper (Cu) has been utilized by the humankind since 5000s BC and was reported in the oldest medical record the Smith Papyrus written until 2600s BC to function for sterilization of chest wounds[209]. Cu was first acknowledged to be a material with antibacterial properties in the 1800s when the scientists realized that Cu mine workers were immune to cholera and since then it has been used in medicine widely[209,210]. Cu, either in metal or oxide form, is a cheaper alternative to noble metals (gold or silver) for several antibacterial and antifungal applications such as preparation of dental cements, medical implants, and producing antibacterial coatings/materials to be used in public places such as hospitals, transportations vehicles, and food packaging[209–215].

In views of conferring or enhancing its antibacterial activity, Cu can be used as nanoparticles to obtain high specific surface area. The antibacterial activity of Cu

nanoparticles at the size range of 2-10 nm was shown to have antibacterial activity against both gram positive and gram negative bacteria[179,213]. Moreover, Cu nanoparticles, compared to Cu^{+} ions attached on the surface of the carrier, have higher stability under body conditions (e.g., changing pH) leading to slower ion release from the nanoparticles which provides a long period of antibacterial activity and a lower potential of being toxic against mammal cells[199,211–213,216]. Also, their long lifetime can enable them to be used in contact therapies such as wound plaster[213].

The antibacterial activity of materials such as Cu or Ag has become more attractive especially due to the increasing resistance of microorganisms to various broad spectrum antibiotics and antiseptic chemicals[217]. Due to their bacterial toxicity, Cu nanoparticles were used as a complementary agent to antibacterial drugs or antibiotics in many drug delivery studies[216,217].

The antibacterial activity of Cu nanoparticles can be both a contact-driven or ion releasing process which runs by cell wall destruction, production of ROS in the bacterial cells and DNA degradation leading to cell death[209,212,216,218]. The copper ions released from each nanoparticle are the toxic agent, and its release rate can determine how harmful the administered material is to bacterial cells and how safe it is to mammal cells[216].

Chlorhexidine digluconate (CHX) is an organic antibacterial and antiseptic drug which is well-established in dentistry and successfully used in the clinic for more than 20 years, especially for the treatment of periodontal deseases[199,219,220]. Moreover, it is used in handwashing and oral products due to its broad spectrum effect and low cytotoxicity which minimizes skin irritation[220,221]. It has both antibacterial and bacteriostatic activity, and it is effective against many gram-positive and gram-negative bacteria as well as fungi[219,222], but it can not kill bacterial spores or myobacteria[221,223]. It is bactericidal by contact to which it is attached to the cell membrane of the microorganism. Afterwards, it goes through an easy uptake by bacteria by diffusion and it attacks the inner membrane causing the bacterial membrane disruption and thus the intracellular contents to leak. The second phase starts where the high concentration of CHX in the cell can cause the cellular contents to coagulate[221]. Chlorhexidine is a cationic molecule, and its antibactericidal property is originated from this charge which reacts with the lipopolysaccharides which contain negatively charged phosphate groups[222]. This molecular charge of CHX is also a valuable characteristic for loading it into any acidic carrier[219].

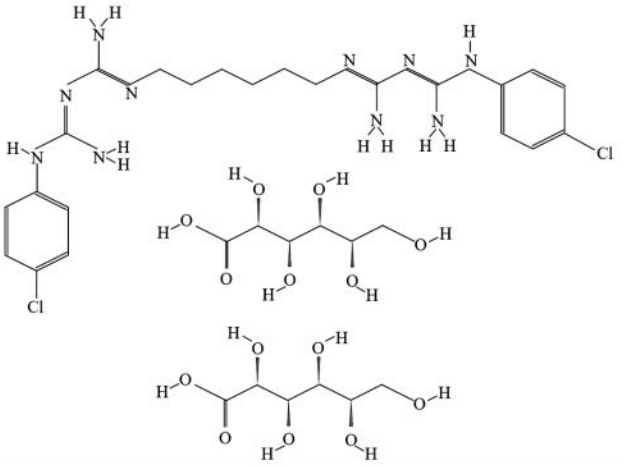

Figure 4.2. Chlorhexidine digluconate

Doxycycline Hyclate (Doxy) is a semi-synthetic wide spectrum antibiotic from tetracycline family which is effective against periodontal pathogens and shows anti-inflammatory effect[176,224].

The topical administration of Doxy has been demonstrated to improve the management of periodontitis via systemic administration because by topical administration the amount of antibiotic delivered on-site is much higher, it is possible to apply it one time only and thus preventing any systemic side-effect[224–226].

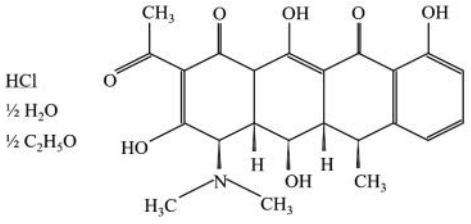

Figure 4.3. Doxycycline hyclate

5

ANALYSIS METHODS

The characterization of mesoporous silica can be done with a wide range of techniques. The morphological identification can be made by imaging, more explicitly scanning electron microscopy (SEM) and transmission electron microscopy (TEM). The porous network is investigated with physisorption and small angle x-ray diffraction methods. Fourier transform infrared spectroscopy (FTIR) is utilized for identification of the silica network whereas Synchrotron radiation and in situ horizontal attenuated total reflectance (ATR) can help clarify the mesoporous silica network formation mechanism. The surface acidity is assessed by NH_3-temperature programmed desorption (TPD) measurements.

Using SBA-15 in applications, however, require slightly different analysis methods. In order to analyze the resulting gas from the CO_2 hydrogenation, gas chromatography-mass spectrometry (GC-MS) were used in combination to get quantitative results. In situ diffuse reflectance infrared Fourier transform spectroscopy (DRIFTs) gives insights to the reactions occurring on the catalyst surface during CO_2 hydrogenation.

In drug delivery applications, the drug loading amount can be measured by thermogravimetry (TG), and drug release amounts can be calculated from the drug concentration in the release medium detected by a UV spectrometer. The antibacterial properties of a material are typically measured with agar diffusion test to obtain qualitative information and the microplate technique to obtain quantitative information.

5.1. Physisorption

Physisorption (physical sorption) is the attachment of free gas molecules to the surface atoms of a material by weak van der Waals forces. A gas, at or near its boiling point, is used to expose the sample to different pressures, which are typically lower than the vapor pressure of the gas itself. The applied gas pressure is increased stepwise. During each step, the pressure is held constant to allow for adsorption and for the adsorbent temperature to equilibrate. The pressure change, as well as the amount of the dosed gas, are used to calculate the adsorbed amount which is then plotted against the adsorptive pressure to obtain isotherms[227]. Employing this technique, it is possible to determine the specific surface area and pore size distribution of porous materials by using nitrogen gas[228].

There are six types of isotherms according to the IUPAC classification[2,229], and they are schematically depicted in Figure 5.1. They are based on multilayer coverage of gas molecules forming on the adsorbent. The first stage is monolayer adsorption, and it occurs when the surface of the mesoporous material is covered with one row of gas molecules. Then the gas molecules accumulate layer by layer forming a multilayer. As the final step of adsorption, the condensed gas molecules fill up the rest of the empty space. The desorption occurs in the opposite direction.

Type I is typically observed for microporous materials. Indeed, due to micropores with a small diameter, the quantity of the adsorbed gas shows a fast increase at low pressures which approaches an equilibrium value as the accessible pores are filled. Type II isotherms represent non-porous or macroporous adsorbents where monolayer is formed until the first knee point, and the multilayer coverage goes up high as the partial pressure increases to high values after the second knee point. The type III isotherm occurs when the adsorbent-adsorbate interaction is very weak. Due to this reason, the gas molecules accumulate on the very few active sites on the adsorbent surface, and thus full layer coverage cannot be achieved. The mesoporous materials are represented by type IV which starts similar to type II but also shows a hysteresis due to capillary condensation. This phenomenon occurs with the gas condensing in the pores at pressures higher than the saturation pressure which causes delayed condensation, and finally the condensed molecules fill the pores. During desorption, however, the liquid stays in the pores until the equilibrium vapor pressure is reached, and at the right time, the gas molecules evaporate their way out of the pores. The type V isotherm is similar to Type III where the adsorbent-

adsorbate attraction is very weak and a capillary condensation occurs. Finally, type VI is when multilayer gas deposition occurs on a nonporous or a very uniform surface[2,229].

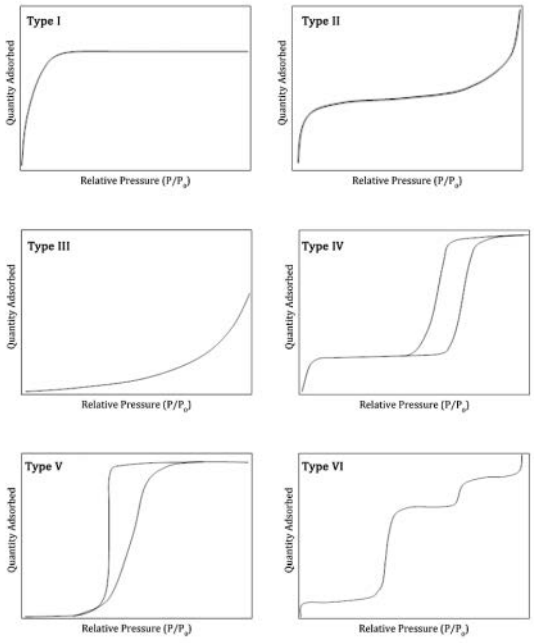

Figure 5.1. Isotherm types

Hysteresis can occur in 5 different shapes depending on the pore shape of the material (Figure 5.2). H1 loop occurs for uniform, cylindrical mesopores as in MCM-41 or SBA-15 where all the pores are filled and emptied at once. H2 is typically observed when the sample has pore blockings or bottle-necks causing percolation of the liquid. H3 loop typically represents a sample made up of platelet-shaped particle aggregates or slit-shaped pores with pore blockings. H4 is when the sample is made up of aggregated crystals of zeolites or slit-shaped pores without any pore blocking. Finally, H5 loop belongs to the samples where there are both blocked, partially blocked and open pores [229,230].

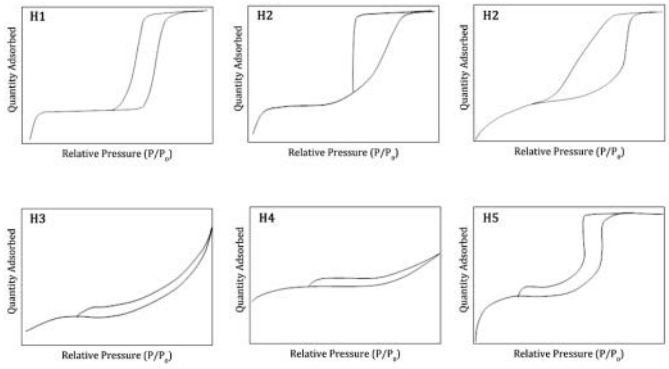

Figure 5.2. Hysteresis loops

The surface area is typically calculated by the BET (Brunauer-Emmet-Teller) method[231]. This method includes using a multilayer coverage capacity to calculate the accessible surface for the gas molecules. The number of molecules forming the first layer can then be used with a molecular cross-section area to find the whole surface area. This theory assumes that the surface active sites are identical and adsorbed molecules do not interact with each other[1,229].

Pore size distribution is typically calculated by the KJS (Kruk-Jaroniec-Sayari) method for mesoporous silicas with ordered and cylindrically-shaped pores[232,233]. This method depends on BJH method which was determined to underestimate the pore size, and thus KJS method includes a correction to BJH method. BJH method assumes that all the pores are cylindrical and it calculates the pore radius by taking advantage of the capillary condensation from the Kelvin equation which is the basis of explaining partial pressure dependence of the curvature at the liquid-gas interface. Later, by comparing the XRD data of the MCM-41 type of mesoporous silica with the sorption data, the BJH method was improved[228,229,232,234].

5.2. Temperature Programmed Desorption

Temperature programmed desorption (TPD) is a chemisorption (chemical sorption) based technique. Chemisorption is the attachment of free gas molecules to the surface atoms of a bulk material by covalent or ionic bonds. It is a common method to analyze the

surface properties of solid catalysts and their affinity to the gas molecules in a heterogeneous reaction system. It is irreversible and a monolayer activity[235].

During TPD measurements a probe molecule, such as ammonia or carbon monoxide, is used to determine the properties and the density of the surface acid sites of a solid catalyst. A solid catalyst of a known weight is first saturated with the adsorbate flow at a temperature typically between 100-150°C for a sufficient amount of time to ensure a complete coverage. Afterwards, physisorbed molecules are removed from the catalyst surface by an inert carrier gas flow. The remaining chemisorbed molecules are then forced to desorb by increasing the temperature. While heating, the adsorbate concentration in the carrier stream is measured by using a thermal conductivity detector. The acquired TPD spectra are normalized with the weight of the sample powder and plotted versus temperature. TPD spectra exhibit peaks at specific temperatures at which the adsorbate molecules are detached from the acid sites. Therefore, stronger is the acid site, higher is the temperature required for desorption[236–238].

5.3. X-ray diffractometry

Electromagnetic radiation with a wavelength of about 10^{-10} m is called X-rays. When X-rays penetrate matter, they can interact with electrons and scatter, be emitted or absorbed in specific ways depending on the nature of the interacting atoms. Diffracted x-rays can be analyzed to determine the atomic structure of a crystalline phase. The diffraction technique requires long-range periodicity of the lattice planes in the material of interest. These planes cause scattering due to constructive interference, and this can be shown with a relationship between the scattering angle and lattice spacings called Bragg's law[239]:

$$n\lambda = 2d_{hkl}sin\theta \qquad (19)$$

where λ is the wavelength of the x-ray beam, d_{hkl} is the lattice spacing, θ is the scattering angle and n is the order of reflection.

Small angle x-ray diffraction is conducted in transmission geometry for ordered powders by analyzing the diffracted beam as a result of an incident beam striking the sample at a shallow angle. The diffracted angle of the incident beam (2θ) is typically recorded between 0-2.5° for mesoporous silica. In this angle range, the hexagonal pore stacking

system of SBA-15 results in at least three peaks corresponding to 100, 110, 200 when using Cu radiation.

The phase and size of the nanoparticles with well-defined crystallographic planes can typically be determined by x-ray diffraction at angles between 20-60°. Crystallite size, i.e., nanoparticle size for a single crystal material, with a size between 5 and 100 nm can be calculated by the Scherrer equation, utilizing the full width half maximum of the strongest peak of the material.[240,241]

5.4. Electron microscopy and energy dispersive x-ray spectroscopy

Electron microscopy enables imaging by projecting a beam of accelerated electrons onto the sample. In Transmission Electron Microscopy (TEM) the electrons that penetrate a specimen, are transmitted through the sample, and the resultant beam is recorded at the exit by suitable lenses whereas in Scanning Electron Microscopy (SEM) the reflected (secondary) electrons are used for imaging. TEM is more suitable for thin samples, while SEM is typically used for thick or very absorbent samples where electrons cannot be transmitted properly[242]. Dark-field images can be produced by TEM method by using only the diffracted electrons and avoiding the direct beam by an objective aperture. This method can provide enough contrast between different crystal structures[87]. Energy dispersive x-ray spectroscopy technique (EDS/EDX) is a common method for determination of the atomic content of a sample and it relies on the emitted x-rays from the sample which have a characteristic energy depending on the atomic content of the sample. This measurement is typically conducted with an SEM or a TEM equipped with an integrated x-ray detector.

5.5. Infrared spectroscopy [FTIR, DRIFTS, and ATR]

Infrared spectroscopy (IR) is a technique to analyze the presence of atoms, molecules and molecular interactions which are active under infrared beam, i.e., absorb/emit the IR beam. These vibrations include mainly stretching (bond elongation) and bending (bond angle change). IR spectroscopy relies on these vibrations to get excited under IR radiation and change their energy levels. As a result of this energy adsorption, less energy from the

incident radiation is transmitted at the relevant wavenumber which appears as peak formations on a spectrum. With *Fourier transform infrared spectroscopy (FTIR)*, the main beam is split, and the partial beams are reflected back to the splitter where they recombine. The interference of the partial beams is interpreted in an interferometer by the Fourier transformation technique [243].

Attenuated total reflectance (ATR) employs an internal reflection element, e.g., a crystal, with high refractive index enabling multiple reflection of the IR beam while going through this element. During that time, the beam is absorbed by the sample, and finally, the attenuated beam is measured (Figure 5.3). It is typically utilized to measure samples in liquid or solids that produce very strong peaks with the transmission IR technique[243].

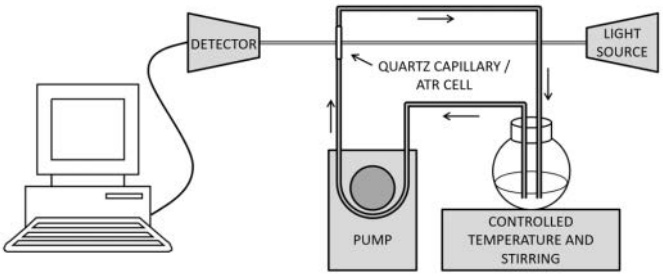

Figure 5.3. ATR setup schematic

In situ diffuse reflectance infrared Fourier transform spectroscopy (DRIFTs) is performed in a drifts cell which enables reflection of the beam over a solid sample(Figure 5.4). When the beam hits the sample, it is reflected by specular and diffuse reflectance. Specular reflectance occurs when the reflected beam is equal to the incident beam, which is valid for flat surfaces. The diffuse beam, however, is observed when the reflected light is scattered due to a rough surface causing various reflection angles. A rough sample can absorb a huge amount of the beam in case of transmission mode, and therefore the DRIFTS method is quite sensitive compared to traditional FTIR and thus is a convenient method of determining surface groups on a catalyst during a reaction[243–245].

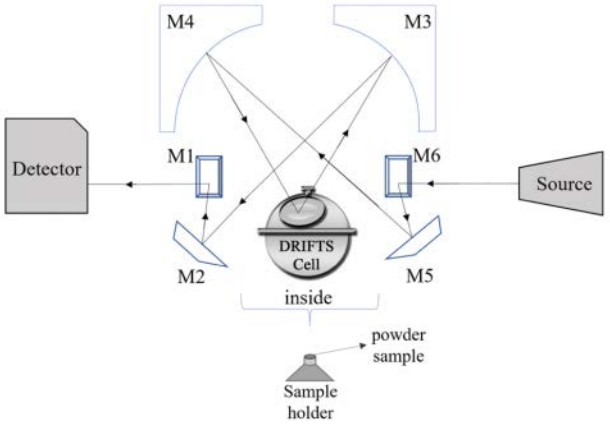

Figure 5.4. DRIFTs setup schematic. M1-M5 represent the mirrors in a specific order from detector towards the source.

5.6. UV/vis spectroscopy

UV/vis spectroscopy works by exposing the material of interest (typically dissolved in a solution) to a beam in the UV and visible range and detects the transmittance/absorbance by the measured material due to electron excitation. The resulting change in the beam is reflected through the detector and outcome is presented as a spectrum where peaks/bands give clues regarding molecular structure[246]. The most common use of this method is in the determination of the concentration of a substance in a liquid such as metal ion or a drug molecule.

5.7. X-ray photoelectron spectroscopy

X-ray photoelectron spectroscopy (XPS) is a surface-sensitive analysis technique that measures the elemental composition of the top surface (typically 1-10 nm) and provides information regarding the chemical state of the elements that compose the material being analyzed. XPS measurements are conducted in vacuum by irradiating a material with an X-ray monochromatic beam (commonly Al Kα or Mg Kα), which causes photo-emission of core-level electrons. As a result, the kinetic energy distribution of these emitted electrons is measured and used to identify and determine the concentrations of the elements present[247,248].

5.8. Gas chromatography and mass spectrometry

Gas chromatography is an analysis method where a gas mixture is separated into its components by a stationary phase (capillary column) by using their different affinity to the analytes, and each component is identified/quantified. The sample gas mixture in question is transmitted through the detector with a non-polar and non-reactive carrier gas such as Ar, He, and H_2. There are many different types of GC detectors, and they have their specific operation principle depending on a physical property of the molecules. For example, thermal conductivity detector (TCD) operates by measuring the changing thermal conductivity of the flowing gas and therefore determines the concentration in the gas while flame ionization detector (FID) burns the input gas with H_2 and gets its signal from the mass of the formed ions.[249,250]

Mass spectrometry (MS) provides identification of the components in a mixture by measuring the mass dependent deflection of the ionized molecules from the sample[251]. An ion source is employed to produce ions from the entering molecules. These molecules undergo fragmentation into radicals and ions when exposed to the ion flux from the ion source. Finally, the ions from the sample are passed through an electric field that deflects them differently depending on their kinetic energy. The abundance of ions are grouped according to their mass-to-charge ratio and presented as a bar graph which provides the mass-to-charge ratio of the species within the sample that is fed into the mass spectrometer[251,252].

5.9. Thermogravimetry

Thermogravimetric analysis is done by changing (typically elevating) the ambient temperature of a material gradually and measuring its mass over time. The measured sample is typically a solid. As it is heated, desorption, phase transition and thermal decomposition can occur. It is a destructive method which can be used for quantification and determination of the composition of materials, as well as their water and solvent content, impurity levels, and the thermal stability[237].

6

SUMMARY AND DISCUSSIONS OF THE PAPERS

The papers appended to this thesis focus on synthesizing hybrid materials based on mesoporous silica for catalysis and drug delivery applications.

6.1 Paper 1

Synthesis of Cu-infiltrated Zr-doped SBA-15 catalyst for CO_2 hydrogenation into methanol and dimethyl ether

In **Paper 1**, a rapid sol-gel route[15] was used to synthesize a Zr-doped SBA-15 matrix with Cu nanoparticles grown on its surface. The effects of Cu and Zr modifications were investigated from a chemistry viewpoint, and the catalytic efficiency in a CO_2 hydrogenation system was evaluated.

Zr-doped SBA-15 materials (Zr-SBA-15) demonstrated very similar porous network as for SBA-15 with additional Zr-O-Si bonds with an overall Si/Zr atomic ratio of about 10. Zr doping has yielded pore size increase from 11 to 15 nm while the SSA remained constant around 700 m^2/g. The particles for both SBA-15 and Zr-SBA-15 were rod-shaped, but wider in case of Zr doping. This structural difference was determined to be due to the decrease in F^- ion concentration in the solution caused by the Zr salt addition which otherwise acts as a catalyst in SBA-15 formation. By changing the static duration in the synthesis and the hydrothermal treatment conditions, it was observed that the pore

characteristics of the Zr-SBA-15 could further be altered. When the synthesis catalyst salt NH_4F was changed to NaCl the particle morphology was evolved to spheres due to slower formation rate in the presence of Cl^- ions compared to F^- ions. Cu nanoparticles grown on Zr-SBA-15 were determined to have a smaller average size compared to the ones grown on SBA-15. The reason for the improved Cu distribution in the presence of Zr is ascribed to the increase in the number of acid sites on the Zr-doped silica surface. In both cases, various oxidation states of Cu (Cu^{2+}, Cu^{3+}, and Cu^+/Cu^0) were detected to coexist in the sample despite reducing the samples under H_2 flow at high temperature. On the other hand, Zr was detected only in Zr^{4+} oxidation state.

The Cu-Zr-SBA-15 material was catalytically active for selective CO_2 hydrogenation to methanol and DME with 15% CO_2 conversion at the end of 5 days at 250°C and 33 bars, whereas SBA-15 and Zr-SBA-15 have shown less than 1% CO_2 conversion. Moreover, the Cu-SBA-15 material yielded a CO_2 conversion lower than 1% which demonstrates the importance of improved acidity with Zr existence in the mesoporous framework. The final conversion was still increasing after 5 days which indicates that a higher conversion can be expected from the Cu-Zr-SBA-15 catalyst at improved reaction conditions.

6.2 Paper 2

Effects of the chemical state of mesoporous CuO_x-Zr-SiO_2 catalysts on CO_2 hydrogenation

In **Paper 2**, the investigation of the synthesis conditions for Cu-Zr-SBA-15 catalytic nanoassembly, which started in **Paper** 1, was taken one step further by altering the chemical state of the catalyst with different silica precursors, and Cu loading procedures and observing the impact of this alteration on the catalytic activity. The tested silica precursors were tetraethyl orthosilicate (TEOS) and sodium metasilicate (SMS) whereas the experimented Cu loading methods were infiltration (Inf) and evaporation induced wetness impregnation (EIWI).

The Zr-SBA-15 particles synthesized with SMS were observed to yield wider particles, i.e., platelets compared to TEOS which yielded rods. This was attributed to the NaOH occurrence with SMS hydrolysis which increases the dissolution of the PEO chains of the micelles in the water media. The improved PEO solubility causes easier entanglement of

the PEO chains in the solution, and thus, the micelles and early-stage particles aggregate to become wider. On the other hand, Zr-SBA-15 produced with SMS showed lower microporosity also causing lower SSA. The dropped microporosity is due to the silica clusters being readily formed in the pre-hydrolized SMS which cause a rapid silica formation. As a result, the silica network formation terminates before PEO chains can penetrate into the silica walls. This rapid formation of SMS based Zr-SBA-15 has shown its impact also on the pore size. When SMS was used, the mesopores were observed to have smaller diameter since there was not enough time for heptane to penetrate the centers of the micelles to cause swallowing and pore enlarging, as in the case of TEOS based Zr-SBA-15. Moreover, TEOS can also act as a swelling agent causing further pore enlarging which is not the case for SMS. The use of SMS as the silica precursor also resulted in weaker bonds of the Zr atoms to the SiO_2 framework. The Cu reduction and re-oxidation were detected to be more efficient for SMS particles compared to TEOS particles. This is attributed to the weaker surface interaction of SMS with the Cu NPs compared to TEOS which facilitatess the reduction efficiency of the Cu nanoparticles. Using TEOS as the silica precursor in the Cu-Zr-SBA-15 catalyst was shown to provide a higher concentration of surface acid sites which ultimately results in a higher total CO_2 conversion compared to SMS.

As for the Cu infiltration methods, Inf method has yielded lower Zr content, smaller surface as well as less surface -OH groups compared to EIWI catalysts. Also, the reaction results have demonstrated that the Inf method promotes higher selectivity for DME than methanol. This is attributed to the higher strength of the medium acid sites of Inf which have more affinity for methoxy than the weaker ones which can adsorb hydrogen. As the surface methoxy concentration becomes higher for Inf methods, DME can be formed from two surface methoxy groups interacting with each other. It was shown in this paper that the medium acid sites were determined to be the most effective among the others in both activity and selectivity in CO_2 hydrogenation whereas the strong acid sites can promote methanol selectivity and the weak acid sites do not show any considerable activity.

6.3 Paper 3

Time evolution of the CO_2 hydrogenation to fuels over Cu-Zr-SBA-15 catalysts

In **Paper 3,** the time evolution of catalytic CO_2 hydrogenation to methanol and dimethyl ether (DME) has been investigated at 250°C and 33 bars in a closed batch reactor where products accumulate over time. Two types of Cu-Zr-SBA-15 were prepared with the chemical routes described in **Paper 1** and **Paper 2**. TEOS was used as the silica precursor, and Cu nanoparticles were loaded into the Zr-doped SBA-15 matrix with both Inf and EIWI methods in order to compare the trends of different reaction systems. The catalysis results were compared with the thermodynamical equilibrium calculations.

The Cu-Zr-SBA-15 catalyst produced via Inf method has yielded 24 % CO_2 conversion to methanol and DME. This percentage was shown to be the thermodynamically highest theoretical conversion where only DME and methanol are the products. When the EIWI Cu loading method was used, the resulting catalyst was methanol selective. In this case, when DME is not formed, calculations indicate CO as a product suggesting its involvement in DME formation. In both cases, several other molecules (such as methane, methyl formate, and butane) were detected on the catalyst surface by DRIFTS method. However, these molecules were, interestingly, not observed in the final gas mixture which was analyzed by GC-MS. Theoretical calculations showed that in case of formation of any (one or more) of these molecules, no conversion to methanol and DME is possible. Therefore, we concluded that the Cu-Zr-SBA-15 catalysts used in this study were not selective for any of the aforementioned molecules.

DRIFTS measurements also showed increased surface CH_3O^- formation which drops during the reaction for the catalyst prepared via Inf method. EIWI, on the other hand, demonstrated a lower CH_3O^- concentration which stayed stable during the whole reaction where methanol was being formed. Therefore, we inferred that DME was formed by two CH_3O^- molecules reacting with each other, as also mentioned in **Paper 2**. The difference in the surface methoxy concentration is attributed to the strength of the medium acid sites which demonstrate a higher affinity for methoxy as they become stronger.

The time evolution of methanol and DME formation was determined to be a sigmoidal function which indicates a seeding period followed by acceleration and deceleration until an equilibrium value is reached. The importance of seeding was also proven by repeated

reactions using a reacted catalyst isolated from the atmosphere. Methanol formation was determined to be faster than DME since it requires only one methoxy formation, rather than two. Since DME is formed of two methoxy groups, a higher surface methoxy concentration, i.e., a higher seeding duration, is needed.

After the half-time of the reaction (7 days), the conversion increased from 20% to 24% which is a rather small contribution. It indicates that finalizing this reaction at its half-time can cut the energy usage by half but sacrifice only 4% of the total conversion. This is an important finding not only from economical but also from an environmental point.

6.4 Paper 4

Cu and Zr modified SBA-15 as drug carriers

Mesoporous silica has potential use in the biomedical field as a drug carrier. Thus, a modified form of SBA-15 was investigated in **Paper 4** as the means of releasing Chlorhexidine digluconate (CHX), an antibacterial drug.

For this study, SBA-15, Zr-doped SBA-15, and Cu nanoparticle infiltrated Zr-doped SBA-15 were prepared with the chemical routes described in **Paper 1** and investigated as drug carriers. TEOS was used as the silica precursor, and Cu nanoparticles were loaded on the Zr-doped SBA-15 matrix by an infiltration procedure.

The prepared materials were loaded with a 2% CHX solution and yielded a loading percentage of 25-40%. The chemical bonding between the drug and the carrier was confirmed by FTIR via N-H and O-H vibration bands. Cu and Zr contents of the carrier were observed to increase the drug loading amount per unit surface. This was attributed to increased surface active sites and enhanced acidity which improves the attraction of the drug molecules on the carrier walls. The same trend was also shown in released drug percentage which was the highest for SBA-15 (65%) and the lowest for Cu-Zr-SBA-15 (28%), indicating better drug affinity to the carrier when Zr and Cu were added to SBA-15.

Drug release was shown to occur into two stages: a burst release and a slower release. Burst release involves the drug molecules which are weakly held inside the drug carrier whereas the slower release occurs while the drug molecules held on the carrier surface are desorbed. It was observed that for Cu-Zr-SBA-15 and Zr-SBA-15 the second stage is dominant. This

indicates that Zr and Cu improved the drug attachment to the carrier framework and thus, slowed down the drug release which is attributed to enhanced acidity. This effect was observed for Cu more dramatically due to its particle morphology which cause partial blockage in the pores.

Antibacterial properties were investigated against Staphylococcus aureus and Escherichia coli qualitatively and quantitatively by employing agar diffusion. It was found that the release from Cu nanoparticles was too low to cause a considerable boost in the antibacterial properties. The antibacterial inhibition was observed to be in line with the released amounts. The quantitative antibacterial measurements showed that the maximum antibacterial efficiency was achieved between the first 2-6 hours for all the carriers. However, it dropped for Cu-Zr-SBA-15 after a while due to the lower amount of released CHX.

6.5 Paper 5

Tuning the pore size of a mesoporous carrier as means for control of antibiotic release

The study reported in **Paper 4** was complemented with **Paper 5** where SBA-15 was used as a drug carrier and the effect of its pore size on the control of the release of doxycycline hyclate (Doxy), an antibiotic widely used in dental applications, was investigated.

In this study, the pore size of the SBA-15 carrier was tuned between 6.5 and 14.0 nm by changing the synthesis conditions such as temperature and time. The SBA-15 particle morphologychanged from platelet to rods under different synthesis conditions as the pores got wider. Also, specific surface area and microporosity dropped as the pore size got bigger whereas the wall thickness increased.

This study showed that the pore size has a strong effect on the amount of the drug loading on SBA-15. As the pore size increased, the drug loading was observed to increase linearly. On the other hand, the effect of the pore volume as well as the specific surface area on the drug loading amount was found to be minimal.

All the drug release profiles were observed to be diffusion controlled, i.e. burst release. The release rates were found to be inversely proportional to the drug loading per pore volume, i.e. drug concentration. This indicates a slower drug release as the drug concentration in

the pores gets higher. We inferred this behaviour to the drug-drug interactions dominating the release profiles due to weak drug-carrier attachment.

All the drug loading was released for 14 nm pore-sized sample whereas some sample entrapment was observed for 11.5 nm, and 6.5 nm pore sized samples. This was inferred to the changing microporosity.

Finally, the antibacterial activity against Staphylococcus aureus and Escherichia coli was observed to follow the drug release amounts, i.e., pore sizes.

7

CONCLUSIONS AND FUTURE WORK

In this work, SBA-15 and its modified forms as Zr-SBA-15 and Cu-Zr-SBA-15 were prepared and their structural properties as well as their activity in catalysis and drug delivery were investigated. I believe these applications can be taken further in more multi-disciplinary environments. Moreover, the modifications for SBA-15 can be varied to obtain additional/tunable properties in different application areas such as catalysis and drug delivery.

In **Paper 1-3,** SBA-15 and Zr-SBA-15 were synthesized with different pore sizes and morphologies by changing synthesis conditions. For all studied conditions, these materials have shown narrow pore size distributions, hexagonal pore arrangements, and large specific surface areas. In Zr-SBA-15, Zr was incorporated into the SBA-15 framework whereas in Cu-Zr-SBA-15, Cu was incorporated by growing as nanoparticles with a diameter smaller than 10 nm in the pores of Zr-SBA-15. Cu-Zr-SBA-15 was later shown to be catalytically active and can promote CO_2 hydrogenating into DME and methanol. The highest thermodynamically possible CO_2 conversion to DME and methanol, which is 24%, was achieved. Changing the silica source and Cu loading procedure, the catalytic activity and selectivity between DME and methanol was modified. The time evolution of the CO_2 hydrogenation have shown that methanol formation is faster than DME. High methanol selectivity requires sufficient surface H affinity, whereas high DME selectivity requires high surface methoxy concentration. It was concluded that methoxy can join the formation of DME without going through hydrogenation into a methanol molecule. On

the other hand, the equilibrium point of the conversion was achieved only after 14 days. The slow evolution is due to two reasons: 1) a batch reactor is used for this reactor where each molecule of a product works against the CO_2 conversion, and 2) pressure was as low as 33 bars.

As the future work, I suggest a full study employing a flow type reactor which can improve the reactant-catalyst contact and help to remove the products from the catalyst environment simultaneously. On the other hand, under 50 bars it was shown to improve the total CO_2 conversion. A full study for the conversion and selectivity at 50 bars or higher should be conducted. Our findings can guide all this suggested conversion improvement efforts. Synthesis-wise, Cu-Zr-SBA-15 systems should further be investigated by using different elements such as Ni or Co. Also as the dopant, Zn or Al can be used in different combinations. As the next step, the industrialization process should take place where the studied catalyst powders can be brought to disc forms and appropriate catalytic systems possibly composed of recycling and additional columns installed in series to the reactor for separation of fuels such as methanol and DME.

A Cu-Zr-SBA-15 material prepared within this thesis work was shown in **Paper 4** to respond well as a drug carrier. Cu and Zr components were shown to slow down the drug release and improve the drug loading. Moreover, when Cu was prepared as nanoparticles, the resulting ion release was different from a simple ion doping. **Paper 5** have demonstrated that changing the pore size of SBA-15 can affect the drug loading and release amount directly. To achieve a final drug delivery device in the future, the Cu-Zr-SBA-15 powder should further be treated since dental procedures require well mixing of the drug loaded SBA-15 particles with the dental composite is crucial. Also, in vivo pharmacological tests and toxicity measurements are important for future applications.

References

(1) Rouquerol, J.; Avnir, D.; Fairbridge, C. W.; Everett, D. H.; Haynes, J. M.; Pernicone, N.; Ramsay, J. D. F.; Sing, K. S. W.; Unger, K. K. Recommendations for the Characterization of Porous Solids (Technical Report). *Pure Appl. Chem.* **1994**, *66* (8), 1739–1758.

(2) Sing, K. S. W. Reporting Physisorption Data for Gas/solid Systems with Special Reference to the Determination of Surface Area and Porosity (Provisional). *Pure Appl. Chem.* **1982**, *54* (11), 2201–2218.

(3) Beck, J. S.; Vartuli, J. C.; Roth, W. J.; Leonowicz, M. E.; Kresge, C. T.; Schmitt, K. D.; Chu, C. T. W.; Olson, D. H.; Sheppard, E. W. A New Family of Mesoporous Molecular Sieves Prepared with Liquid Crystal Templates. *J. Am. Chem. Soc.* **1992**, *114* (27), 10834–10843.

(4) Kresge, C. T. Leonowicz, M. E.Roth, W. J.Vartuli, J.Beck, J. S. C. Ordered Mesoporous Molecular Sieves Synthesized by a Liquid-Crystal Template Mechanism. *Nature* **1992**, *359* (6397), 710–712.

(5) Wang, S. Ordered Mesoporous Materials for Drug Delivery. *Microporous Mesoporous Mater.* **2009**, *117* (1–2), 1–9.

(6) Park, S.-Y.; Pendleton, P. Mesoporous Silica SBA-15 for Natural Antimicrobial Delivery. *Powder Technol.* **2012**, *223*, 77–82.

(7) Mamaeva, V.; Sahlgren, C.; Lindén, M. Mesoporous Silica Nanoparticles in Medicine--Recent Advances. *Adv. Drug Deliv. Rev.* **2013**, *65* (5), 689–702.

(8) Izquierdo-Barba, I.; Martinez, A.; Doadrio, A. L.; Pérez-Pariente, J.; Vallet-Regí, M. Release Evaluation of Drugs from Ordered Three-Dimensional Silica Structures. *Eur. J. Pharm. Sci.* **2005**, *26* (5), 365–373.

(9) Eggenhuisen, T. M.; Zečević, J.; Talsma, H.; De Jong, K. P.; De Jongh, P. E. Quantitative Assessment of Pore Blockage in Supported Catalysts: Comparing Differential Scanning Calorimetry and Physisorption. *J. Phys. Chem. C* **2012**, *116* (13), 7480–7490.

(10) Moritz, M.; Geszke-Moritz, M. Mesoporous Materials as Multifunctional Tools in Biosciences: Principles and Applications. *Mater. Sci. Eng. C* **2014**, *49*, 114–151.

(11) Alothman, Z. A Review: Fundamental Aspects of Silicate Mesoporous Materials. *Materials (Basel).* **2012**, *5* (12), 2874–2902.

(12) Zhao, D.; Feng, J.; Huo, Q.; Melosh, N.; Fredrickson, G. H.; Chmelka, B. F.; Stucky, G. D. Triblock Copolymer Syntheses of Mesoporous Silica with Periodic 50 to 300 Angstrom Pores. *Science (80-.).* **1998**, *279* (5350), 548–552.

(13) Mihai, G. D.; Meynen, V.; Mertens, M.; Bilba, N.; Cool, P.; Vansant, E. F. ZnO Nanoparticles Supported on Mesoporous MCM-41 and SBA-15: A Comparative Physicochemical and Photocatalytic Study. *J. Mater. Sci.* **2010**, *45* (21), 5786–5794.

(14) Hartmann, M.; Vinu, A. Mechanical Stability and Porosity Analysis of Large-Pore SBA-15 Mesoporous Molecular Sieves by Mercury Porosimetry and Organics Adsorption. *Langmuir* **2002**, *18* (21), 8010–8016.

(15) Johansson, E. M.; Ballem, M. A.; Cordoba, J. M.; Oden, M. Rapid Synthesis of SBA-15 Rods with Variable Lengths, Widths, and Tunable Large Pores. *Langmuir* **2011**, *27* (8), 4994–4999.

(16) Johansson, E. M.; Córdoba, J. M.; Odén, M. The Effects on Pore Size and Particle Morphology of Heptane Additions to the Synthesis of Mesoporous Silica SBA-15. *Microporous Mesoporous Mater.* **2010**, *133* (1–3), 66–74.

(17) Yeh, Y.-Q.; Lin, H.-P.; Tang, C.-Y.; Mou, C.-Y. Mesoporous Silica SBA-15 Sheet with Perpendicular Nanochannels. *J. Colloid Interface Sci.* **2011**, *362* (2), 354–366.

(18) Zhao, D.; Sun, J.; Li, Q.; Stucky, G. D. Morphological Control of Highly Ordered Mesoporous Silica SBA-15. *Chem. Mater.* **2000**, *12* (2), 275–279.

(19) Cao, L.; Kruk, M. Synthesis of Large-Pore SBA-15 Silica from Tetramethyl Orthosilicate Using Triisopropylbenzene as Micelle Expander. *Colloids Surfaces A Physicochem. Eng. Asp.* **2010**, *357* (1–3), 91–96.

(20) Fulvio, P. F.; Pikus, S.; Jaroniec, M. Short-Time Synthesis of SBA-15 Using Various Silica Sources. *J. Colloid Interface Sci.* **2005**, *287* (2), 717–720.

(21) Björk, E. M.; Söderlind, F.; Odén, M. Tuning the Shape of Mesoporous Silica Particles by Alterations in Parameter Space: From Rods to Platelets. *Langmuir* **2013**, *29* (44), 13551–13561.

(22) Alfredsson, V.; Wennerström, H. The Dynamic Association Processes Leading from a Silica Precursor to a Mesoporous SBA-15 Material. *Acc. Chem. Res.* **2015**, *48* (7), 1891–1900.

(23) Nagarajan, R. Amphiphilic Surfactants and Amphiphilic Polymers: Principles of Molecular Assembly. In *ACS Symposium Series*; 2011; Vol. 1070, pp 1–22.

(24) Gobin, O. C. SBA-15 Materials - Synthesis, Diffusion and Sorption Properties, 2006.

(25) Teixeira, C. V; Amenitsch, H.; Linton, P.; Lindén, M.; Alfredsson, V. The Role Played by Salts in the Formation of SBA-15, an in Situ Small-Angle X-Ray Scattering/Diffraction Study. *Langmuir* **2011**, *27* (11), 7121–7131.

(26) Björk, E. M.; Mäkie, P.; Rogström, L.; Atakan, A.; Schell, N.; Odén, M. Formation of Block-Copolymer-Templated Mesoporous Silica. *J. Colloid Interface Sci.* **2018**, *521*, 183–189.

(27) Denkova, A. G.; Mendes, E.; Coppens, M.-O. Effects of Salts and Ethanol on the Population and Morphology of Triblock Copolymer Micelles in Solution. *J. Phys. Chem. B* **2008**, *112* (3), 793–801.

(28) Linton, P.; Wennerström, H.; Alfredsson, V. Controlling Particle Morphology and Size in the Synthesis of Mesoporous SBA-15 Materials. *Phys. Chem. Chem. Phys.* **2010**, *12* (15), 3852–3858.

(29) Jana, S. K.; Mochizuki, A.; Namba, S. Progress in Pore-Size Control of Mesoporous MCM-41 Molecular Sieve Using Surfactant Having Different Alkyl Chain Lengths and Various Organic Auxiliary Chemicals. *Catal. Surv. from Asia* **2004**, *8* (1), 1–13.

(30) Nguyen, T. P. B.; Lee, J.-W.; Shim, W. G.; Moon, H. Synthesis of Functionalized SBA-15 with Ordered Large Pore Size and Its Adsorption Properties of BSA. *Microporous Mesoporous Mater.* **2008**, *110* (2–3), 560–569.

(31) Meynen, V.; Cool, P.; Vansant, E. F. Verified Syntheses of Mesoporous Materials. *Microporous Mesoporous Mater.* **2009**, *125* (3), 170–223.

(32) Kruk, M. Access to Ultralarge-Pore Ordered Mesoporous Materials through Selection of Surfactant/Swelling-Agent Micellar Templates. *Acc. Chem. Res.* **2012**, *45* (10), 1678–1687.

(33) Li, Q.; Wu, Z.; Feng, D.; Tu, B.; Zhao, D. Hydrothermal Stability of Mesostructured Cellular Silica Foams. *J. Phys. Chem. C* **2010**, *114* (11), 5012–5019.

(34) Wan, Y.; Shi, Y.; Zhao, D. Designed Synthesis of Mesoporous Solids via Nonionic-Surfactant-Templating Approach. *Chem. Commun.* **2007**, No. 9, 897–926.

(35) Jin, D.; Zhu, B.; Hou, Z.; Fei, J.; Lou, H.; Zheng, X. Dimethyl Ether Synthesis via Methanol and Syngas over Rare Earth Metals Modified Zeolite Y and Dual Cu–Mn–Zn Catalysts. *Fuel* **2007**, *86* (17–18), 2707–2713.

(36) MAO, D.; YANG, W.; XIA, J.; ZHANG, B.; SONG, Q.; CHEN, Q. Highly Effective Hybrid Catalyst for the Direct Synthesis of Dimethyl Ether from Syngas with Magnesium Oxide-Modified HZSM-5 as a Dehydration Component. *J. Catal.* **2005**, *230* (1), 140–149.

(37) Liu, X.; Bai, S.; Zhuang, H.; Yan, Z. Preparation of Cu/ZrO2 Catalysts for Methanol Synthesis from CO2/H2. *Front. Chem. Sci. Eng.* **2012**, *6* (1), 47–52.

(38) Zhong, X.; Barbier, J.; Duprez, D.; Zhang, H.; Royer, S. Modulating the Copper Oxide Morphology and Accessibility by Using Micro-/mesoporous SBA-15 Structures as Host Support: Effect on the Activity for the CWPO of Phenol Reaction. *Appl. Catal. B Environ.* **2012**, *121–122*, 123–134.

(39) Anu Prathap, M. U.; Kaur, B.; Srivastava, R. Direct Synthesis of Metal Oxide Incorporated Mesoporous SBA-15, and Their Applications in Non-Enzymatic Sensing of Glucose. *J Colloid Interface Sci* **2012**, *381* (1), 143–151.

(40) Usami, Y.; Hongo, T.; Yamazaki, A. Thermal Stability and Behavior of Platelet-Shaped SBA-15 Containing Zr. *J. Porous Mater.* **2011**, *19* (5), 897–902.

(41) Chandra Mouli, K.; Mohanty, S.; Hu, Y.; Dalai, A.; Adjaye, J. Effect of Hetero Atom on Dispersion of NiMo Phase on M-SBA-15 (M=Zr, Ti, Ti-Zr). *Catal. Today* **2013**, *207*, 133–144.

(42) Reyes-Carmona, Á.; Arango-Díaz, A.; Moretti, E.; Talon, A.; Storaro, L.; Lenarda, M.; Jiménez-López, A.; Rodríguez-Castellón, E. CuO/CeO2 Supported on Zr Doped SBA-15 as Catalysts for Preferential CO Oxidation (CO-PROX). *J. Power Sources* **2011**, *196* (9), 4382–4387.

(43) Zhang, H.; Tang, C.; Lv, Y.; Sun, C.; Gao, F.; Dong, L.; Chen, Y. Synthesis, Characterization, and Catalytic Performance of Copper-Containing SBA-15 in the Phenol Hydroxylation. *J Colloid Interface Sci* **2012**, *380* (1), 16–24.

(44) Aghayan, H.; Mahjoub, A. R.; Khanchi, A. R. Samarium and Dysprosium Removal Using 11-Molybdo-Vanadophosphoric Acid Supported on Zr Modified Mesoporous Silica SBA-15. *Chem.*

Eng. J. **2013**, *225* (0), 509–519.

(45) Sawant, D. P.; Vinu, A.; Jacob, N. E.; Lefebvre, F.; Halligudi, S. B. Formation of Nanosized Zirconia-Supported 12-Tungstophosphoric Acid in Mesoporous Silica SBA-15: A Stable and Versatile Solid Acid Catalyst for Benzylation of Phenol. *J. Catal.* **2005**, *235* (2), 341–352.

(46) García-Trenco, A.; Martínez, A. A Simple and Efficient Approach to Confine Cu/ZnO Methanol Synthesis Catalysts in the Ordered Mesoporous SBA-15 Silica. *Catal. Today* **2013**, *215* (0), 152–161.

(47) Ajaikumar, S.; Golets, M.; Larsson, W.; Shchukarev, a.; Kordas, K.; Leino, a.-R.; Mikkola, J.-P. Effective Dispersion of Au and Au–M (M=Co, Ni, Cu and Zn) Bimetallic Nanoparticles over TiO2 Grafted SBA-15: Their Catalytic Activity on Dehydroisomerization of α-Pinene. *Microporous Mesoporous Mater.* **2013**, *173*, 99–111.

(48) Prieto, G.; Zečević, J.; Friedrich, H.; de Jong, K. P.; de Jongh, P. E. Towards Stable Catalysts by Controlling Collective Properties of Supported Metal Nanoparticles. *Nat. Mater.* **2013**, *12* (1), 34–39.

(49) Tang, Y.; Zong, E.; Wan, H.; Xu, Z.; Zheng, S.; Zhu, D. Zirconia Functionalized SBA-15 as Effective Adsorbent for Phosphate Removal. *Microporous Mesoporous Mater.* **2012**, *155*, 192–200.

(50) Katryniok, B.; Paul, S.; Capron, M.; Royer, S.; Lancelot, C.; Jalowiecki-Duhamel, L.; Bellière-Baca, V.; Rey, P.; Dumeignil, F. Synthesis and Characterization of Zirconia-Grafted SBA-15 Nanocomposites. *J. Mater. Chem.* **2011**, *21* (22), 8159.

(51) Subbaramaiah, V.; Srivastava, V. C.; Mall, I. D. Catalytic Activity of Cu/SBA-15 for Peroxidation of Pyridine Bearing Wastewater at Atmospheric Condition. *AIChE J.* **2013**, *59* (7), 2577–2586.

(52) Tsoncheva, T.; Linden, M.; Areva, S.; Minchev, C. Copper Oxide Modified Large Pore Ordered Mesoporous Silicas for Ethyl Acetate Combustion. *Catal. Commun.* **2006**, *7* (6), 357–361.

(53) Dixit, M.; Mishra, M.; Joshi, P. a.; Shah, D. O. Study on the Catalytic Properties of Silica Supported Copper Catalysts. *Procedia Eng.* **2013**, *51* (NUiCONE 2012), 467–472.

(54) Salvador, M. A.; Canales-Vázquez, J.; Ferreira, P.; Figueiredo, F. M. Characterization of Mesoporous Zirconium and Cerium Oxides by Transmission Electron Microscopy. *Microsc. Microanal.* **2012**, *18* (Supplement S5), 81–82.

(55) Gutiérrez, O. Y.; Romero, K. A.; Fuentes, G. A.; Klimova, T. New NiMo Catalysts Supported on ZrO2-Modified SBA-15 Materials for 4,6-Dimethyldibenzothiophene Hydrodesulfurization. In *Scientific Bases for the Preparation of Heterogeneous Catalysts Proceedings of the 9th International Symposium*; E.M. Gaigneaux D.E. De Vos, S. Hermans, P.A. Jacobs, J.A. Martens and P. Ruiz BT - Studies in Surface Science and Catalysis, M. D., Ed.; Elsevier, 2006; Vol. Volume 162, pp 355–362.

(56) Florek-Milewska, J.; Decyk, P.; Ziolek, M. Catalytic Properties of Cu/SBA-3 in Oxidative Dehydrogenation of methanol—The Effect of the Support Composition. *Appl. Catal. A Gen.* **2011**, *393* (1–2), 215–224.

(57) Ungureanu, A.; Dragoi, B.; Chirieac, A.; Ciotonea, C.; Royer, S.; Duprez, D.; Mamede, A. S.;

Dumitriu, E. Composition-Dependent Morphostructural Properties of Ni-Cu Oxide Nanoparticles Confined within the Channels of Ordered Mesoporous SBA-15 Silica. *ACS Appl. Mater. Interfaces* **2013**, *5* (8), 3010–3025.

(58) Tsoncheva, T.; Dal Santo, V.; Gallo, A.; Scotti, N.; Dimitrov, M.; Kovacheva, D. Structure and Catalytic Activity of Hosted in Mesoporous Silicas Copper Species: Effect of Preparation Procedure and Support Pore Topology. *Appl. Catal. A Gen.* **2011**, *406* (1–2), 13–21.

(59) Garcia-Cuello, V. S.; Giraldo, L.; Moreno-Piraján, J. C. Oxidation of Carbon Monoxide Over SBA-15-Confined Copper, Palladium and Iridium Nanocatalysts. *Catal. Letters* **2011**, *141* (11), 1659–1669.

(60) Escalera, E.; Ballem, M. A.; Córdoba, J. M.; Antti, M.-L.; Odén, M. Synthesis of Homogeneously Dispersed Cobalt Nanoparticles in the Pores of Functionalized SBA-15 Silica. *Powder Technol.* **2012**, *221*, 359–364.

(61) Zha, F.; Ding, J.; Chang, Y. Cu–Zn–Al Oxide Cores Packed by Metal-Doped Amorphous Silica–Alumina Membrane for Catalyzing the Hydrogenation of Carbon Dioxide to Dimethyl Ether. *Ind. Eng. …* **2011**, 345–352.

(62) Alonso, A.; Moral-Vico, J.; Abo Markeb, A.; Busquets-Fité, M.; Komilis, D.; Puntes, V.; Sánchez, A.; Font, X. Critical Review of Existing Nanomaterial Adsorbents to Capture Carbon Dioxide and Methane. *Sci. Total Environ.* **2017**, *595*, 51–62.

(63) Song, H.; Rioux, R.; Hoefelmeyer, J.; Komor, R.; Niesz …, K. Hydrothermal Growth of Mesoporous SBA-15 Silica in the \nPresence of PVP-Stabilized Pt Nanoparticles: Synthesis, \nCharacterization, and Catalytic Properties \n. *J. Am. Chem. Soc* **2006**, No. 13, 3027–3037.

(64) Wang, N.; Yu, X.; Shen, K.; Chu, W.; Qian, W. Synthesis, Characterization and Catalytic Performance of MgO-Coated Ni/SBA-15 Catalysts for Methane Dry Reforming to Syngas and Hydrogen. *Int. J. Hydrogen Energy* **2013**, *38* (23), 9718–9731.

(65) Slowing, I. I.; Trewyn, B. G.; Giri, S.; Lin, V. S.-Y. Mesoporous Silica Nanoparticles for Drug Delivery and Biosensing Applications. *Adv. Funct. Mater.* **2007**, *17* (8), 1225–1236.

(66) Biswas, P.; Narayanasarma, P.; Kotikalapudi, C. M.; Dalai, A. K.; Adjaye, J. Characterization and Activity of ZrO2Doped SBA-15 Supported NiMo Catalysts for HDS and HDN of Bitumen Derived Heavy Gas Oil. *Ind. Eng. Chem. Res.* **2011**, *50* (13), 7882–7895.

(67) Wei, L.; Hu, N.; Zhang, Y. Synthesis of Polymer—Mesoporous Silica Nanocomposites. *Materials (Basel).* **2010**, *3* (7), 4066–4079.

(68) Wang, W.; Wang, S.; Ma, X.; Gong, J. Recent Advances in Catalytic Hydrogenation of Carbon Dioxide. *Chem Soc Rev* **2011**, *40* (7), 3703–3727.

(69) Van Speybroeck, M.; Barillaro, V.; Thi, T. Do; Mellaerts, R.; Martens, J.; Van Humbeeck, J.; Vermant, J.; Annaert, P.; Van den Mooter, G.; Augustijns, P. Ordered Mesoporous Silica Material SBA-15: A Broad-Spectrum Formulation Platform for Poorly Soluble Drugs. *J. Pharm. Sci.* **2009**, *98* (8), 2648–2658.

(70) Śliwa, M.; Samson, K.; Ruggiero–Mikołajczyk, M.; Żelazny, a.; Grabowski, R. Influence of Montmorillonite K10 Modification with Tungstophosphoric Acid on Hybrid Catalyst Activity in

Direct Dimethyl Ether Synthesis from Syngas. *Catal. Letters* **2014**, *144* (11), 1884–1893.

(71) Tu, C.-H.; Wang, A.-Q.; Zheng, M.-Y.; Wang, X.-D.; Zhang, T. Factors Influencing the Catalytic Activity of SBA-15-Supported Copper Nanoparticles in CO Oxidation. *Appl. Catal. A Gen.* **2006**, *297* (1), 40–47.

(72) Selvaraj, M.; Kawi, S. An Optimal Direct Synthesis of CrSBA-15 Mesoporous Materials with Enhanced Hydrothermal Stability. *Chem. Mater.* **2007**, *19* (3), 509–519.

(73) Lin, D.-H.; Jiang, Y.-X.; Wang, Y.; Sun, S.-G. Silver Nanoparticles Confined in SBA-15 Mesoporous Silica and the Application as a Sensor for Detecting Hydrogen Peroxide. *J. Nanomater.* **2008**, *2008*, 1–10.

(74) Semelsberger, T. A.; Borup, R. L.; Greene, H. L. Dimethyl Ether (DME) as an Alternative Fuel. *J. Power Sources* **2006**, *156* (2), 497–511.

(75) Olah, G. a. Beyond Oil and Gas: The Methanol Economy. *Angew. Chem. Int. Ed. Engl.* **2005**, *44* (18), 2636–2639.

(76) Olah, G. A.; Goeppert, A.; Prakash, G. K. S. Chemical Recycling of Carbon Dioxide to Methanol and Dimethyl Ether: From Greenhouse Gas to Renewable, Environmentally Carbon Neutral Fuels and Synthetic Hydrocarbons. *J. Org. Chem.* **2008**, *74* (2), 487–498.

(77) Blasing, T. J. Recent Greenhouse Gas Concentrations. **2009**, No. August 2016, 1–5.

(78) Cox, P.; Jones, C. CLIMATE CHANGE: Illuminating the Modern Dance of Climate and CO2. *Science (80-.).* **2008**, *321* (5896), 1642–1644.

(79) Royer, D. L.; Berner, R. A.; Park, J. Climate Sensitivity Constrained by CO2 Concentrations over the Past 420 Million Years. *Nature* **2007**, *446* (7135), 530–532.

(80) Takht Ravanchi, M.; Sahebdelfar, S. Carbon Dioxide Capture and Utilization in Petrochemical Industry: Potentials and Challenges. *Appl. Petrochemical Res.* **2014**, *4* (1), 63–77.

(81) Chang, K.; Wang, T.; Chen, J. G. Hydrogenation of CO2 to Methanol over CuCeTiOx Catalysts. *Appl. Catal. B Environ.* **2017**, *206*, 704–711.

(82) Sankaranarayanan, S.; Srinivasan, K. Carbon Dioxide – A Potential Raw Material for the Production of Fuel , Fuel Additives and Bio-Derived Chemicals. **2012**, *51*, 1252–1262.

(83) Ahouari, H.; Soualah, A.; Le Valant, A.; Pinard, L.; Magnoux, P.; Pouilloux, Y. Methanol Synthesis from CO2 Hydrogenation over Copper Based Catalysts. *React. Kinet. Mech. Catal.* **2013**, *110* (1), 131–145.

(84) Arena, F.; Barbera, K.; Italiano, G.; Bonura, G.; Spadaro, L.; Frusteri, F. Synthesis, Characterization and Activity Pattern of Cu–ZnO/ZrO2 Catalysts in the Hydrogenation of Carbon Dioxide to Methanol. *J. Catal.* **2007**, *249* (2), 185–194.

(85) Pontzen, F.; Liebner, W.; Gronemann, V.; Rothaemel, M.; Ahlers, B. CO2-Based Methanol and DME – Efficient Technologies for Industrial Scale Production. *Catal. Today* **2011**, *171* (1), 242–250.

(86) Gao, P.; Li, F.; Xiao, F.; Zhao, N.; Sun, N.; Wei, W.; Zhong, L.; Sun, Y. Preparation and Activity

of Cu/Zn/Al/Zr Catalysts via Hydrotalcite-Containing Precursors for Methanol Synthesis from CO2 Hydrogenation. *Catal. Sci. Technol.* **2012**, *2* (7), 1447.

(87) Styring, P.; Armstrong, K. Catalytic Carbon Dioxide Conversions to Value-Added Chemicals. *Chimica Oggi*. 2011, pp 34–37.

(88) Liang, X.-L.; Dong, X.; Lin, G.-D.; Zhang, H.-B. Carbon Nanotube-Supported Pd–ZnO Catalyst for Hydrogenation of CO2 to Methanol. *Appl. Catal. B Environ.* **2009**, *88* (3–4), 315–322.

(89) Pérez-Fortes, M.; Schöneberger, J. C.; Boulamanti, A.; Tzimas, E. Methanol Synthesis Using Captured CO2 as Raw Material: Techno-Economic and Environmental Assessment. *Appl. Energy* **2016**, *161*, 718–732.

(90) Huang, C.; Chen, S.; Fei, X.; Liu, D.; Zhang, Y. Catalytic Hydrogenation of CO2 to Methanol: Study of Synergistic Effect on Adsorption Properties of CO2 and H2 in CuO/ZnO/ZrO2 System. *Catalysts* **2015**, *5* (4), 1846–1861.

(91) Saeidi, S.; Amin, N. A. S.; Rahimpour, M. R. Hydrogenation of CO2 to Value-Added products—A Review and Potential Future Developments. *J. CO2 Util.* **2014**, *5*, 66–81.

(92) Jadhav, S. G.; Vaidya, P. D.; Bhanage, B. M.; Joshi, J. B. Catalytic Carbon Dioxide Hydrogenation to Methanol: A Review of Recent Studies. *Chem. Eng. Res. Des.* **2014**, *92* (11), 2557–2567.

(93) Ma, J.; Sun, N.; Zhang, X.; Zhao, N.; Xiao, F.; Wei, W.; Sun, Y. A Short Review of Catalysis for CO2 Conversion. *Catal. Today* **2009**, *148* (3–4), 221–231.

(94) Sakakura, T.; Choi, J.-C.; Yasuda, H. Transformation of Carbon Dioxide. *Chem. Rev.* **2007**, *107* (6), 2365–2387.

(95) Suib, S. L.; Homs, N.; Toyir, J.; de la Piscina, P. R. *New and Future Developments in Catalysis*; Elsevier, 2013.

(96) Arakawa, H. *Advances in Chemical Conversions for Mitigating Carbon Dioxide, Proceedings of the Fourth International Conference on Carbon Dioxide Utilization*; Studies in Surface Science and Catalysis; Elsevier, 1998; Vol. 114.

(97) Skrzypek, J.; Lachowska, M.; Grzesik, M.; Słoczyński, J.; Nowak, P. Thermodynamics and Kinetics of Low Pressure Methanol Synthesis. *Chem. Eng. J. Biochem. Eng. J.* **1995**, *58* (2), 101–108.

(98) IUPAC Compendium of Chemical Terminology. **2009**, *2291* (Recommendations 1990), 2293.

(99) Deutschmann, O.; Knözinger, H.; Kochloefl, K.; Turek, T. Heterogeneous Catalysis and Solid Catalysts. In *Ullmann's Encyclopedia of Industrial Chemistry*; Wiley-VCH Verlag GmbH & Co. KGaA, 2000.

(100) Huff, C.; Sanford, M. Catalytic CO2 Hydrogenation to Formate by a Ruthenium Pincer Complex. *ACS Catal.* **2013**, 2412–2416.

(101) Kasaie, M.; Sohrabi, M. Kinetic Study on Methanol Dehydration to Dimethyl Ether Applying Clinoptilolite Zeolite as the Reaction Catalyst. *J. Mex. Chem. Soc.* **2009**, *53* (4), 233–238.

(102) Lee, S. Methanol Synthesis from Syngas. In *Handbook of Alternative Fuel Technologies*; CRC

Press, 2007; pp 297–321.

(103) Olah, G. A.; Molnár, Á. *Hydrocarbon Chemistry*; John Wiley & Sons, Inc.: Hoboken, NJ, USA, 2003.

(104) Olah, G. A.; Prakash, G. K. S. Conversion of Carbon Dioxide to Dimethyl Ether Using Bi-Reforming of Methane or Natural Gas, 2012.

(105) Tidona, B.; Koppold, C.; Bansode, A.; Urakawa, A.; Rudolf Von Rohr, P. CO2 Hydrogenation to Methanol at Pressures up to 950 Bar. *J. Supercrit. Fluids* **2013**, *78*, 70–77.

(106) Rozovskii, A.; Lin, G. Fundamentals of Methanol Synthesis and Decomposition. *Top. Catal.* **2003**, *22* (3–4), 137–150.

(107) McGrath, K. M.; Prakash, G. K. S.; Olah, G. A. Direct Methanol Fuel Cells. *J. Ind. Eng. Chem.* **2004**, *10* (7), 1063–1080.

(108) Mittasch, A.; Pier, M. Synthetic Manufacture of Methanol, January 12, 1926.

(109) Klier, K. Methanol Synthesis. *Adv. Catal.* **1982**, *31*, 243–313.

(110) van Bennekom, J. G.; Venderbosch, R. H.; Winkelman, J. G. M.; Wilbers, E.; Assink, D.; Lemmens, K. P. J.; Heeres, H. J. Methanol Synthesis beyond Chemical Equilibrium. *Chem. Eng. Sci.* **2013**, *87*, 204–208.

(111) Kandemir, T.; Friedrich, M.; Parker, S. F.; Studt, F.; Lennon, D.; Schlögl, R.; Behrens, M. Different Routes to Methanol: Inelastic Neutron Scattering Spectroscopy of Adsorbates on Supported Copper Catalysts. *Phys. Chem. Chem. Phys.* **2016**, No. 4, 17253–17258.

(112) Zhao, Y.-F.; Yang, Y.; Mims, C.; Peden, C. H. F.; Li, J.; Mei, D. Insight into Methanol Synthesis from CO2 Hydrogenation on Cu(111): Complex Reaction Network and the Effects of H2O. *J. Catal.* **2011**, *281* (2), 199–211.

(113) Hu, Z.-M.; Takahashi, K.; Nakatsuji, H. Mechanism of the Hydrogenation of CO2 to Methanol on a Cu(100) Surface: Dipped Adcluster Model Study. *Surf. Sci.* **1999**, *442* (1), 90–106.

(114) Grabow, L. C.; Mavrikakis, M. Mechanism of Methanol Synthesis on Cu through CO2and CO Hydrogenation. *ACS Catal.* **2011**, *1* (4), 365–384.

(115) Yang, Y.; White, M. G.; Liu, P. A Theoretical Study of Methanol Synthesis from CO2 Hydrogenation on Metal-Doped Cu(111) Surfaces. *J Phys Chem A* **2011**.

(116) Reubroycharoen, P.; Yamagami, T.; Vitidsant, T.; Yoneyama, Y.; Ito, M.; Tsubaki, N. Continuous Low-Temperature Methanol Synthesis from Syngas Using Alcohol Promoters. *Energy & Fuels* **2003**, *17* (4), 817–821.

(117) Gokhale, A. A.; Dumesic, J. A.; Mavrikakis, M. Article On the Mechanism of Low-Temperature Water Gas Shift Reaction on Copper On the Mechanism of Low-Temperature Water Gas Shift Reaction on Copper. *J. Am. Chem. Soc.* **2008**, *130* (33), 1402–1414.

(118) Loyd J. Burcham, †; Laura E. Briand, ‡ and; Israel E. Wachs*, §. Quantification of Active Sites for the Determination of Methanol Oxidation Turn-over Frequencies Using Methanol Chemisorption and in Situ Infrared Techniques. 1. Supported Metal Oxide Catalysts. *Langmuir*

2001, *17*(20), 6164–6174.

(119) Gao, P.; Xie, R.; Wang, H.; Zhong, L.; Xia, L.; Zhang, Z.; Wei, W.; Sun, Y. Cu / Zn / Al / Zr Catalysts via Phase-Pure Hydrotalcite-like Compounds for Methanol Synthesis from Carbon Dioxide. *Biochem. Pharmacol.* **2015**.

(120) an, X.; Zuo, Y.; Zhang, Q.; Wang, J. Methanol Synthesis from CO2 Hydrogenation with a Cu/Zn/Al/Zr Fibrous Catalyst. *Chinese J. Chem. Eng.* **2009**, *17*(1), 88–94.

(121) Pinto, A. Methanol Production. US 4455394 A, 1984.

(122) Shulenberger, A. M.; Jonsson, F. R.; Ingolfsson, O.; Tran, K. C. Process for Producing Liquid Fuel from Carbon Dioxide and Water. US 8198338 B2, 2012.

(123) Matsushita, T.; Haganuma, T.; Fujita, D. Process for Producing Methanol. US 20130237618 A1, 2013.

(124) da Silva, R. J.; Pimentel, A. F.; Monteiro, R. S.; Mota, C. J. A. Synthesis of Methanol and Dimethyl Ether from the CO2 Hydrogenation over Cu·ZnO Supported on Al2O3 and Nb2O5. *J. CO2 Util.* **2016**, No. 2015, 1–6.

(125) Raudaskoski, R.; Niemela, M. V.; Keiski, R. L. The Effect of Ageing Time on Co-Precipitated Cu/ZnO/ZrO2 Catalysts Used in Methanol Synthesis from CO2 and H2. *Top. Catal.* **2007**, *45*(1–4), 57–60.

(126) Guo, X.; Mao, D.; Wang, S.; Wu, G.; Lu, G. Combustion Synthesis of CuO-ZnO-ZrO2 Catalysts for the Hydrogenation of Carbon Dioxide to Methanol. *Catal. Commun.* **2009**, *10*(13), 1661–1664.

(127) Zhang, Y.; Fei, J.; Yu, Y.; Zheng, X. Methanol Synthesis from CO2 Hydrogenation over Cu Based Catalyst Supported on Zirconia Modified γ-Al2O3. *Energy Convers. Manag.* **2006**, *47*(18–19), 3360–3367.

(128) Witoon, T.; Numpilai, T.; Phongamwong, T.; Donphai, W.; Boonyuen, C.; Warakulwit, C.; Chareonpanich, M.; Limtrakul, J. Enhanced Activity, Selectivity and Stability of a CuO-ZnO-ZrO 2 Catalyst by Adding Graphene Oxide for CO 2 Hydrogenation to Methanol. *Chem. Eng. J.* **2018**, *334*(November 2017), 1781–1791.

(129) Lei, Z.; Zou, Z.; Dai, C.; Li, Q.; Chen, B. Synthesis of Dimethyl Ether (DME) by Catalytic Distillation. *Chem. Eng. Sci.* **2011**, *66*(14), 3195–3203.

(130) Hosseininejad, S.; Afacan, a.; Hayes, R. E. Catalytic and Kinetic Study of Methanol Dehydration to Dimethyl Ether. *Chem. Eng. Res. Des.* **2012**, *90*(6), 825–833.

(131) Frusteri, F.; Cordaro, M.; Cannilla, C.; Bonura, G. Multifunctionality of Cu–ZnO–ZrO2/H-ZSM5 Catalysts for the One-Step CO2-to-DME Hydrogenation Reaction. *Appl. Catal. B Environ.* **2015**, *162*, 57–65.

(132) Rownaghi, A. A.; Rezaei, F.; Stante, M.; Hedlund, J. Selective Dehydration of Methanol to Dimethyl Ether on ZSM-5 Nanocrystals. *Appl. Catal. B Environ.* **2012**, *119–120*(0), 56–61.

(133) Asthana, S.; Samanta, C.; Bhaumik, A.; Banerjee, B.; Voolapalli, R. K.; Saha, B. Direct Synthesis of Dimethyl Ether from Syngas over Cu-Based Catalysts: Enhanced Selectivity in the Presence of

MgO. *J. Catal.* **2016**, *334*, 89–101.

(134) Lei, Z.; Zou, Z.; Dai, C.; Li, Q.; Chen, B. Synthesis of Dimethyl Ether (DME) by Catalytic Distillation. *Chem. Eng. Sci.* **2011**, *66* (14), 3195–3203.

(135) Liu, R.; Qin, Z.; Ji, H.; Su, T. Synthesis of Dimethyl Ether from CO 2 and H 2 Using a Cu–Fe–Zr/HZSM-5 Catalyst System. *Ind. Eng. Chem. Res.* **2013**, *52* (47), 16648–16655.

(136) Witoon, T.; Permsirivanich, T.; Kanjanasoontorn, N.; Akkaraphataworn, C.; Seubsai, A.; Faungnawakij, K.; Warakulwit, C.; Chareonpanich, M.; Limtrakul, J. Direct Synthesis of Dimethyl Ether from CO 2 Hydrogenation over Cu–ZnO–ZrO 2 /SO 4 2− –ZrO 2 Hybrid Catalysts: Effects of Sulfur-to-Zirconia Ratios. *Catal. Sci. Technol.* **2015**, *5* (4), 2347–2357.

(137) Flores-Escamilla, G. a.; Fierro-Gonzalez, J. C. Infrared Spectroscopic Study of Dimethyl Ether Carbonylation Catalysed by TiO $_2$ -Supported Rhodium Carbonyls. *Catal. Sci. Technol.* **2015**, *5* (2), 843–850.

(138) LCL, J.; CMBM, B.; L, N.; JR, R. Catalytic Dehydration of Methanol to Dimethyl Ether (DME) Using the Al62,2Cu25,3Fe12,5 Quasicrystalline Alloy. *J. Chem. Eng. Process Technol.* **2013**, *4* (5), 1–8.

(139) Yu, J.; Mao, D.; Han, L.; Guo, Q.; Lu, G. Synthesis of C2 Oxygenates from Syngas over Monodispersed SiO2 Supported Rh-Based Catalysts: Effect of Calcination Temperature of SiO2. *Fuel Process. Technol.* **2013**, *106*, 344–349.

(140) Porosoff, M. D.; Chen, J. G. Trends in the Catalytic Reduction of CO2 by Hydrogen over Supported Monometallic and Bimetallic Catalysts. *J. Catal.* **2013**, *301*, 30–37.

(141) Bouarab, R.; Cherifi, O.; Auroux, A. Reforming of Methane by CO2 in Presence of Cobalt- Based catalystsThis Work Was Presented at the Green Solvents for Catalysis Meeting Held in Bruchsal, Germany, 13–16th October 2002. *Green Chem.* **2003**, *5* (2), 209–212.

(142) Fisher, I. a; Bell, A. T. In-SituInfrared Study of Methanol Synthesis from H2/CO2over Cu/SiO2and Cu/ZrO2/SiO2. *J. Catal.* **1997**, *172* (1), 222–237.

(143) Jia, M.; Li, W.; Xu, H.; Hou, S.; Yu, C.; Ge, Q. The Effect of Additives on Cu/HZSM-5 Catalyst for DME Synthesis. *Catal. Letters* **2002**, *84* (1/2), 31–35.

(144) Samson, K.; Śliwa, M.; Socha, R. P.; Góra-Marek, K.; Mucha, D.; Rutkowska-Zbik, D.; Paul, J.-F.; Ruggiero-Mikołajczyk, M.; Grabowski, R.; Słoczyński, J. Influence of ZrO 2 Structure and Copper Electronic State on Activity of Cu/ZrO 2 Catalysts in Methanol Synthesis from CO 2. *ACS Catal.* **2014**, *4* (10), 3730–3741.

(145) van den Berg, R.; Zečević, J.; Sehested, J.; Helveg, S.; de Jongh, P. E.; de Jong, K. P. Impact of the Synthesis Route of Supported Copper Catalysts on the Performance in the Methanol Synthesis Reaction. *Catal. Today* **2016**, *272*, 87–93.

(146) Nonneman, L. E. Y.; Ponec, V. On the Problem of the Activity in Methanol Synthesis of Supported, Unpromoted Copper Catalysts. *Catal. Letters* **1991**, *7* (1–4), 213–217.

(147) Thi, T. P. T.; Nguyen, D. T.; Duong, T. Q.; Luc, H. H.; Vo, V. Facile Postsynthesis of N-Doped TiO 2 -SBA-15 and Its Photocatalytic Activity. *Adv. Mater. Sci. Eng.* **2013**, *2013*, 1–8.

(148) Xing, M.; Fang, W.; Nasir, M.; Ma, Y.; Zhang, J.; Anpo, M. Self-Doped Ti3+-Enhanced TiO2 Nanoparticles with a High-Performance Photocatalysis. *J. Catal.* **2013**, *297*, 236–243.

(149) Schneider, J.; Matsuoka, M.; Takeuchi, M.; Zhang, J.; Horiuchi, Y.; Anpo, M.; Bahnemann, D. W. Understanding TiO 2 Photocatalysis : Mechanisms and Materials. *Chem. Rev.* **2014**, *114*, 9919–9986.

(150) Kuncewicz, J.; Ohtani, B. Titania Photocatalysis through Two-Photon Band-Gap Excitation with Built-in Rhodium Redox Mediator. *Chem. Commun.* **2015**, *51* (2), 298–301.

(151) Ali, K. A.; Zuhairi, A.; Mohamed, A. R. Recent Development in Catalytic Technologies for Methanol Synthesis from Renewable Sources : A Critical Review. *Renew. Sustain. Energy Rev.* **2015**, *44*, 508–518.

(152) Słoczyński, J.; Grabowski, R.; Kozłowska, A.; Olszewski, P.; Lachowska, M.; Skrzypek, J.; Stoch, J. Effect of Mg and Mn Oxide Additions on Structural and Adsorptive Properties of Cu/ZnO/ZrO2 Catalysts for the Methanol Synthesis from CO2. *Appl. Catal. A Gen.* **2003**, *249* (1), 129–138.

(153) Sakurai, H.; Haruta, M. Carbon Dioxide and Carbon Monoxide Hydrogenation over Gold Supported on Titanium, Iron, and Zinc Oxides. *Appl. Catal. A Gen.* **1995**, *127* (1–2), 93–105.

(154) Arena, F.; Italiano, G.; Barbera, K.; Bordiga, S.; Bonura, G.; Spadaro, L.; Frusteri, F. Solid-State Interactions, Adsorption Sites and Functionality of Cu-ZnO/ZrO2 Catalysts in the CO2 Hydrogenation to CH3OH. *Appl. Catal. A Gen.* **2008**, *350* (1), 16–23.

(155) Wang, G.; Zuo, Y.; Han, M.; Wang, J. Copper Crystallite Size and Methanol Synthesis Catalytic Property of Cu-Based Catalysts Promoted by Al, Zr and Mn. *React. Kinet. Mech. Catal.* **2010**, *101* (2), 443–454.

(156) Degirmenci, V.; Uner, D.; Cinlar, B.; Shanks, B. H.; Yilmaz, A.; Santen, R. A.; Hensen, E. J. M. Sulfated Zirconia Modified SBA-15 Catalysts for Cellobiose Hydrolysis. *Catal. Letters* **2010**, *141* (1), 33–42.

(157) Masoud, N.; Delannoy, L.; Schaink, H.; van der Eerden, A.; de Rijk, J. W.; Silva, T. A. G.; Banerjee, D.; Meeldijk, J. D.; de Jong, K. P.; Louis, C.; de Jongh, P. E. Superior Stability of Au/SiO 2 Compared to Au/TiO 2 Catalysts for the Selective Hydrogenation of Butadiene. *ACS Catal.* **2017**, *7* (9), 5594–5603.

(158) Xin-Chao, S.; Lin-Hai, D.; Yu-Ye, W.; Wen-Guang, Q.; YU, Y.-C.; Yuan, W.; Huai-Lei, L.; Zhao-Lin, S.; Li-Juan, S. Effect of Surface Acidity of CuO-SBA-15 on Adsorptive Desulfurization of Fuel Oils. **2012**, *28* (6), 1467–1473.

(159) Prieto, G.; Meeldijk, J. D.; De Jong, K. P.; De Jongh, P. E. Interplay between Pore Size and Nanoparticle Spatial Distribution: Consequences for the Stability of CuZn/SiO2methanol Synthesis Catalysts. *J. Catal.* **2013**, *303*, 31–40.

(160) Twigg, M. V; Spencer, M. S. Deactivation of Supported Copper Metal Catalysts for Hydrogenation Reactions. *Appl. Catal. A Gen.* **2001**, *212* (1–2), 161–174.

(161) Saltzman, W. M. *Drug Delivery: Engineering Principles for Drug Therapy*; Topics in Chemical Engineering; Oxford University Press, 2001.

(162) Park, K. Controlled Drug Delivery Systems: Past Forward and Future Back. *J. Control. Release* **2014**, *190*, 3–8.

(163) Doadrio, A. L.; Sousa, E. M. B.; Doadrio, J. C.; Pérez Pariente, J.; Izquierdo-Barba, I.; Vallet-Regí, M. Mesoporous SBA-15 HPLC Evaluation for Controlled Gentamicin Drug Delivery. *J. Control. Release* **2004**, *97* (1), 125–132.

(164) Jain, K. K. *Drug Delivery Systems*; 2008; Vol. 437.

(165) Perrie, Y.; Rades, T. *Pharmaceutics: Drug Delivery and Targeting*; Fast Track Series; Pharmaceutical Press, 2009.

(166) Martinho, N.; Damgé, C.; Reis, C. P. Recent Advances in Drug Delivery Systems. *J. Biomater. Nanobiotechnol.* **2011**, *2* (5), 510–526.

(167) Vallet-Regí, M.; Ruiz-González, L.; Izquierdo-Barba, I.; González-Calbet, J. M. Revisiting Silica Based Ordered Mesoporous Materials: Medical Applications. *J. Mater. Chem.* **2006**, *16* (1), 26–31.

(168) Wang, X.; Chen, D.; Cao, L.; Li, Y.; Boyd, B. J.; Caruso, R. a. Mesoporous Titanium Zirconium Oxide Nanospheres with Potential for Drug Delivery Applications. *ACS Appl. Mater. Interfaces* **2013**, *5*, 10926–10932.

(169) Barich, D. H.; Munson, E. J.; Zell, M. T. Physicochemical Properties, Formulation, and Drug Delivery. In *Drug Delivery*; John Wiley & Sons, Inc.: Hoboken, NJ, USA, 2005; pp 57–71.

(170) Lao, L. L.; Peppas, N. a.; Boey, F. Y. C.; Venkatraman, S. S. Modeling of Drug Release from Bulk-Degrading Polymers. *Int. J. Pharm.* **2011**, *418* (1), 28–41.

(171) Holowka, E. P.; Bhatia, S. K. *Drug Delivery*; 2014.

(172) Costa, P.; Sousa Lobo, J. M. Modeling and Comparison of Dissolution Profiles. *Eur. J. Pharm. Sci.* **2001**, *13* (2), 123–133.

(173) Aucoin, H.; Wilson, A.; Wilson, A.; Ishihara, K.; Guiseppi-Elie, A. Release of Potassium Ion and Calcium Ion from Phosphorylcholine Group Bearing Hydrogels. *Polymers (Basel).* **2013**, *5* (4), 1241–1257.

(174) Siepmann, J.; Peppas, N. A. Higuchi Equation: Derivation, Applications, Use and Misuse. *Int. J. Pharm.* **2011**, *418* (1), 6–12.

(175) Dash, S.; Murthy, P. N.; Nath, L.; Chowdhury, P. Kinetic Modeling on Drug Release from Controlled Drug Delivery Systems. *Acta Pol. Pharm.* **2010**, *67* (3), 217–223.

(176) Petrescu, M.; Mitran, R. A.; Luchian, A. M.; Matei, C.; Berger, D. Mesoporous Ceria-Silica Composites as Carriers for Doxycycline. *UPB Sci. Bull. Ser. B Chem. Mater. Sci.* **2015**, *77* (3), 13–24.

(177) Berger, D.; Bajenaru, L.; Nastase, S.; Mitran, R.-A.; Munteanu, C.; Matei, C. Influence of Structural, Textural and Surface Properties of Mesostructured Silica and Aluminosilicate Carriers on Aminoglycoside Uptake and in Vitro Delivery. *Microporous Mesoporous Mater.* **2015**, *206*, 150–160.

(178) Bhatia, S. Nanoparticles Types, Classification, Characterization, Fabrication Methods and Drug Delivery Applications. In *Natural Polymer Drug Delivery Systems*; Springer International Publishing: Cham, 2016; pp 33–93.

(179) Jadhav, S.; Gaikwad, S.; Nimse, M.; Rajbhoj, A. Copper Oxide Nanoparticles: Synthesis, Characterization and Their Antibacterial Activity. *J. Clust. Sci.* **2011**, *22*, 121–129.

(180) Ding, C.; Li, Z. A Review of Drug Release Mechanisms from Nanocarrier Systems. *Mater. Sci. Eng. C* **2017**, *76*, 1440–1453.

(181) De Jong, W. H.; Borm, P. J. A. Drug Delivery and Nanoparticles: Applications and Hazards. *Int. J. Nanomedicine* **2008**, *3* (2), 133–149.

(182) Wang, Z.; Chen, B.; Wu, Q. Increasing the Oral Bioavailability of Poorly Water- Soluble Carbamazepine Using Immediate-Release Pellets Supported on SBA-15 Mesoporous Silica. **2012**, 5807–5818.

(183) Vallet-regí, M.; Balas, F.; Arcos, D. Minireviews Mesoporous Materials for Drug Delivery. **2007**, 7548–7558.

(184) Vallet-Regí, M.; Balas, F. Silica Materials for Medical Applications. *Open Biomed. Eng. J.* **2008**, *2*, 1–9.

(185) Vallet-Regi, M.; Ramila, A. A New Property of MCM-41: Drug Delivery System. *Chem. Mater.* **2001**, No. 11, 308–311.

(186) Rosenholm, J. M.; Sahlgren, C.; Lindén, M. Towards Multifunctional, Targeted Drug Delivery Systems Using Mesoporous Silica Nanoparticles--Opportunities & Challenges. *Nanoscale* **2010**, *2* (10), 1870–1883.

(187) García, A.; Colilla, M.; Izquierdo-Barba, I.; Vallet-Regí, M. Incorporation of Phosphorus into Mesostructured Silicas: A Novel Approach to Reduce the SiO2 Leaching in Water. *Chem. Mater.* **2009**, *21* (18), 4135–4145.

(188) Song, S.-W.; Hidajat, K.; Kawi, S. Functionalized SBA-15 Materials as Carriers for Controlled Drug Delivery: Influence of Surface Properties on Matrix-Drug Interactions. *Langmuir* **2005**, *21* (21), 9568–9575.

(189) de Jongh, P. E.; Eggenhuisen, T. M. Melt Infiltration: An Emerging Technique for the Preparation of Novel Functional Nanostructured Materials. *Adv. Mater.* **2013**, *25* (46), 6672–6690.

(190) Slowing, I. I.; Vivero-Escoto, J. L.; Wu, C.-W.; Lin, V. S.-Y. Mesoporous Silica Nanoparticles as Controlled Release Drug Delivery and Gene Transfection Carriers. *Adv. Drug Deliv. Rev.* **2008**, *60* (11), 1278–1288.

(191) Kato, N.; Kato, N. High-Yield Hydrothermal Synthesis of Mesoporous Silica Hollow Capsules. *Microporous Mesoporous Mater.* **2016**, *219*, 230–239.

(192) Takai, C.; Ishino, T.; Fuji, M.; Shirai, T. Rapid and High Yield Synthesis of Hollow Silica Nanoparticles Using an NH4F Catalyst. *Colloids Surfaces A Physicochem. Eng. Asp.* **2014**, *446*, 46–49.

(193) Tsai, C.-P.; Chen, C.-Y.; Hung, Y.; Chang, F.-H.; Mou, C.-Y. Monoclonal Antibody-

Functionalized Mesoporous Silica Nanoparticles (MSN) for Selective Targeting Breast Cancer Cells. *J. Mater. Chem.* **2009**, *19* (32), 5737.

(194) Moritz, M.; Łaniecki, M. SBA-15 Mesoporous Material Modified with APTES as the Carrier for 2-(3-Benzoylphenyl)propionic Acid. *Appl. Surf. Sci.* **2012**, *258* (19), 7523–7529.

(195) Rosenholm, J. M.; Penninkangas, A.; Lindén, M. Amino-Functionalization of Large-Pore Mesoscopically Ordered Silica by a One-Step Hyperbranching Polymerization of a Surface-Grown Polyethyleneimine. *Chem. Commun. (Camb).* **2006**, No. 37, 3909–3911.

(196) Aznar, E.; Marcos, M. D.; Martínez-Máñez, R.; Sancenón, F.; Soto, J.; Amorós, P.; Guillem, C. pH- and Photo-Switched Release of Guest Molecules from Mesoporous Silica Supports. *J. Am. Chem. Soc.* **2009**, *131* (19), 6833–6843.

(197) Lai, C.-Y.; Trewyn, B. G.; Jeftinija, D. M.; Jeftinija, K.; Xu, S.; Jeftinija, S.; Lin, V. S.-Y. A Mesoporous Silica Nanosphere-Based Carrier System with Chemically Removable CdS Nanoparticle Caps for Stimuli-Responsive Controlled Release of Neurotransmitters and Drug Molecules. *J. Am. Chem. Soc.* **2003**, *125* (15), 4451–4459.

(198) Samuel, S. P.; Li, S.; Mukherjee, I.; Guo, Y.; Patel, A. C.; Baran, G.; Wei, Y. Mechanical Properties of Experimental Dental Composites Containing a Combination of Mesoporous and Nonporous Spherical Silica as Fillers. *Dent. Mater.* **2009**, *25*, 296–301.

(199) Fullriede, H.; Timpe, N.; Borchers, L.; Stiesch, M.; Menzel, H.; Behrens, P.; Chemie, A.; Hannover, L. U.; Chemie, T.; Braunschweig, T. U.; Prothetik, Z. A NTIBACTERIAL SILICA NANOPARTICLES WITH P H-SENSITIVE RELEASE PROPERTIES AS FILLERS FOR DENTAL DENTA L COMPOSITE MATERIALS. **2013**, *58*, 9–10.

(200) Bowen, R. L.; Reed, L. E. Semiporous Reinforcing Fillers for Composite Resins: I. Preparation of Provisional Glass Formulations. *J. Dent. Res.* **1976**, *55* (5), 738–747.

(201) Vallet-Regi, M.; Doadrio, J. C.; Doadrio, A. L.; Izquierdo-Barba, I.; Perez-Pariente, J. Hexagonal Ordered Mesoporous Material as a Matrix for the Controlled Release of Amoxicillin. *Solid State Ionics* **2004**, *172* (1–4), 435–439.

(202) Ng, J. B. S.; Kamali-Zare, P.; Brismar, H.; Bergstr??m, L. Release and Molecular Transport of Cationic and Anionic Fluorescent Molecules in Mesoporous Silica Spheres. *Langmuir* **2008**, *24* (19), 11096–11102.

(203) Demuth, P.; Hurley, M.; Wu, C.; Galanie, S.; Zachariah, M. R.; Deshong, P. Mesoscale Porous Silica as Drug Delivery Vehicles: Synthesis, Characterization, and pH-Sensitive Release Profiles. *Microporous Mesoporous Mater.* **2011**, *141* (1–3), 128–134.

(204) Hisbergues, M.; Vendeville, S.; Vendeville, P. Review Zirconia: Established Facts and Perspectives for a Biomaterial in Dental Implantology. *J. Biomed. Mater. Res. - Part B Appl. Biomater.* **2009**, *88*, 519–529.

(205) Asadpour, E.; Boroushaki, M. T.; Ghorbani, A.; Sadeghnia, H. R. Effect of Zirconium Dioxide Nanoparticles on Glutathione Peroxidase Enzyme in PC12 and N2a Cell Lines. *Iran. J. Pharm. Res.* **2014**, *13* (4), 1141–1148.

(206) Otero-González, L.; García-Saucedo, C.; Field, J. A.; Sierra-Álvarez, R. Toxicity of TiO_2, ZrO_2,

Fe^0, Fe_2O_3, and Mn_2O_3 Nanoparticles to the Yeast, Saccharomyces Cerevisiae. *Chemosphere* **2013**, *93* (6), 1201–1206.

(207) Karunakaran, G.; Suriyaprabha, R.; Manivasakan, P.; Yuvakkumar, R.; Rajendran, V.; Kannan, N. Screening of in Vitro Cytotoxicity, Antioxidant Potential and Bioactivity of Nano- and Micro-ZrO2 and -TiO2 Particles. *Ecotoxicol Env. Saf* **2013**, *93*, 191–197.

(208) Jangra, S. L.; Stalin, K.; Dilbaghi, N.; Kumar, S.; Tawale, J.; Singh, S. P.; Pasricha, R. Antimicrobial Activity of Zirconia (ZrO2) Nanoparticles and Zirconium Complexes. *J. Nanosci. Nanotechnol.* **2012**, *12* (9), 7105–7112.

(209) Grass, G.; Rensing, C.; Solioz, M. Metallic Copper as an Antimicrobial Surface. *Appl. Environ. Microbiol.* **2011**, *77* (5), 1541–1547.

(210) Konieczny, J.; Rdzawski, Z. Antibacterial Properties of Copper and Its Alloys. *Arch. Mater. Sci. Eng.* **2012**, *56* (2), 53–60.

(211) Argueta-Figueroa, L.; Morales-Luckie, R. A.; Scougall-Vilchis, R. J.; Olea-Mejía, O. F. Synthesis, Characterization and Antibacterial Activity of Copper, Nickel and Bimetallic Cu-Ni Nanoparticles for Potential Use in Dental Materials. *Prog. Nat. Sci. Mater. Int.* **2014**, *24* (4), 321–328.

(212) Raffi, M.; Mehrwan, S.; Bhatti, T. M.; Akhter, J. I.; Hameed, A.; Yawar, W.; Ul Hasan, M. M. Investigations into the Antibacterial Behavior of Copper Nanoparticles against Escherichia Coli. *Ann. Microbiol.* **2010**, *60*, 75–80.

(213) Esteban-Cubillo, A.; Pecharromán, C.; Aguilar, E.; Santarén, J.; Moya, J. S. Antibacterial Activity of Copper Monodispersed Nanoparticles into Sepiolite. *J. Mater. Sci.* **2006**, *41*, 5208–5212.

(214) Cioffi, N.; Torsi, L.; Ditaranto, N.; Tantillo, G.; Ghibelli, L.; Sabbatini, L.; Bleve-Zacheo, T.; D'Alessio, M.; Zambonin, P. G.; Traversa, E. Copper Nanoparticle/polymer Composites with Antifungal and Bacteriostatic Properties. *Chem. Mater.* **2005**, *17* (7), 5255–5262.

(215) Pinto, R. J. B.; Daina, S.; Sadocco, P.; Neto, C. P.; Trindade, T. Antibacterial Activity of Nanocomposites of Copper and Cellulose. *Biomed Res. Int.* **2013**, *2013*.

(216) Chatterjee, A. K.; Chakraborty, R.; Basu, T. Mechanism of Antibacterial Activity of Copper Nanoparticles. *Nanotechnology* **2014**, *25*, 135101.

(217) Silva, H. F. O.; Lima, K. M. G.; Cardoso, M. B.; Oliveira, J. F. a.; Melo, M. C. N.; Sant'Anna, C.; Eugênio, M.; Gasparotto, L. H. S. Doxycycline Conjugated with Polyvinylpyrrolidone-Encapsulated Silver Nanoparticles: A Polymer's Malevolent Touch against Escherichia Coli. *RSC Adv.* **2015**, *5* (82), 66886–66893.

(218) Ren, G.; Hu, D.; Cheng, E. W. C.; Vargas-Reus, M. a.; Reip, P.; Allaker, R. P. Characterisation of Copper Oxide Nanoparticles for Antimicrobial Applications. *Int. J. Antimicrob. Agents* **2009**, *33*, 587–590.

(219) Kovtun, A.; Kozlova, D.; Ganesan, K.; Biewald, C.; Seipold, N.; Gaengler, P.; Arnold, W. H.; Epple, M. Chlorhexidine-Loaded Calcium Phosphate Nanoparticles for Dental Maintenance Treatment: Combination of Mineralising and Antibacterial Effects. *RSC Adv.* **2012**, *2* (3), 870.

(220) do Amorim, C. V. G.; Aun, C. E.; Mayer, M. P. A. Susceptibility of Some Oral Microorganisms to Chlorhexidine and Paramonochlorophenol. *Braz. Oral Res.* **2004**, *18* (3), 242–246.

(221) McDonnell, G; Russell, A. Antiseptics and Disinfectants : Activity , Action , and Resistance. *Am. Soc. Microbiol.* **1999**, *12* (1), 147–179.

(222) Attin, T.; Abouassi, T.; Becker, K.; Wiegand, A.; Roos, M.; Attin, R. A New Method for Chlorhexidine (CHX) Determination: CHX Release after Application of Differently Concentrated CHX-Containing Preparations on Artificial Fissures. *Clin. Oral Investig.* **2008**, *12* (3), 189–196.

(223) Russell, A. D.; Day, M. J. Antibacterial Activity of Chlorhexidine. *J. Hosp. Infect.* **1993**, *25* (4), 229–238.

(224) Deo, V.; Ansari, S.; Mandia, S.; Bhongade, M. Therapeutic Efficacy of Subgingivally Delivered Doxycycline Hyclate as an Adjunct to Non-Surgical Treatment of Chronic Periodontitis. *J. Oral Maxillofac. Res.* **2010**, *2* (1), 1–7.

(225) Al Hulami, H.; Babay, N.; Awartani, F.; Anil, S. The Effect of Locally Delivered Doxycycline as an Adjunctive Therapy to Scaling and Root Planing in Smokers. *Saudi Dent. J.* **2011**, *23* (3), 143–148.

(226) Machion, L.; Andia, D. C.; Lecio, G.; Nociti, F. H.; Casati, M. Z.; Sallum, A. W.; Sallum, E. A. Locally Delivered Doxycycline as an Adjunctive Therapy to Scaling and Root Planing in the Treatment of Smokers: A 2-Year Follow-Up. *J. Periodontol.* **2006**, *77* (4), 606–613.

(227) Condon, J. B. *Surface Area and Porosity Determinations by Physisorption*; Elsevier, 2006.

(228) Sing, K. S. W. Physisorption of Nitrogen by Porous Materials. *J. Porous Mater.* **1995**, *2* (1), 5–8.

(229) Thommes, M.; Kaneko, K.; Neimark, A. V.; Olivier, J. P.; Rodriguez-Reinoso, F.; Rouquerol, J.; Sing, K. S. W. Physisorption of Gases, with Special Reference to the Evaluation of Surface Area and Pore Size Distribution (IUPAC Technical Report). *Pure Appl. Chem.* **2015**, *87* (9–10), 1051–1069.

(230) Condon, J. B. (total pdf). *Surface Area and Porosity Determinations by Physisorption, Measurements and Theory*; 2006.

(231) Xiao Jiang, Naoto Koizumi, A.; Guo, X.; Song, and C. Bimetallic Pd-Cu Catalysts for Selective CO2 Hydrogenation to Methanol.

(232) Jaroniec, M.; Solovyov, L. A. Improvement of the Kruk–Jaroniec–Sayari Method for Pore Size Analysis of Ordered Silicas with Cylindrical Mesopores. *Langmuir* **2006**, *22* (16), 6757–6760.

(233) Kruk, M.; Jaroniec, M.; Ko, C. H.; Ryoo, R. Characterization of the Porous Structure of SBA-15. *Chem. Mater.* **2000**, *12* (7), 1961–1968.

(234) Kruk, M.; Jaroniec, M.; Sayari, A. Application of Large Pore MCM-41 Molecular Sieves to Improve Pore Size Analysis Using Nitrogen Adsorption Measurements. *Langmuir* **1997**, *7463* (12), 6267–6273.

(235) Condon, J. B. *Surface Area and Porosity Determinations by Physisorption*; Elsevier, 2006.

(236) Webb, P. A. Introduction to Chemical Adsorption Analytical Techniques and Their Applications to Catalysis. **2003**, No. January.

(237) Gallacher, P. K. *Handbook of Thermal Analysis and Calorimetry*; 1998; Vol. 1.

(238) Webb, P.; Orr, C.; Corporation., M. I. *Analytical Methods in Fine Particle Technology*; Micromeritics Instrument Corp.: Norcross, Ga., 1997.

(239) Jenkins, R. X-Ray Techniques: Overview. *Encycl. Anal. Chem.* **2000**, 13269–13288.

(240) Ingham, B. X-Ray Scattering Characterisation of Nanoparticles. *Crystallogr. Rev.* **2015**, *21* (4), 229–303.

(241) Patterson, A. L. The Scherrer Formula for X-Ray Particle Size Determination. *Phys. Rev.* **1939**, *56* (10), 978–982.

(242) Egerton, R. F. *Physical Principles of Electron Microscopy*; Springer US: Boston, MA, 2005; Vol. 24.

(243) Stuart, B. H. *Infrared Spectroscopy: Fundamentals and Applications*; Analytical Techniques in the Sciences; John Wiley & Sons, Ltd: Chichester, UK, 2004; Vol. 8.

(244) Armaroli, T.; Bécue, T.; Gautier, S. Diffuse Reflection Infrared Spectroscopy (Drifts): Application to the in Situ Analysis of Catalysts. *Oil Gas Sci. Technol.* **2004**, *59* (2), 215–237.

(245) Harrick, N. J.; Beckmann, K. H. Internal Reflection Spectroscopy. In *Characterization of Solid Surfaces*; Kane, P. F., Larrabee, G. B., Eds.; Springer US: Boston, MA, 1974; pp 215–245.

(246) Harvey, D. *Modern Analytical Chemistry*; McGraw-Hill, 1999.

(247) Watts, J. F.; Wolstenholme, J. *An Introduction to Surface Analysis by XPS and AES*; John Wiley & Sons, Ltd: Chichester, UK, 2003; Vol. 27.

(248) Briggs, D. Handbook of X-Ray Photoelectron Spectroscopy C. D. Wanger, W. M. Riggs, L. E. Davis, J. F. Moulder and G. E.Muilenberg Perkin-Elmer Corp., Physical Electronics Division, Eden Prairie, Minnesota, USA, 1979. 190 Pp. $195. *Surf. Interface Anal.* **1981**, *3* (4), v–v.

(249) Hajšlová, J.; Čajka, T. Gas Chromatography–mass Spectrometry (GC–MS). In *Food Toxicants Analysis*; Elsevier, 2007; pp 419–473.

(250) Stashenko, E.; Ren, J. Gas Chromatography-Mass Spectrometry. In *Advances in Gas Chromatography*; InTech, 2014; pp 1–38.

(251) de Hoffmann, E.; Stroobant, V. *Mass Spectrometry: Principles and Applications*; Wiley, 2007.

(252) Glish, G. L.; Vachet, R. W. The Basics of Mass Spectrometry in the Twenty-First Century. *Nat. Rev. Drug Discov.* **2003**, *2* (2), 140–150.

APPENDED PAPERS

Paper 1

Synthesis of a Cu-infiltrated Zr-doped SBA-15 catalyst for CO_2 hydrogenation into methanol and dimethyl ether

A. Atakan, P. Mäkie, F. Söderlind, J. Keraudy, E.M. Björk, and M. Odén

Phys. Chem. Chem. Phys. 19 (2017) 19139
DOI: 10.1039/C7CP03037A

ATTENTION¡¡
Pages 98 to 113 of the thesis are available at the editor's web
https://pubs.rsc.org/en/content/articlelanding/2017/cp/c7cp03037a#!divAbstract

Paper 2

Effects of the chemical state of mesoporous CuO_x-Zr-SiO_2 catalysts on CO_2 hydrogenation

A. Atakan, J. Keraudy, P. Mäkie, Christian Hulteberg, E.M. Björk, and M. Odén

Submitted for publication

Effects of the chemical state of mesoporous CuO_x-Zr-SiO_2 catalysts on CO_2 hydrogenation

Aylin Atakan[1,*], Julien Keraudy[2], Peter Mäkie[1], Christian Hulteberg[3], Emma M. Björk[1], and Magnus Odén[1]

[1] Nanostructured Materials, Department of Physics, Chemistry and Biology, Linköping University, Linköping SE-58183, Sweden

[2] Plasma and Coatings Physics, Department of Physics, Chemistry and Biology, Linköping University, Linköping SE-58183, Sweden

[3] Department of Chemical Engineering, Lund University, Lund SE-22100, Sweden

* aylin.atakan@liu.se

Zr doped SBA-15; Cu nanoparticles; CO_2 hydrogenation; methanol; dimethyl ether

ABSTRACT: A catalytic assembly consisting of Zr-doped mesoporous silica (Zr-SBA-15) supports with intergrown Cu nanoparticles was used to study the effects of its chemical states on CO_2 hydrogenation. The chemical states of the final material was altered by using tetraethyl orthosilicate (TEOS) or sodium metasilicate (SMS) as the silica precursor in the synthesis of the Zr-SBA-15 framework, and infiltration (*Inf*) or evaporation induced wetness impregnation (*EIWI*)) as the Cu loading method. It was found that the silica precursor mainly affects the activity of the catalyst whereas the Cu loading method alters the selectivity of the reaction products. Samples prepared with TEOS exhibit a higher catalytic activity compared to SMS materials due to different Zr dispersion and bonding to the silica matrix. Catalysts prepared by *EIWI* display selectivity for methanol formation, while the ones prepared by *Inf* enable methanol conversion to DME. This is correlated to a higher Zr content and lower Cu oxidation states of *EIWI* prepared catalysts. The results demonstrate the importance of taking the chemical state of a hybrid catalyst into account to control the yield and selectivity of the catalyzed reaction.

1. INTRODUCTION

The increasing concentration of CO_2 in the atmosphere affects the global climate. To reverse this trend, two main world-wide strategies are adopted: (1) reducing the amount of CO_2 emissions by modifying processes or (2) eliminating/consuming the already emitted CO_2 by introducing new processes[1,2]. In this respect, consumption of CO_2 in processes such as hydrogenation is an important way to reduce the CO_2 emission and instead convert it into valuable resources such as methanol and dimethyl ether (DME). Methanol, is a potent molecule, not only for use as a chemical feedstock and solvent, but also as a H_2 storing agent and a fuel[2–5]. DME can also be used as a fuel and to store methanol since methanol production from CO_2 hydrogenation is thermodynamically limited[6,7]. Potentially, many products may form when hydrogenating CO_2, e.g. CO, CH_4, ethanol, butane etc. and therefore a selective catalyst is needed.

Among the metals studied so far, Cu with a favorable morphology integrated in a support has shown significant catalytic properties and remains as the main component of a heterogenous catalyst for CO_2 hydrogenation[2,8–11]. In an integrated catalyst, SiO_2 and ZrO_2 are favorable supports and promoters for Cu due to their high chemical and mechanical stability, low price, lack of toxic effects, and contribution to the Cu dispersion efficiency[2,4,6,12–17]. Catalyst development typically relies on tailoring the properties of the support to add features for a targeted task[13,18–20], e.g. by introducing porosity to increase the surface area. Using SBA-15[21], a mesoporous SiO_2, as a support for Cu is a result of this strategy. SBA-15 offers a large specific surface area and its tunable pore size can be used to control the size of the nanoparticles (NP) grown in the pores. Moreover, it is possible to dope an alien atom into the SiO_2 framework to introduce new properties. It has been shown that doping SBA-15 with Zr improves the catalytic activity due to promoted acidity of the catalyst and improved dispersion of the active Cu phase [14,22].

Various nanoassemblies based on SBA-15 have been reported in earlier studies[19,23,24]. However, systematic studies of how alterations of the chemical state of these catalysts affect CO_2 hydrogenation are sparse. In most studies where SBA-15 (doped or undoped) is used as the support, tetraethyl orthosilicate (TEOS) is used as the silica precursor[25]. TEOS is not toxic and it provides a robust formation route giving opportunity to physical alterations and atomic modifications without destroying the mesoporous framework[26–30]. It has also been reported that the cheaper sodium metasilicate (SMS) can be a good candidate to replace TEOS[31,32]. However, nanoengineering SBA-15 with SMS as the precursor remains a challenging task since SMS is a less studied reagent.

The method for incorporating Cu in the porous network can also influence the physical characteristics of the catalytically active assembly. Wetness impregnation technique is one of the most common method for growing Cu NPs in a porous support[19,28,33,34]. In comparison, the infiltration method (*Inf*)[35] offers better Cu NP dispersion since functional groups are attached to the support surface. Another technique for Cu incorporation is evaporation induced wetness impregnation (*EIWI*)[36]. Despite the efficiency in Cu NP confinement to the pores and advantages in terms of price, time, health risks, and envi-

ronmental hazardousness, *EIWI* has received less attention compared to *Inf.*

In this paper, a hybrid catalyst comprising of Cu NPs integrated into a Zr-SBA-15 mesoporous support has been synthesized using two different silica precursors (TEOS and SMS) and two Cu loading methods (*Inf* and *EIWI*). The impact of the resulting different chemical states of the final nanoassembly on the physical characteristics of the Zr-SBA-15 support and the resulting CO_2 catalytic activity such as yield and selectivity are discussed.

2. EXPERIMENTAL SECTION

Pluronic P123 block copolymer ($EO_{20}PO_{70}EO_{20}$, av. M_n~5800, Aldrich), ammonium fluoride (NH_4F) (≥98.0%, puriss p.a., ACS reagent,Fluka), HCl (≥37.0%, puriss. p.a., ACS reagent, fuming, Sigma-Aldrich), heptane (99%, ReagentPlus®, Sigma-Aldrich), tetraethyl orthosilicate (TEOS, 98%, reagent grade, Sigma-Aldrich), sodium metasilicate (Na_2SiO_3), zirconium(IV) oxychloride octahydrate ($ZrOCl_2{\cdot}8H_2O$, ≥98.0%, puriss p.a., Sigma-Aldrich), chlorotrimethylsilane (TMCS, ≥99.0%, Aldrich), (3-aminopropyl)trimethoxysilane (APTMS, 97%, Aldrich), toluene (≥99.7%, puriss p.a., ACS reagent, reag. ISO, reag. Ph Eur, Sigma-Aldrich), and copper(II) sulfate pentahydrate ($CuSO_4.5H_2O$, ≥99%, ACS reagent, reag. ISO, reag. Ph Eur, Sigma-Aldrich) were used as received.

2.1. Catalyst Synthesis

The catalysts were prepared in two main steps. First Zr-SBA-15 supports were synthesized which was followed by the incorporation of Cu NPs into the supports.

The Zr-SBA-15 synthesis used is based on a method described elsewhere[37]. In a typical synthesis, 2.4 g of P123, 28 mg of NH_4F and 0.74 g of $ZrOCl_2$ were dissolved in 80 ml (for TEOS) or 66 ml (for SMS) of 1.84 M HCl at 20 °C. The silica precursor (5 ml of TEOS or 2.73 g of SMS pre-hydrolyzed in 14 ml of 1.84 M HCl) and 2 ml of heptane were mixed, added to the main solution, and vigorously stirred for 4 minutes. The final solution was kept under static conditions at 20 °C for 5 hours and then transferred to a PTFE flask for hydrothermal treatment at 100 °C for 24 hours. The final slurry was filtered and washed with deionized water. Parts of the recovered powder was calcined at 550°C for 5 hours for future analysis. The samples are labeled as [TEOS] and [SMS], according to the used silica precursor.

Cu NPs were grown in the pores of the Zr-SBA-15 supports via two methods: infiltration (*Inf)* or evaporation induced wetness impregnation (*EIWI). Inf* was performed by a selective functionalization procedure[35,37] where the external surface of the Zr-SBA-15-particle was passivated by attaching methyl ($-CH_3$) groups and the internal pore walls were activated by attaching amine groups. For the external passivation, uncalcined Zr-SBA-15 was stirred into 15 vol% TMCS in toluene with a concentration of 10 g/L at 80 °C for 8 hours under reflux. The suspension was then cooled down, filtered, and the recovered particles washed with toluene. The collected material was then calcined at 300°C for 5 hours. For internal activation, the TMCS treated sample was stirred in 6.25 vol% APTMS in toluene with a concentration of 5.9 g/L for 24 hours at room temperature. Excess APTMS was removed by soxhlet extraction for 5 hours. The suspension was then cooled down, filtered, and the recovered particles washed with toluene. For Cu incorporation, the functionalized material was stirred at a concentration of 20 g/L at room temperature in 0.06 M $CuSO_4$ overnight. The mixture was then filtered and the recovered particles washed with deionized water. The powder was then mixed (20 g/L) with 0.1 M $NaBH_4$ to reduce the Cu ions attached to the surface of the support. Finally the sample was calcined at 550°C for 5 hours. The obtained samples are labeled as [TEOS_Inf] and [SMS_Inf].

EIWI was performed by mixing (20 g/L) calcined Zr-SBA-15 into 0.06 M $CuSO_4$. The mixture was stirred at 80 °C with the outlet open until all the water had evaporated. The powder was then mixed (20 g/L) with 0.1 M $NaBH_4$ for Cu reduction. The resulting material was calcined at 550 °C for 5 hours and labeled as [TEOS_EIWI] and [SMS_EIWI].

2.2. Characterization

The Cu NPs and the pore structure of Zr-SBA-15 supports were imaged by transmission electron microscopy (TEM) using a FEI Tecnai G2 operated at 200 kV. The samples were prepared by suspending the powders in ethanol and drop-vise placed on carbon coated copper grids.

Imaging of the support and external Cu NP morphology was carried out with scanning electron microscopy (SEM) using a LEO 1550 Gemini operated at 3 kV and equipped with an Oxford X-Max 80 energy dispersive x-ray spectrometer (EDS). For EDS analysis the SEM was operated at 20 kV. The EDS was calibrated using 6 different powder mixtures of SiO_2 and ZrO_2 with known Si/Zr atomic ratios.

A Micromeritics ASAP 2020 was used to measure the nitrogen physisorption isotherms at 196°C. The recorded data was used to extract the specific surface area (SSA) with the Brunauer Emmet Teller method[38] within a P/P_0 interval of 0.08-0.16, and the total pore volume at P/P_0=0.997. The pore size distribution was calculated using the Kruk Jaroniec Sayari (KJS) method[39] at the adsorption branch of the isotherms. The micropore volume with calculated by t-plot method[40] .

Fourier transformed infrared spectroscopy (FTIR) was performed in transmission mode for bond structure investigation. For this, a Bruker Vertex 70 device equipped with a LN2 cooled broad band MCT detector and a water cooled glowbar MIR source was used with 2 cm^{-1} resolution. The measurement was conducted on pressed KBr tablets containing 1 mg of sample.

X-ray diffractometry (XRD) was performed using a Panalytical Empyrean x-ray diffractometer equipped with a Cu Kα x-ray source operated at 45 kV and 40 mA. Small angle x-ray diffractometry (SAXRD) was conducted in transmission mode at 0-2.5° for determining the pore packing structure in the samples and extracting the unit cell parameter. The pore wall thickness was determined by subtracting the pore size from the unit cell parameters. The same equipment but operated in reflection mode was used to determine the crystalline structure of the Cu NPs.

X-ray photoemission spectroscopy (XPS) spectra were recorded on a Kratos Ultra photoelectron spectrometer equipped with a monochromated Al Kα (1486.6 eV) x-ray source operating at 150 W. The pressure in the analysis chamber was kept below 10^{-7} Pa at all times during the acquisition process. The experimental conditions were such that the full width at half maximum (FWHM) of $Ag3d_{5/2}$ peak from the reference Ag sample was 0.45 eV. High-resolution spectra of Cu*2p* and Zr*3d* core levels were recorded using a pass energy of 20 eV at $\theta = 0°$ take-off angle (angle between the speci-

men surface normal and the detection direction). All spectra were calibrated in energy by setting adventitious carbon C1s at 284.7 eV (binding energy). In this study, no Ar-etching was carried out before spectra acquisitions. The data were treated with the CasaXPS software, using Shirley backgrounds and a Gaussian-Lorenzian (70-30 ratio) function to account for the different components.

NH_3 temperature programmed desorption (NH_3-TPD) measurements were carried out using a Micromeritics 3-FLEX. The NH_3-TPD spectra were recorded with a thermal conductivity detector (TCD). Prior the measurements, each catalyst was reduced at 400°C under a 100 ml/min hydrogen gas flow (4% in Ar), then cooled to 100°C, and exposed to NH_3 with a constant flow of 10 ml/min during 10 min. Afterwards, all catalysts were exposed to a constant helium flow of 10 ml/min for 1 hour at 100°C, in order to evacuate the physisorbed NH_3. Finally, the temperature was ramped up to about 750°C at a rate of 10°C/min while recording the amount of desorbed ammonia.

2.3. Catalytic activity

The catalytic activity was analyzed in a high-pressure high-temperature (HPHT) cell with a 13 mL total internal volume from Harrick Scientific. For each test, 0.4 g of catalyst material was pressed into discs, placed in the cell, and reduced under H_2 flow at 400 °C for 9 hours. The temperature was then reduced to 250°C and CO_2 and H_2 were fed into the cell at a molar ratio of CO_2/H_2 = 1/3 to a total pressure of 33 bar. The reaction was monitored for 5 days during which the reactants and products were analyzed *in-situ* by diffuse reflectance infrared Fourier transform spectroscopy (DRIFTS) using the previously described IR-spectrometer. Spectra were acquired with a 4 cm^{-1} resolution and each spectrum is an average of 128 scans. KBr was used as background.

A Bruker 450-GC gas chromatograph equipped with a flame ionization detector (FID) and a Bruker SCION mass spectrometer (GC-MS) was used for determining the conversion of CO_2. For this, the resulting gas mixture was transferred from the HPHT cell to the GC-MS in three portions. The molar content in each portion was measured and the average of the measured concentrations was used to calculate the CO_2 conversion to DME and methanol (MeOH).

$$Conversion\% = \frac{C_P}{C_P + C_{Rr}} \quad (1);$$

where C_P is the molar concentration (%) of the product(s) of interest in the final gas mixture and C_{Rr} is the molar concentration of all other spices in the final gas mixture. Therefore the 'conversion%' in Eq (1) represents conversion to the chosen products only. Accordingly, for our experiments, the conversion% values are calculated using Eq (2), (3) and (4) below.

$$CO_2\ conversion\ to\ DME\ and\ MeOH\ \% = \frac{(MeOH\% + 2 * DME\%)}{(MeOH\% + 2 * DME\%) + \frac{[100 - 2 * (MeOH\% + 2 * DME\%)]}{4}} \quad (2)$$

$$CO_2 conversion\ to\ DME\ \% = \frac{2*DME\%}{2*DME\% + \frac{[100-2*(2*DME\%)]}{4}} \quad (3)$$

$$CO_2 conversion\ to\ MeOH\ \% = \frac{MeOH\%}{MeOH\% + \frac{[100 - 2 * (MeOH\%)]}{4}} \quad (4)$$

3. RESULTS

Figure 1 shows the morphology of the Zr-SBA-15 synthesized with TEOS (Figure 1(a)) and SMS (Figure 1(b)). [TEOS] displays monodispersed particles with rod morphology whereas [SMS] consists of particles with a platelet morphology.

Both materials show similar 500±100 nm particle heights, i.e. pore lengths, but different cross sectional diameters: 400±100 nm for [TEOS] and 2.5±0.5 µm for [SMS].

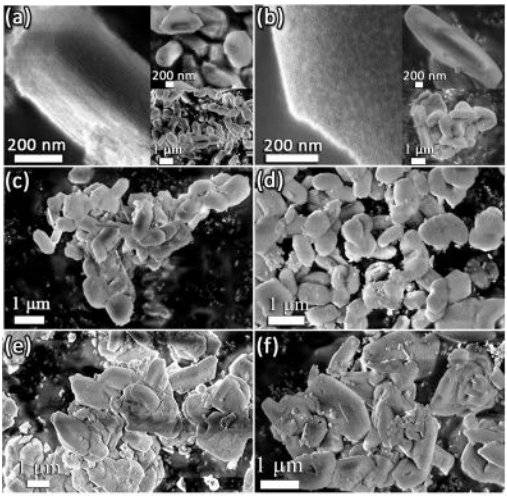

Figure 1. SEM micrographs of Zr-SBA-15 samples: [TEOS] **(a)** and [SMS] **(b)**, and the Cu-Zr-SBA-15 samples [TEOS_Inf] **(c)**, [TEOS_EIWI] **(d)**, [SMS_Inf] **(e),** and [SMS_EIWI] **(f)**.

Table 1. The physicochemical properties of the as-synthesized materials.

Sample Name	Si/Zr atomic ratio	Mean Cu weight %	Specific Surface Area (m^2/g)	Pore size (nm)	Pore volume (cm^3/g)	Micropore volume (cm^3/g)	d-spacing (nm)	Wall thickness (nm)
[TEOS]	10.8	-	736	14.8	1.3	0.05	16.0	1.1
[SMS]	10.2	-	482	11.7	0.9	0.00	12.7	1.0
[TEOS_Inf]	19.0	12.7	422	13.3	0.8	0.02	15.8	2.5
[SMS_Inf]	28.3	14.6	450	10.9	0.7	0.00	13.0	2.1
[TEOS_EIWI]	11.3	15.6	316	13.0	0.8	0.00	14.9	1.9
[SMS_EIWI]	11.5	15.6	279	9.7	0.6	0.00	11.5	1.8

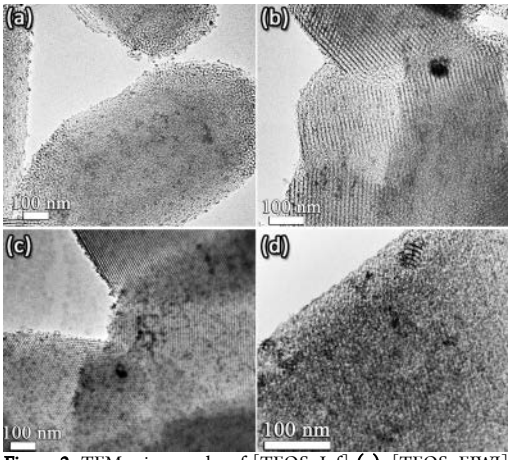

Figure 2. TEM micrographs of [TEOS_Inf] **(a)**, [TEOS_EIWI] **(b)**, [SMS_Inf] **(c)**, and [SMS_EIWI] **(d)**.

SEM micrographs of the as-synthesized Cu-Zr-SBA-15 catalysts are presented in Figure 1(c-f). Formations of Cu NPs on the outer surface (external Cu NPs) of the Zr-SBA-15 supports were observed for all materials. The concentration of external Cu NPs is higher for *SMS* materials than *TEOS*, while no distinct difference was observed for the two Cu-loading methods. TEM micrographs in Figure 2 show the porous network of Zr-SBA-15 with cylindrical pores hexagonally packed parallel to each other as well as the internal Cu NPs in all the supports. No alteration in the morphology of Zr-SBA-15 particles could be observed upon growth of Cu NPs.

The Si/Zr atomic ratio was found to be ~10 for both [TEOS] and [SMS] prior to Cu loading, indicating a complete incorporation of Zr into the mesoporous silica framework (Table 1). A similar value was also found for *EIWI* materials, whereas half of the Zr was lost during Cu loading by the *Inf* method (Table 1) due to the high elution strength of toluene[37]. The Cu-content was found to be between 12 and 16 wt.% for all samples.

Nitrogen sorption measurements show type IV isotherms for both unloaded and Cu-loaded supports with type 1 hysteresis loops, characteristic for mesoporous materials with open cylindrical pores[41] (Figure 3(a,b)). After Cu-loading, the desorption branch of the hysteresis loop is distorted as a result of blockage of Cu NPs present inside the mesopores[19,42–44]. The narrow pore size distributions (Figure 3 (a,b)) confirm uniform pore size for all materials. As expected, the pore size decreases slightly when Cu NPs are present. The textural parameters of all synthesized samples are summarized in Table 1 including pore size, specific surface area (SSA), and pore volume. These parameters are higher for all *TEOS* samples compared to *SMS* samples and all decrease upon Cu-loading.

Figure 3(c,d) shows FTIR transmission spectra of unloaded and Cu-loaded Zr-SBA-15 supports. All the FTIR spectra show an absorption band at around 975 cm^{-1}, which is assigned to the Zr-O-Si bond[14,45,46]. All the other bands, 465, 801, 1085, and 1230 cm^{-1} are typical for SBA-15 supports and attributed to the bending vibration of Si-O-Si bonds[47,48]. The band at 1640 cm^{-1} and the broad peak between 3200-3600 cm^{-1} are assigned to the H-O-H symmetrical vibrations of adsorbed water and the hydroxyl groups on the silica surface[33,49], respectively. The intensity (I) of these peaks varies as $I^{Inf} > I^{EIWI} > I^{unloaded\ support}$ for both *TEOS* and *SMS* samples. After Cu loading, all the main bands are still present with the addition of a band at about 590 cm^{-1} which is ascribed to Cu-O[50,51].

The SAXRD diffractograms (Figure 3(e)) of [TEOS] and [SMS] display one intense 100 reflection and three smaller peaks assigned as 110, 200 and 210. This confirms the ordered, 2-dimensional, hexagonal pore structure. These peaks remain upon Cu loading even though the intensities decreased for [SMS] samples.

The d-spacings and the extracted wall thicknesses are listed in Table 1. Cu-loading by *EIWI* decreased the d-spacings while *Inf* did not affect the d-spacings (Table 1). The wall thickness increased upon Cu loading, and more so for samples prepared by the *Inf* method compared to the *EIWI* method (Table 1).

The x-ray diffractograms of the as-synthesized Cu loaded catalysts are shown in Figure 4(a). All observed peaks stem from copper oxide, CuO (PDF#00-048-1548), except [SMS_EIWI], which shows additional peaks from ZrO_2 (PDF#01-079-1764) at 30.2° and 50.2° 2θ. The presence of ZrO_2 in the [SMS_EIWI] indicates inhomogeneous Zr-doping or aggregation of Zr-O during the Cu-loading. XRD diffractograms of reduced samples (Figure 4(b)) display the presence of Cu metal (PDF#00-004-0836) in [SMS_Inf], [TEOS_EIWI] and [SMS_EIWI], indicating a nearly complete reduction of the Cu NPs. However, in [TEOS_Inf], traces of CuO could still be observed.

XPS results of Zr $3d_{3/2}$ and $3d_{5/2}$ core levels (Figure S1 in the Supporting Information) indicate the existence of Zr-O bonds in all the samples in their as-synthesized and reduced forms. Representative XPS core-level Cu 2p spectra of as synthesized Cu/Zr-SBA-15 samples (Figure 4(c)) reveal the presence of Cu with different oxidation states. All Cu 2p spectra exhibit a main peak at 933.5 ± 0.2 eV accompanied by shoulders at 935.2 ± 0.2 eV and at 932.3 ± 0.3 eV, indicating contributions of Cu^{2+}, Cu^{3+} and Cu^{+} species, respectively[52–55]. However, it is not possible to distinguish Cu^0 from Cu^+ at 932.2-932.4 eV because of their spectral overlap[56]. This peak is therefore labeled as Cu^+/Cu^0. The strongest signal is seen for Cu^{2+} while Cu^{3+} and Cu^+/Cu^0 are weaker, which is in a good agreement with the XRD results. The content of each Cu oxidation state was determined by fitting the spectrum with three component curves (see Figure S2 in the Supporting Information) and calculating the relative peak areas. The results of these calculations are presented in Figure 4(e). Accordingly, the relative high contribution of Cu^{2+} (~59 %) and Cu^{3+} (~34 %) species in all XPS spectra implied that the Cu is present in its high oxidation states while the contribution of Cu^+/Cu^0 peak was only ~7 %. The contribution from each Cu state was similar for all as-synthesized materials, independent of the preparation procedure. These results together with XRD analysis confirm successful incorporation of CuO_x species within the structure of the Zr-SBA-15 supports for both *Inf* and *EIWI* methods. After the reduction, the main Cu XPS peak was observed to shift to lower binding energies for all the samples (Figure 4(d)) indicating an increase in the reduced state of the Cu NPs. The relative contents of the Cu oxidation states after the reduction were extracted from the Cu 2p XPS spectra (Figure 4(d)) and presented in Figure 4(f). It is observed that the degree of reduction depended on the silica precursor. For both *SMS* samples, 60% of the Cu NPs (within the near surface sampling volume of XPS) displayed Cu^+/Cu^0 as the oxidation state and the rest was Cu^{2+} after reduction. For *TEOS* samples, the oxidation states of 40% of the NPs were Cu^+/Cu^0 and the remaining was in higher oxidation

form. This demonstrates that a more efficient reduction was achieved for *SMS* compared to *TEOS* samples, which indicates different surface reactivity of the Cu NPs depending on the support. The lower reducing degree of Cu in the *TEOS* samples suggest a stronger interaction between the Cu NPs and the [TEOS] support compared to [SMS] support[57,58].

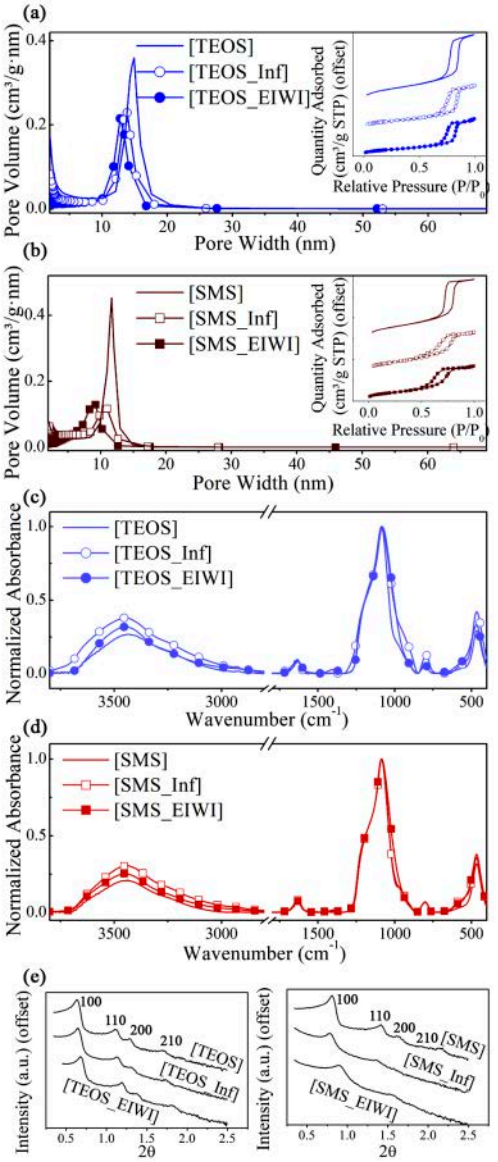

Figure 3. Pore size distributions and isotherms **(a,b)**, FTIR spectra **(c,d),** SAXRD diffractograms **(e)** of the materials.

Figure 6 summarizes the CO_2 conversion efficiency of as-synthesized Cu-Zr-SBA-15. The catalytic tests reveal that the main products from the CO_2 hydrogenation were methanol and DME. GC-MS showed the existence of other hydrocarbons and alcohols such as propane, butane, methoxy ethane and methyl formate where each one contributed with less than 0.05 % to the total conversion. These compounds are regarded as impurities in the final gas mixture. The chromatograms obtained by the flame ionization detector (FID) in GC are presented in Figure S3 in the Supporting Information.

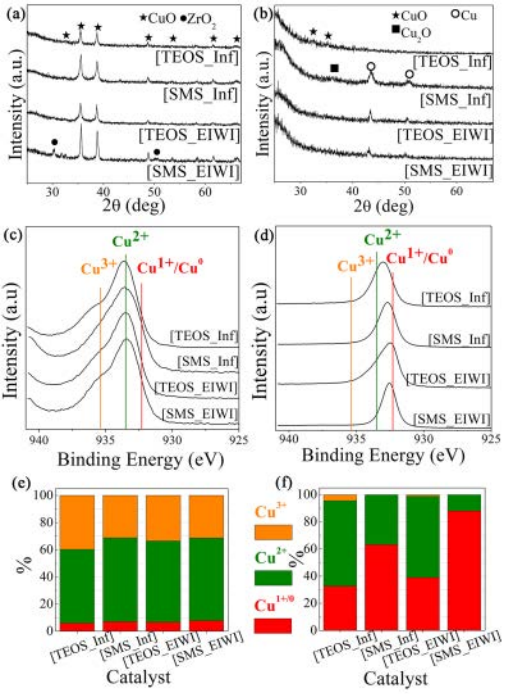

Figure 4. XRD diffractograms **(a-b)**, Cu 2p core-level spectra **(c-d)** and the Cu oxidation states at the very thin surface **(e-f)** of the as-synthesized **(a, c and e)** and reduced **(b, d and f)** catalysts.

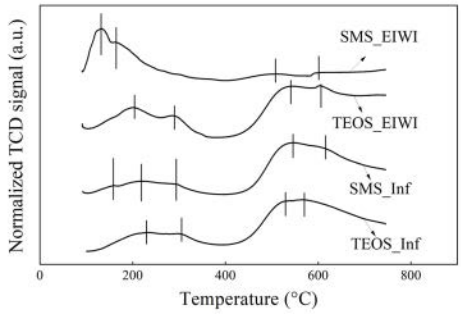

Figure 5. NH_3-TPD profiles of the catalysts with horizontal offset.

NH_3-TPD profiles of the materials (Figure 5) reveal six distinct peaks distributed in three temperature ranges. The appearance of the peaks is due to NH_3 desorption from acid sites that have different strength. The peak positions represent the strength of this acid

sites whereas the intensities reflect the concentration of that specific acid site on the catalyst surface.

The two peaks between 500-600 °C (HT) indicate the presence of strong acid sites, while the ones observed between 200-300 °C (MT) and 100-200 °C (LT) are attributed to the presence of medium and weak acid sites, respectively[59,60]. All the Cu loaded catalysts, with the exception of SMS_EIWI, exhibit a large amount of strong acid sites, which is seen by the strong intensity of the HT peaks. This is in contrast to the SMS_EIWI sample which reveals the unique presence of only weak acid sites by displaying just LT peaks. This suggests a strong influence on the catalytic activity by the medium and strong acid sites since the CO_2 conversion of SMS_EIWI is very low. The MT peaks of TEOS_Inf appear at a higher temperature than the corresponding peaks of SMS_Inf and TEOS_EIWI, revealing a higher strength for the medium acid sites of TEOS_Inf. The strong acid sites for TEOS_EIWI and SMS_Inf have higher strength compared to TEOS_Inf.

The intensity of the peaks (area under the graph) of the NH_3-TPD experiment computed for two temperature ranges (100-400 and 400-750 °C) are presented in Table 2. Accordingly, TEOS supports display a higher total intensity compared to SMS supports for the same Cu loading method indicating a higher number of acid sites. The intensity between 400-750 °C is similar between TEOS_Inf, SMS_Inf and TEOS_EIWI, which means that all these samples have similar concentration of strong acid sites. The concentration of medium acid sites is promoted by the EIWI method.

Table 1. Intensities of the NH_3-TPD curves

Sample Name	Intensity (100-400 °C)	Intensity (400-750 °C)
[TEOS_Inf]	67.1	236.3
[SMS_Inf]	41.4	211.2
[TEOS_EIWI]	91.7	242.3
[SMS_EIWI]	107	41.7

Figure 6 shows that both CO_2 conversion efficiency and product selectivity are strongly affected by the synthesis methods of the nanoassembly. For catalysts prepared via the *Inf* method, the one having TEOS as the silica precursor exhibits up to 15% CO_2-conversion, which is nearly twice the conversion obtained for catalysts prepared with SMS (~9%). A similar trend can also be seen for catalysts prepared by *EIWI*, i.e. low catalytic activity (0.4%) for [SMS_EIWI] compared to ~6.5% for [TEOS_EIWI]. Also catalysts synthesized by *EIWI* demonstrated a higher selectivity for methanol formation during the CO_2 conversion, while catalysts fabricated via *Inf* produced more DME.

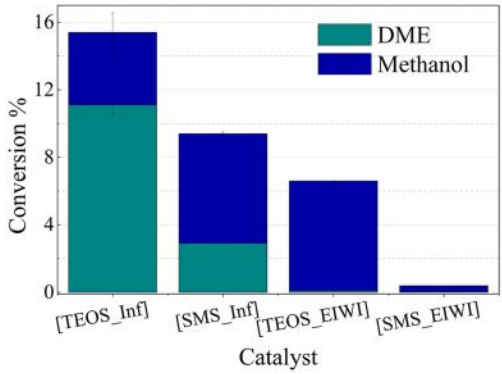

Figure 6. CO_2 conversion to methanol and DME for the prepared catalysts.

The chemical reactions which take place on the catalyst surface during CO_2 hydrogenation were investigated by DRIFTS (Figure 7). [TEOS_Inf] and [SMS_Inf] show a DME peak at 2890 cm^{-1} for the $2\delta(CH_3)$ vibrational mode[61]. This peak is not present in the spectra from [TEOS_EIWI] and [SMS_EIWI] (Figure 7), which corresponds well with the conversion results (Figure 6). Comparing the DME peak intensity relative to the methoxy peak, the amount of DME relative to methanol is higher for [TEOS_Inf] than for [SMS_Inf], This is also in good agreement with the conversion results (Figure 6). The surface reactions on the [TEOS_EIWI] catalyst were the most rapid ones, indicating fast formation of methanol. [TEOS_Inf] showed a more gradual conversion (Figure 7) indicating slower synthesis of DME compared to methanol. Methane was detected at 3015 cm^{-1} (Figure 7) but there was no trace of methane in the GC-MS measurements. The ratio of the methane peak at 3015 cm^{-1} to the methoxy peak at 2854 cm^{-1} is considerably higher in [SMS_Inf] and [SMS_EIWI] than in the TEOS samples. This indicates that when the catalyst is based on SMS, a higher concentration of surface methane is formed. All the other peaks appearing in Figure 7 correspond to the impurities detected by GC-MS and are listed in Table S1 in the Supporting Information.

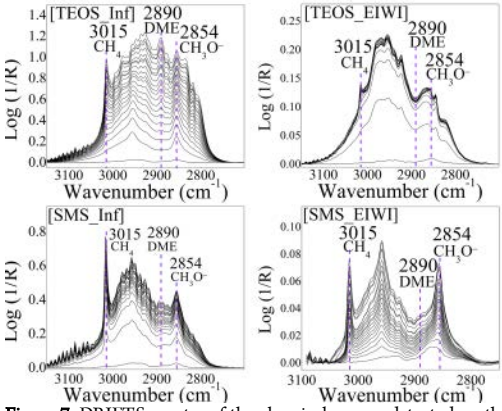

Figure 7. DRIFTS spectra of the chemical groups detected on the catalyst surface during the CO_2 hydrogenation reaction. Each line represents 8 hours progress from t=0 h to t=120 h.

To investigate the phase changes of the Cu NPs upon CO_2 hydrogenation, all catalysts were re-analyzed by XRD and XPS. Figure 8(a) represents the X-ray diffractograms of the catalysts after the CO_2 conversion. It is noted that the Cu oxidation levels change in all the nanoassemblies after the reaction. [TEOS_Inf] shows a weak CuO peak similar to its reduced form (Figure 4(b)) while [SMS_Inf] and [TEOS_EIWI] both display Cu_2O and Cu metal. [SMS_EIWI] exhibits a very similar XRD pattern as the one recorded from the as-synthesized material, i.e. peaks attributed to CuO and ZrO_2 (Figure 4(a) and 7(c)). This indicates complete reversibility of the reduction process for [SMS_EIWI], which was not the case for the other samples. In addition, crystalline ZrC (PDF#03-065-9888) appeared on [SMS_Inf] and [TEOS_EIWI] after the reaction (Figure 8(a)).

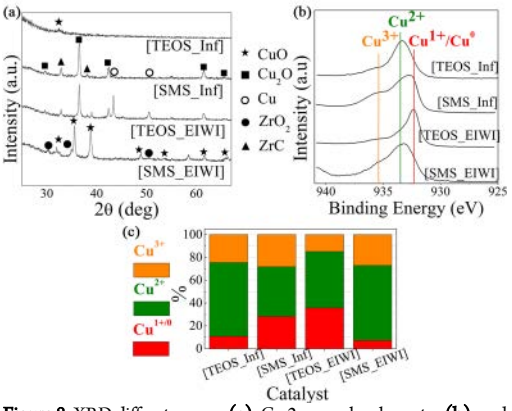

Figure 8. XRD diffractograms **(a)**, Cu 2p core-level spectra **(b),** and Cu contents **(c)** of the catalysts after reaction.

The Cu $2p_{3/2}$ core-level spectra of the used catalysts are presented in Figure 8(b) and fractions of the different Cu oxidation states are shown in Figure 8(c). After the CO_2 hydrogenation, the chemical environment of Cu includes all its oxidation states: Cu^{+3}, Cu^{2+} and Cu^{+}/Cu^{0}, where Cu^{2+} is the most dominant. This is similar to the as-synthesized catalysts (Figure 4(c)), even though fractions vary. The only exception is [SMS_EIWI], which shows the same Cu oxidation state fraction as for the as-synthesized, which is in accord with the XRD results in Figure 8(a).

Comparing the fractions of the Cu oxidation states in the as-synthesized and reduced samples (Figure 4 (d,f)) with the used catalysts (Figure 8(b,c)) yields Cu NPs in the *SMS* samples re-oxidize during (or after) the CO_2 hydrogenation to a higher degree compared to those in *TEOS* samples. This again indicates a higher surface reactivity of Cu NPs on *SMS* supports compared to *TEOS* supports. We attribute this to a stronger interaction between TEOS supports and the Cu NPs, similar to what was seen for reduced samples[57,58]. When comparing *TEOS* supports, Cu NPs in [TEOS_Inf] re-oxidize to a higher extent than Cu NPs in [TEOS_EIWI]. This suggests that DME formation contributes to the catalyst's surface oxidation, since [TEOS_Inf] produces DME while [TEOS_EIWI] is selective to methanol.

A ZrO_2 phase as well as indications of Zr^0 metal were also observed in the used catalysts (Figure S1 in the Supporting Information).

4. DISCUSSION

In this work, different chemical states of Cu loaded Zr-SBA-15 supports and their effects on the catalytic activity during CO_2 hydrogenation were studied. The different chemical states were obtained by changing the silica precursor in the Zr-SBA-15 synthesis and the technique for loading Cu NPs in the supports. This is addressed in the first part of the discussions. In the second part, the effects of these alterations on the catalytic activity and selectivity in terms of CO_2 conversion into methanol and DME, are discussed.

4.1. Synthesis of Cu-Zr-SBA-15

Both TEOS and SMS silica precursors yield a Zr-SBA-15 material with hexagonally ordered pore structure and a similar Zr content. A morphological difference was observed. [SMS] has a larger particle cross-sectional diameter than [TEOS]. In addition, the pore size, microporosity and specific surface area (SSA) are larger for [TEOS].

The difference in the particle width is attributed to the lower PEO solubility of the micelle in the synthesis solution of [SMS]. The material formation occurs by silica oligomers attaching to the PEO corona of the micelles[62]. During the hydrolysis of *SMS*, NaOH is released as silica is formed, Eq.(5,6)[63,64].

$$Na_2SiO_3 + H_2O \rightarrow H_2SiO_3 + 2NaOH \quad (5)$$

$$H_2SiO_3 + H_2O \rightarrow Si(OH)_4 \quad (6)$$

$$2F^- + 2NaOH \rightarrow 2NaF + H_2O + \frac{1}{2}O_2 \quad (7)$$

Formation of NaOH does not only reduce the acidity but it can also interact with F^- ions in the solution (Eq. (7)). A decreased F^- concentration results in an increased solubility of the PEO-chains. As a consequence, the elongated PEO-chains cause more micelles to aggregate due to entanglement[63,65], which causes a widening of the particles before the mesoporous structure of [SMS] is locked. Since Na is not part of the [TEOS] synthesis, less PEO-chain entanglement occurs and the formed particles are more narrow.

The microporosity is less for [SMS] than [TEOS] samples. Microporosity is typically induced by PEO-chains that remain penetrated in the silica walls during condensation[66]. Pre-hydrolysis of SMS results in pre-formed silica clusters and as this silica precursor is added into the synthesis the silica framework forms rapidly[67]. As a result, the PEO chains cannot penetrate into the silica wall as efficiently as in case of [TEOS]. A low level of microporosity causes a lower SSA of [SMS] compared to [TEOS].

The pore size is larger for [TEOS] compared to [SMS] because *TEOS* may act as a swelling agent in the synthesis solution prior to its hydrolysis. Not-yet hydrolyzed *TEOS*, due to its immiscibility in water, penetrates into the hydrophobic core of the micelles and results in larger pores[68]. *SMS* is miscible in water and does not act as a swelling agent. Additionally, expansion of the micelles by heptane occurs to a lower degree because of the rapid formation of [SMS].

Zr bonds stronger to the silica framework in [TEOS] compared to [SMS]. The weaker Zr attachment to [SMS] causes a larger loss of Zr in [SMS_Inf] than [TEOS_Inf] during Cu-loading. *Inf* is a method that previously has been shown to decrease the Zr content in a Zr-SBA-15 material due to high elution strength of the used toluene[37]. As a consequence, ZrO_2 detached from [SMS_Inf] can form ZrO_2 clusters and due to their low interaction with the SiO_2 framework they can be reduced to Zr metal. The strong bonding of Zr to [TEOS_Inf] prevents such reduction. This is further

corroborated by the observation of ZrO_2-clusters with long-range order in [SMS_EIWI] and not in [TEOS_EIWI]. The reason for the poor Zr-interaction with the SiO_2 framework of [SMS] can be traced back to the pre-hydrolysis of the SMS precursor. During the pre-hydrolysis, small silica clusters are formed, which reduces the Zr – Si interaction, and also causes a faster material formation which compromise the Zr incorporation.

Cu NPs were grown in the Zr-SBA-15 supports without causing modification of the hexagonal pore order. The presence of Cu NPs results in a decreased SSA of the mesoporous material as they block some of the pores. Despite this, the number of -OH groups increases by attachment to the not fully oxidized Cu NPs. However, between the Cu loading methods the number of -OH groups were higher for *Inf* compared to *EIWI* even though their Cu oxidation state fractions were similar. This is an effect of the overall higher SSA of *Inf* compared to *EIWI*.

The wall thickness of the mesoporous supports increases when Cu loaded due to incorporation of Cu-atoms in the walls. It has been shown that adsorbed atoms on a surface can make their way into the body by displacing existing atoms in their way such that the displaced atoms now exist on the surface[69–72]. This leads to decreased pore size and increased wall thickness. This phenomenon can also result in unexpected oxidations states, such as Cu^{3+} as the local chemistry surrounding the embedded atom affects the oxidation state. The higher level of Cu diffusion into the walls of [TEOS] is an indication of a stronger interaction between Cu NPs and the [TEOS] support, i.e. a stronger interface between the particle and the support resulting in a higher resistance against a reducing environment[57,58]. As a result of the difference in affinities between particle and support and possible Cu diffusion into the walls, *TEOS* materials are reduced and re-oxidized (after the CO_2 conversion) to a less extent than *SMS* materials. The reason for the different affinity is not clear, but likely associated with the acidity of the support, as *TEOS* showed a higher surface acidity than *SMS*. Similarly, Cu atomic diffusion into the walls was slightly more favored for *Inf* compared to *EIWI*. This is in a good agreement with the fact that SSA for *Inf* samples are higher than *EIWI* due to better distribution of Cu on the support causing less pore plugs.

4.2. Catalytic activity

The good adhesion between the [TEOS] support and the Cu NPs have resulted in a more efficient collective CO_2 conversion into methanol and DME compared to [SMS]-based assemblies. The selectivity for methanol and DME was also different for [TEOS] and [SMS]-based catalysts due to their distinct surface acidity. *TEOS* materials have shown to exhibit a higher amount of acid sites with a higher strength compared to *SMS* materials yielding DME, which is known to from by acid catalysts[73]. The different surface acidity is a consequence of the different synthesis solution environment of [SMS] compared to *TEOS*. In the SMS synthesis, NaOH is a side product of [SMS] and more Zr is lost during Cu loading[37,74,75] compared to *TEOS*. The high concentration of surface methane groups on the *SMS* catalysts is also attributed to its low acidity. A high acidity causes methane decomposition[76] while improved catalyst basicity has been shown to increase the methane yield[77,78]. In addition, the formed methane can poison the catalyst and cause lower catalytic conversion rates.

As for the Cu loading methods, the *Inf* method tends to promote higher CO_2 conversion to DME whereas *EIWI* produced catalysts are highly selective for methanol formation. One reason for this difference in terms of catalytic selectivity can be the Zr content of the catalysts which is higher for *EIWI* compared to *Inf*. Zr contributes to the electron/oxygen mobility of Cu[79], and thus provides higher collective amount of weak and medium acid sites to the *EIWI* catalysts although they exhibit lower strength than the corresponding sites in *Inf*. The weak acid sites do not impact the CO_2 conversion as evident from the low catalytic activity of SMS_EIWI. Instead, the difference in activity and selectivity of the catalysts mainly depends on the amount and strength of medium and strong acid sites.

TEOS_EIWI has a high total concentration of acid sites and yields a high selectivity for methanol. This is a result of a sufficient amount of H attached to the catalyst sur-face to react with the surface methoxy groups and form methanol. In case of TEOS_Inf, a higher strength of the medium acid sites was observed compared to TEOS_EIWI. We note that as the strength of the medium acid sites increases the selectivity of the catalyst for DME formation increases. This is in accord with previous studies showing that DME is preferentially catalyzed at medium strength acid sites[59]. We then infer that a higher strength of the medium strength acid sites favors methoxy attachment caused by the increased attraction between the positively charged surface acid sites and the negatively charged methoxy groups. The improved DME selectivity is then caused by a higher sur-face methoxy concentration, which enhances the probability of neighboring methoxy groups to form DME (Figure 9).

The relevance of acid site strength to the methoxy affinity is also corroborated by the XPS results from the reduced samples. Comparison of the same Zr-SBA-15 support shows that higher DME selectivity is caused by a less reduced sample, e.g. TEOS_Inf versus TEOS_EIWI. Catalysts with less reduction can demonstrate a higher concentration of surface Cu-O-H^+ acid sites which donate protons and thus can couple with the negatively charged methoxy surface groups. On the other hand, more reduced catalysts would involve more unsaturated cationic acid sites (such as Cu^+) which would strongly attract single-electron hydrogen.

[TEOS_Inf] is more re-oxidized compared to [TEOS_EIWI] after the CO_2 hydrogenation reaction This is due to the DME formation on the catalyst surface of [TEOS_Inf] which leads to re-oxidation of the reduced Cu species. It has previously been proposed[80] that DME can be converted directly from methoxy without going through the methanol formation step, which causes excess oxygen atoms to remain on the catalyst surface with a mechanism shown in Eq. (8) and Figure 9. Such reaction promotes re-oxidation of the reduced catalyst.

$$CH_3O^- + CH_3O^- \rightarrow CH_3OCH_3 + O^{2-} \quad (8)$$

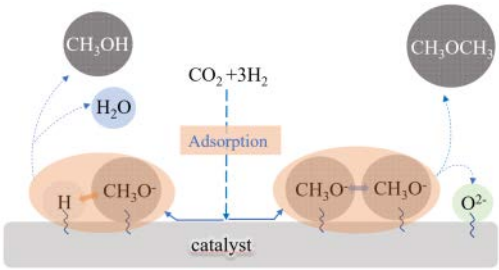

Figure 9. Catalyst surface reactions during CO_2 hydrogenation.

5. CONCLUSIONS

Zr-SBA-15 was synthesized using two different silica precursors: TEOS and SMS, and was loaded with Cu using two different methods (*Inf* and *EIWI*). TEOS yields materials with larger pores, specific surface area, and microporosity compared to SMS whereas [SMS] particles are wider compared to [TEOS] particles. Cu NPs grown in the pores of the supports cause a reduction in the specific surface area and pore size, as well as wall thickness increase due to Cu atomic diffusion into the walls. All the nano-assemblies show catalytic activity in CO_2 hydrogenation but with different level of activity and selectivity due to their different chemical states. *SMS* samples exhibit lower catalytic activity compared to *TEOS* samples due to a lower Zr content, lower acid site content, and formation of methane. The interaction of the Cu NPs with the support surface affects the reducibility and thus the performance in terms of catalyzing CO_2 hydrogenation. The *Inf* method yields DME and methanol with higher selectivity for DME whereas *EIWI* selectively produces methanol. DME formation from two methoxy molecules on the catalyst surface causes re-oxidation of the Cu and points out the possibility of direct DME synthesis, bypassing the methanol formation step.

ASSOCIATED CONTENT

Supporting Information. Cu peak fittings of XRD results, Cu 3p core-level spectra fittings and Cu 3p and Zr 3d core-level comparative spectra for each sample, FID chromatograms, and Drifts peak identification table are presented in the Supporting Information (SI).

AUTHOR INFORMATION

Corresponding Author

* E-mail: aylin.atakan@liu.se

Notes

The authors declare no competing financial interest.

ACKNOWLEDGMENT

This work was financially supported by EU's Erasmus-Mundus program (The European School of Materials - Doctoral Programme – DocMASE), The Swedish Government Strategic Research Area in Materials Science on Functional Materials at Linköping University (Faculty Grant SFO-Mat-LiU # 2009-00971), The Swedish research council (Dnr 2015-00624), the competence center FunMat-II that is financially supported by Vinnova (grant no 2016-05156) and Knut and Alice Wallenbergs Foundation through the project: Designed nanoparticles through pulsed plasma (Contract KAW 2012.0083).

REFERENCES

[1] T.J. Blasing, Recent Greenhouse Gas Concentrations., (2009) 1–5. doi:10.3334/CDIAC/atg.032.

[2] W. Wang, S. Wang, X. Ma, J. Gong, Recent advances in catalytic hydrogenation of carbon dioxide, Chem Soc Rev. 40 (2011) 3703–3727. doi:10.1039/c1cs15008a.

[3] J.G. van Bennekom, R.H. Venderbosch, J.G.M. Winkelman, E. Wilbers, D. Assink, K.P.J. Lemmens, H.J. Heeres, Methanol synthesis beyond chemical equilibrium, Chem. Eng. Sci. 87 (2013) 204–208. doi:10.1016/j.ces.2012.10.013.

[4] K.A. Ali, A. Zuhairi, A.R. Mohamed, Recent development in catalytic technologies for methanol synthesis from renewable sources : A critical review, Renew. Sustain. Energy Rev. 44 (2015) 508–518. doi:10.1016/j.rser.2015.01.010.

[5] J.A. Kosek, C.C. Cropley, A.B. LaConti, Membrane-electrode assembly for a direct methanol fuel cell, (1996). https://www.google.com/patents/US5523177.

[6] H. Arakawa, Advances in Chemical Conversions for Mitigating Carbon Dioxide, Proceedings of the Fourth International Conference on Carbon Dioxide Utilization, Elsevier, 1998. doi:10.1016/S0167-2991(98)80723-4.

[7] S.G. Jadhav, P.D. Vaidya, B.M. Bhanage, J.B. Joshi, Catalytic carbon dioxide hydrogenation to methanol: A review of recent studies, Chem. Eng. Res. Des. 92 (2014) 2557–2567. doi:10.1016/j.cherd.2014.03.005.

[8] I. a Fisher, A.T. Bell, In-SituInfrared Study of Methanol Synthesis from H2/CO2over Cu/SiO2and Cu/ZrO2/SiO2, J. Catal. 172 (1997) 222–237. doi:10.1006/jcat.1997.1870.

[9] M. Madej-Lachowska, A. Kasprzyk-Mrzyk, H. Moroz, a I. Lachowski, H. Wyzgol, Methanol Synthesis from Carbon Dioxide and Hydrogen over CuO / ZnO / ZrO 2 promoted catalysts, Chemik. 68 (2014) 61–68.

[10] T. Tsoncheva, V. Dal Santo, A. Gallo, N. Scotti, M. Dimitrov, D. Kovacheva, Structure and catalytic activity of hosted in mesoporous silicas copper species: Effect of preparation procedure and support pore topology, Appl. Catal. A Gen. 406 (2011) 13–21. doi:10.1016/j.apcata.2011.07.034.

[11] P. Munnik, M. Wolters, A. Gabrielsson, S.D. Pollington, G. Headdock, J.H. Bitter, P.E. de Jongh, K.P. de Jong, Copper Nitrate Redispersion To Arrive at Highly Active Silica-Supported Copper Catalysts, J. Phys. Chem. C. 115 (2011) 14698–14706. doi:10.1021/jp111778g.

[12] X.-M. Liu, G.Q. Lu, Z.-F. Yan, J. Beltramini, Recent Advances in Catalysts for Methanol Synthesis via Hydrogenation of CO and CO2, Ind. Eng. Chem. Res. 42 (2003) 6518–6530. doi:10.1021/ie020979s.

[13] Z. Alothman, A Review: Fundamental Aspects of Silicate Mesoporous Materials, Materials (Basel). 5 (2012) 2874–2902. doi:10.3390/ma5122874.

[14] P. Biswas, P. Narayanasarma, C.M. Kotikalapudi, A.K. Dalai, J. Adjaye, Characterization and Activity of ZrO2Doped SBA-15 Supported NiMo Catalysts for HDS and HDN of Bitumen Derived Heavy Gas Oil, Ind. Eng. Chem. Res. 50 (2011) 7882–7895. doi:10.1021/ie102429j.

[15] N. Masoud, L. Delannoy, H. Schaink, A. van der Eerden, J.W. de Rijk, T.A.G. Silva, D. Banerjee, J.D. Meeldijk, K.P. de Jong, C. Louis, P.E. de Jongh, Superior Stability of Au/SiO 2 Compared to Au/TiO 2 Catalysts for the Selective Hydrogenation of Butadiene, ACS Catal. 7 (2017) 5594–5603. doi:10.1021/acscatal.7b01424.

[16] T. Witoon, T. Numpilai, T. Phongamwong, W. Donphai, C. Boonyuen, C. Warakulwit, M. Chareonpanich, J. Limtrakul, Enhanced activity, selectivity and stability of a CuO-ZnO-ZrO 2 catalyst by adding graphene oxide for CO 2 hydrogenation to methanol, Chem. Eng. J. 334 (2018) 1781–1791. doi:10.1016/j.cej.2017.11.117.

[17] T. Phongamwong, U. Chantaprasertporn, T. Witoon, T. Numpilai, Y. Poo-arporn, W. Limphirat, W. Donphai, P. Dittanet, M. Chareonpanich, J. Limtrakul, CO 2 hydrogenation to methanol over CuO–ZnO–ZrO 2 –SiO 2 catalysts: Effects of SiO 2 contents, Chem. Eng. J. 316 (2017) 692–703. doi:10.1016/j.cej.2017.02.010.

[18] V. Mamaeva, C. Sahlgren, M. Lindén, Mesoporous silica nanoparticles in medicine--recent advances., Adv. Drug Deliv. Rev. 65 (2013) 689–702. doi:10.1016/j.addr.2012.07.018.

[19] V. Meynen, P. Cool, E.F. Vansant, Verified syntheses of mesoporous materials, Microporous Mesoporous Mater. 125 (2009) 170–223.

doi:10.1016/j.micromeso.2009.03.046.

[20] S. Wang, Ordered mesoporous materials for drug delivery, Microporous Mesoporous Mater. 117 (2009) 1–9. doi:10.1016/j.micromeso.2008.07.002.

[21] D. Zhao, J. Feng, Q. Huo, N. Melosh, G.H. Fredrickson, B.F. Chmelka, G.D. Stucky, Triblock Copolymer Syntheses of Mesoporous Silica with Periodic 50 to 300 Angstrom Pores, Science (80-.). 279 (1998) 548–552. doi:10.1126/science.279.5350.548.

[22] D.M. Do, S. Jaenicke, G.-K. Chuah, Mesoporous Zr-SBA-15 as a green solid acid catalyst for the Prins reaction, Catal. Sci. Technol. 2 (2012) 1417. doi:10.1039/c2cy20084h.

[23] M. Moritz, M. Geszke-Moritz, Mesoporous materials as multifunctional tools in biosciences: Principles and applications, Mater. Sci. Eng. C. 49 (2014) 114–151. doi:10.1016/j.msec.2014.12.079.

[24] H.T. Tsai, J.M. Córdoba, E.M. Johansson, M.A. Ballem, M. Odén, Silica SBA-15 Template Assisted Synthesis of Ultrasmall and Homogeneously Sized Copper Nanoparticles, J. Nanosci. Nanotechnol. 11 (2011) 3493–3498. doi:10.1166/jnn.2011.3609.

[25] N. Rahmat, F. Hamzah, N. Sahiron, M. Mazlan, M.M. Zahari, Sodium silicate as source of silica for synthesis of mesoporous SBA-15, IOP Conf. Ser. Mater. Sci. Eng. 133 (2016) 12011. doi:10.1088/1757-899X/133/1/012011.

[26] C. Zhao, L. Liu, Q. Zhang, J. Wang, Y. Li, Photocatalytic conversion of CO2 and H2O to fuels by nanostructured Ce–TiO2/SBA-15 composites, Catal. Sci. Technol. (2012) 2558–2568. doi:10.1039/c2cy20346d.

[27] V. Degirmenci, D. Uner, B. Cinlar, B.H. Shanks, A. Yilmaz, R.A. Santen, E.J.M. Hensen, Sulfated Zirconia Modified SBA-15 Catalysts for Cellobiose Hydrolysis, Catal. Letters. 141 (2010) 33–42. doi:10.1007/s10562-010-0466-1.

[28] C. Ochoa-Hernández, Y. Yang, P. Pizarro, V.A. de la Peña O'Shea, J.M. Coronado, D.P. Serrano, Hydrocarbons production through hydrotreating of methyl esters over Ni and Co supported on SBA-15 and Al-SBA-15, Catal. Today. 210 (2013) 81–88. doi:http://dx.doi.org/10.1016/j.cattod.2012.12.002.

[29] M. Moritz, M. Łaniecki, SBA-15 mesoporous material modified with APTES as the carrier for 2-(3-benzoylphenyl)propionic acid, Appl. Surf. Sci. 258 (2012) 7523–7529. doi:10.1016/j.apsusc.2012.04.076.

[30] T.X. Bui, V.H. Pham, S.T. Le, H. Choi, Adsorption of pharmaceuticals onto trimethylsilylated mesoporous SBA-15., J. Hazard. Mater. 254–255 (2013) 345–53. doi:10.1016/j.jhazmat.2013.04.003.

[31] P.F. Fulvio, S. Pikus, M. Jaroniec, Short-time synthesis of SBA-15 using various silica sources, J. Colloid Interface Sci. 287 (2005) 717–720. doi:10.1016/j.jcis.2005.02.045.

[32] J.M. Kim, G.D. Stucky, Synthesis of highly ordered mesoporous silica materials using sodium silicate and amphiphilic block copolymers, Chem. Commun. (2000) 1159–1160. doi:10.1039/b002362k.

[33] T. Tsoncheva, E. Sarkadi-Priboczki, Copper and chromium modified SBA-15: 11C-radiolabeling catalytic study, Microporous Mesoporous Mater. 148 (2012) 1–7. doi:10.1016/j.micromeso.2011.07.013.

[34] J. Zhu, T. Wang, X. Xu, P. Xiao, J. Li, Pt nanoparticles supported on SBA-15: Synthesis, characterization and applications in heterogeneous catalysis, Appl. Catal. B Environ. 130–131 (2013) 197–217. doi:10.1016/j.apcatb.2012.11.005.

[35] E. Escalera, M.A. Ballem, J.M. Córdoba, M.-L. Antti, M. Odén, Synthesis of homogeneously dispersed cobalt nanoparticles in the pores of functionalized SBA-15 silica, Powder Technol. 221 (2012) 359–364. doi:10.1016/j.powtec.2012.01.025.

[36] S. Ajaikumar, M. Golets, W. Larsson, a. Shchukarev, K. Kordas, a.-R. Leino, J.-P. Mikkola, Effective dispersion of Au and Au–M (M=Co, Ni, Cu and Zn) bimetallic nanoparticles over TiO2 grafted SBA-15: Their catalytic activity on dehydroisomerization of α-pinene, Microporous Mesoporous Mater. 173 (2013) 99–111. doi:10.1016/j.micromeso.2013.02.015.

[37] A. Atakan, P. Mäkie, F. Söderlind, J. Keraudy, E.M. Björk, M. Odén, Synthesis of a Cu-infiltrated Zr-doped SBA-15 catalyst for CO 2 hydrogenation into methanol and dimethyl ether, Phys. Chem. Chem. Phys. 19 (2017) 19139–19149. doi:10.1039/C7CP03037A.

[38] S. Brunauer, P.H. Emmett, E. Teller, Adsorption of Gases in Multimolecular Layers, J. Am. Chem. Soc. 60 (1938) 309–319. doi:10.1021/ja01269a023.

[39] M. Jaroniec, L.A. Solovyov, Improvement of the Kruk–Jaroniec–Sayari Method for Pore Size Analysis of Ordered Silicas with Cylindrical Mesopores, Langmuir. 22 (2006) 6757–6760. doi:10.1021/la0609571.

[40] B. Lippens, Studies on pore systems in catalysts V. The t method, J. Catal. 4 (1965) 319–323. doi:10.1016/0021-9517(65)90307-6.

[41] K.S.W. Sing, Reporting physisorption data for gas/solid systems with special reference to the determination of surface area and porosity (Provisional), Pure Appl. Chem. 54 (1982) 2201–2218. doi:10.1351/pac198254112201.

[42] T.M. Eggenhuisen, J. Zečević, H. Talsma, K.P. De Jong, P.E. De Jongh, Quantitative assessment of pore blockage in supported catalysts: Comparing differential scanning calorimetry and physisorption, J. Phys. Chem. C. 116 (2012) 7480–7490. doi:10.1021/jp300604b.

[43] M. Thommes, K. Kaneko, A. V. Neimark, J.P. Olivier, F. Rodriguez-Reinoso, J. Rouquerol, K.S.W. Sing, Physisorption of gases, with special reference to the evaluation of surface area and pore size distribution (IUPAC Technical Report), Pure Appl. Chem. 87 (2015) 1051–1069. doi:10.1515/pac-2014-1117.

[44] X. Wang, L. Chen, M. Shang, F. Lin, J. Hu, R.M. Richards, Nanoscale gold intercalated into mesoporous silica as a highly active and robust catalyst, Nanotechnology. 23 (2012) 294010. doi:10.1088/0957-4484/23/29/294010.

[45] M.A. Salvador, J. Canales-Vázquez, P. Ferreira, F.M. Figueiredo, Characterization of Mesoporous Zirconium and Cerium Oxides by Transmission Electron Microscopy, Microsc. Microanal. 18 (2012) 81–82.

[46] L.F. Chen, X.L. Zhou, L.E. Noreña, J. a. Wang, J. Navarrete, P. Salas, a. Montoya, P. Del Angel, M.E. Llanos, Comparative studies of Zr-based MCM-41 and MCM-48 mesoporous molecular sieves: Synthesis and physicochemical properties, Appl. Surf. Sci. 253 (2006) 2443–2451. doi:10.1016/j.apsusc.2006.04.064.

[47] Y. Borodko, J.W.A. Iii, G.E. Marti, H. Song, K. Niesz, Structure Sensitivity of Vibrational Spectra of Mesoporous Silica SBA-15 and Pt / SBA-15, J. Phys. Chem. B. 109 (2005) 17386–17390.

[48] P. Innocenzi, Infrared spectroscopy of sol-gel derived silica-based films: A spectra-microstructure overview, J. Non. Cryst. Solids. 316 (2003) 309–319. doi:10.1016/S0022-3093(02)01637-X.

[49] M. Petrescu, R.A. Mitran, A.M. Luchian, C. Matei, D. Berger, Mesoporous ceria-silica composites as carriers for doxycycline, UPB Sci. Bull. Ser. B Chem. Mater. Sci. 77 (2015) 13–24.

[50] T.S. Tsoncheva, I.G. Genova, N. Scotti, M.D. Dimitrov, A. Gallo, Silica supported copper and cobalt oxide catalysts for methanol decomposition : Effect of preparation procedure, Bulg. Chem. Commun. 47 (2015) 283–290.

[51] V. Prakash, R.K. Diwan, U.K. Niyogi, Characterization of synthesized copper oxide nanopowders and their use in nanofluids for enhancement of thermal conductivity, Indian J. Pure Appl. Phys. 53 (2015) 753–758.

[52] S. Poulston, P.M. Parlett, P. Stone, M. Bowker, Surface Oxidation and Reduction of CuO and Cu2O Studied Using XPS and XAES, Surf. Interface Anal. 24 (1996) 811–820. doi:10.1002/(SICI)1096-

9918(199611)24:12<811::AID-SIA191>3.0.CO;2-Z.

[53] C.C. Chusuei, M.A. Brookshier, D.W. Goodman, Correlation of relative X-ray photoelectron spectroscopy shake-up intensity with CuO particle size, Langmuir. 15 (1999) 2806–2808. doi:10.1021/la9815446.

[54] J.M. Lim, T. Hwang, M.S. Park, M. Cho, K. Cho, Design of a p-type electrode for enhancing electronic conduction in high-Mn, Li-rich oxides, Chem. Mater. 28 (2016) 8201–8209. doi:10.1021/acs.chemmater.6b03032.

[55] N. Padmavathy, R. Vijayaraghavan, G.U. Kulkarni, Solution based rapid synthesis of AgCuO $_2$ at room temperature, RSC Adv. 4 (2014) 62746–62750. doi:10.1039/C4RA11853G.

[56] C. Wu, M. Yin, S. O'Brien, J.T. Koberstein, Quantitative Analysis of Copper Oxide Nanoparticle Composition and Structure by X-ray Photoelectron Spectroscopy, Chem. Mater. 18 (2006) 6054–6058. doi:10.1021/cm061596d.

[57] J. Zhao, H. Chen, J. Xu, J. Shen, Effect of Surface Acidic and Basic Properties of the Supported Nickel Catalysts on the Hydrogenation of Pyridine to Piperidine, J. Phys. Chem. C. 117 (2013) 10573–10580. doi:10.1021/jp402238q.

[58] W. Lin, A.A. Herzing, C.J. Kiely, I.E. Wachs, Probing Metal?Support Interactions under Oxidizing and Reducing Conditions:? In Situ Raman and Infrared Spectroscopic and Scanning Transmission Electron Microscopic?X-ray Energy-Dispersive Spectroscopic Investigation of Supported Platinum Catalysts, J. Phys. Chem. C. 112 (2008) 5942–5951. doi:10.1021/jp710591m.

[59] S. Asthana, C. Samanta, A. Bhaumik, B. Banerjee, R.K. Voolapalli, B. Saha, Direct synthesis of dimethyl ether from syngas over Cu-based catalysts: Enhanced selectivity in the presence of MgO, J. Catal. 334 (2016) 89–101. doi:10.1016/j.jcat.2015.10.020.

[60] T. Witoon, T. Permsirivanich, N. Kanjanasoontorn, C. Akkaraphataworn, A. Seubsai, K. Faungnawakij, C. Warakulwit, M. Chareonpanich, J. Limtrakul, Direct synthesis of dimethyl ether from CO 2 hydrogenation over Cu–ZnO–ZrO 2 /SO 4 2– –ZrO 2 hybrid catalysts: effects of sulfur-to-zirconia ratios, Catal. Sci. Technol. 5 (2015) 2347–2357. doi:10.1039/C4CY01568A.

[61] A. Kecskeméti, R. Barthos, F. Solymosi, Aromatization of dimethyl and diethyl ethers on Mo2C-promoted ZSM-5 catalysts, J. Catal. 258 (2008) 111–120. doi:10.1016/j.jcat.2008.06.003.

[62] E.M. Johansson, M.A. Ballem, J.M. Cordoba, M. Oden, Rapid synthesis of SBA-15 rods with variable lengths, widths, and tunable large pores, Langmuir. 27 (2011) 4994–4999. doi:10.1021/la104864d.

[63] E.M. Björk, F. Söderlind, M. Odén, Tuning the shape of mesoporous silica particles by alterations in parameter space: from rods to platelets., Langmuir. 29 (2013) 13551–61. doi:10.1021/la403201v.

[64] A. Venkateswara Rao, A. Parvathy Rao, M.M. Kulkarni, Influence of gel aging and Na2SiO3/H2O molar ratio on monolithicity and physical properties of water-glass-based aerogels dried at atmospheric pressure, J. Non. Cryst. Solids. 350 (2004) 224–229. doi:10.1016/j.jnoncrysol.2004.07.083.

[65] V. Alfredsson, H. Wennerström, The Dynamic Association Processes Leading from a Silica Precursor to a Mesoporous SBA-15 Material, Acc. Chem. Res. 48 (2015) 1891–1900. doi:10.1021/acs.accounts.5b00165.

[66] O.C. Gobin, SBA-15 Materials - Synthesis, Diffusion and Sorption Properties, 2006.

[67] E.M. Björk, P. Mäkie, L. Rogström, A. Atakan, N. Schell, M. Odén, Formation of block-copolymer-templated mesoporous silica, J. Colloid Interface Sci. 521 (2018) 183–189. doi:10.1016/j.jcis.2018.03.032.

[68] J. Liu, Q. Yang, X.S. Zhao, L. Zhang, Pore size control of mesoporous silicas from mixtures of sodium silicate and TEOS, Microporous Mesoporous Mater. 106 (2007) 62–67. doi:10.1016/j.micromeso.2007.02.045.

[69] R. Tromp, Surface diffusion: Atoms go underground, Nat. Mater. 2 (2003) 212–213. doi:10.1038/nmat869.

[70] G.L. Kellogg, P.J. Feibelman, Surface self-diffusion on Pt(001) by an atomic exchange mechanism, Phys. Rev. Lett. 64 (1990) 3143–3146. doi:10.1103/PhysRevLett.64.3143.

[71] J. Camarero, J. Ferrón, V. Cros, L. Gómez, A.L. Vázquez de Parga, J.M. Gallego, J.E. Prieto, J.J. de Miguel, R. Miranda, Atomistic Mechanism of Surfactant-Assisted Epitaxial Growth, Phys. Rev. Lett. 81 (1998) 850–853. doi:10.1103/PhysRevLett.81.850.

[72] M. Copel, M.C. Reuter, E. Kaxiras, R.M. Tromp, Surfactants in epitaxial growth, Phys. Rev. Lett. 63 (1989) 632–635. doi:10.1103/PhysRevLett.63.632.

[73] Z. Lei, Z. Zou, C. Dai, Q. Li, B. Chen, Synthesis of dimethyl ether (DME) by catalytic distillation, Chem. Eng. Sci. 66 (2011) 3195–3203. doi:10.1016/j.ces.2011.02.034.

[74] S.-Y. Chen, L.-Y. Jang, S. Cheng, Synthesis of Zr-Incorporated SBA-15 Mesoporous Materials in a Self-generated Acidic Environment, Chem. Mater. 16 (2004) 4174–4180. doi:10.1021/cm049247b.

[75] K. Szczodrowski, B. Prélot, S. Lantenois, J. Zajac, M. Lindheimer, D. Jones, A. Julbe, A. van der Lee, Effect of synthesis conditions on the pore structure and degree of heteroatom insertion in Zr-doped SBA-15 silica-based materials prepared by classical or microwave-assisted hydrothermal treatment, Microporous Mesoporous Mater. 110 (2008) 111–118. doi:10.1016/j.micromeso.2007.09.038.

[76] P. va. Beurden, On The Catalytic Aspects Of Steam Reforming Methane - A Literature Survey, Ecn. (2004) 1–27.

[77] R. Bouarab, O. Cherifi, A. Auroux, Reforming of methane by CO2 in presence of cobalt- based catalystsThis work was presented at the Green Solvents for Catalysis Meeting held in Bruchsal, Germany, 13–16th October 2002, Green Chem. 5 (2003) 209–212. doi:10.1039/b210348f.

[78] N. Wang, X. Yu, K. Shen, W. Chu, W. Qian, Synthesis, characterization and catalytic performance of MgO-coated Ni/SBA-15 catalysts for methane dry reforming to syngas and hydrogen, Int. J. Hydrogen Energy. 38 (2013) 9718–9731. doi:http://dx.doi.org/10.1016/j.ijhydene.2013.05.097.

[79] A.G. Sato, D.P. Volanti, D.M. Meira, S. Damyanova, E. Longo, J.M.C. Bueno, Effect of the ZrO2 phase on the structure and behavior of supported Cu catalysts for ethanol conversion, J. Catal. 307 (2013) 1–17. doi:10.1016/j.jcat.2013.06.022.

[80] A. Atakan, E. Erdtman, P. Mäkie, L. Ojamäe, M. Odén, Time evolution of the CO2 hydrogenation to fuels over a Cu-Zr-SBA-15 catalyst, Accept. Publ. J. Catal. (2018).

Supporting Information for 'Effects of the chemical state of mesoporous CuO_x-Zr-SiO_2 catalysts on CO_2 hydrogenation'

Aylin Atakan[1,*], Julien Keraudy[2], Peter Mäkie[1], Christian Hulteberg[3], Emma M. Björk[1], and Magnus Odén[1]

[1] Nanostructured Materials, Department of Physics, Chemistry and Biology, Linköping University, Linköping SE-58183, Sweden

[2] Plasma and Coatings Physics, Department of Physics, Chemistry and Biology, Linköping University, Linköping SE-58183, Sweden

[3] Department of Chemical Engineering, Lund University, Lund SE-22100, Sweden

* aylin.atakan@liu.se

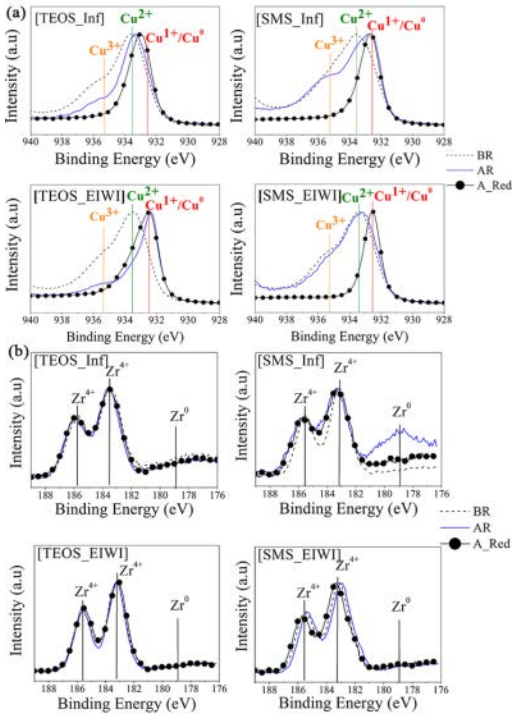

Figure S4. Comparative XPS spectra for Cu (a) and Zr (b) of catalysts [TEOS_Inf], [SMS_Inf], [TEOS_EIWI] and [SMS_EIWI]: as-synthesized (BR: before reaction), after reduction (A_red) and reacted (AR: after reaction).

The Cu 2p and Zr 3d core levels spectra are presented in the Fig S3.(a) and (b). All the Cu 2p spectra exhibit three main features: a main peak located at ~933.4 eV, a second peak at ~935.2 eV and a shoulder at ~932.3 eV. According to the literature, all the contributions are attributable to Cu atoms engaged in Cu-O frameworks with different oxidation states: Cu_2O (Cu^+) for the shoulder, CuO (Cu^{2+}) for the major peak and Cu_2O_3 (Cu^{3+}) for the second peak at higher energy. The main Cu peak is fitted to these components as presented in Figure S4. The Zr 3d spectra show a sharp doublet shape at ~ 182.6 eV and ~184.6 eV due to the spin-orbit splitting into the Zr 3d $_{5/2}$ and Zr 3d $_{3/2}$ which can be assigned to zirconium atoms belonging to the Zr-O framework (ZrO_2)[1,2].

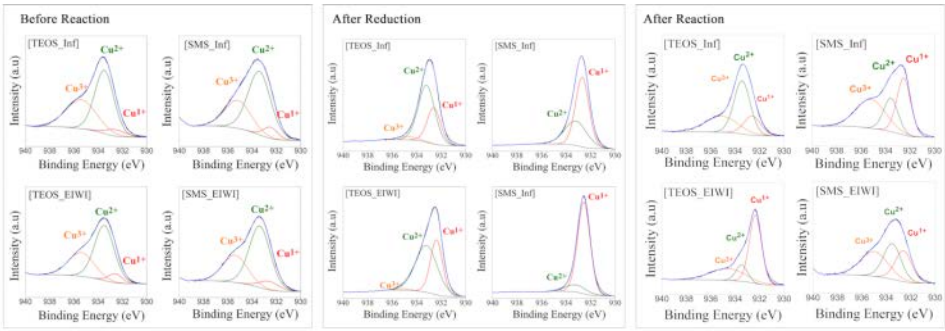

Figure S2. Cu 3p core-level spectra of catalysts [TEOS_Inf], [SMS_Inf], [TEOS_EIWI] and [SMS_EIWI]: before (a) and after reaction (b) with the corresponding spectra deconvolution.

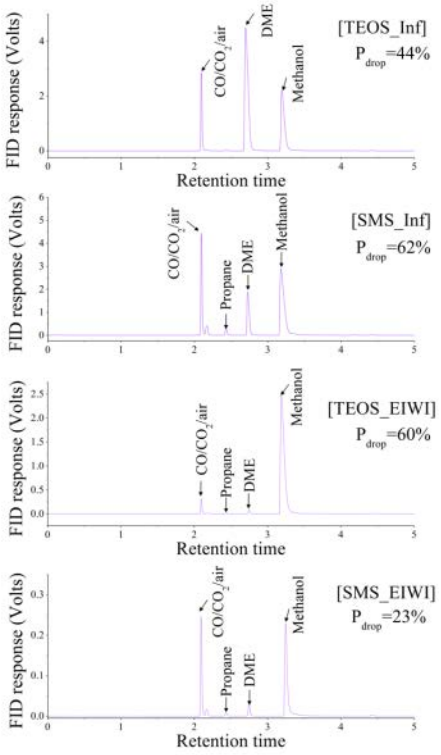

Figure S3. FID chromatograms obtained from GCMS.

Table S1. Peak identification of DRIFTS spectra.

Wavenumber (cm^{-1})	Compound ID	Wavenumber (cm^{-1})	Compound ID	Wavenumber (cm^{-1})	Compound ID
3730	CO2	2947	Methanol Butane Propane	2845	Methanol
3702	CO2	2935	EME Butane Propane MF	2834	DME EME Methanol
3627	CO2	2926	Methoxy DME MF	2818	Methoxy DME
3597	CO2	2918	DME	2806	Methoxy
3015	methane MF	2907	EME Ethanol	2388-2281	CO2
2978	Methanol EME Ethanol Butane Propane	2890	DME EME Ethanol Butane	2177	CO
2967	Methanol EME Ethanol Butane Propane MF	2877	Butane Propane	2112	CO
2957	Methoxy MF Propane EME	2854	Methoxy		

* including the noise between 3220-3050

The bands of CO_2[3,4], methane[3–5], methyl formate (MF)[3,6,7], methanol[3,6,8–12], dimethyl ether (DME)[3,13,14], methoxy[3,10,14,15], ethyl methyl ether (EME)[3,16], ethanol[3,17–19], butane[3,20,21], propane[3,22,23] and CO[3,5,24,25] were obtained from references.

REFERENCES

(1) Kaufmann, R.; Klewe-Nebenius, H.; Moers, H.; Pfennig, G.; Jenett, H.; Ache, H. J. XPS Studies of the Thermal Behaviour of Passivated Zircaloy-4 Surfaces. *Surf. Interface Anal.* **1988**, *11* (10), 502–509.

(2) Balaceanu, M.; Braic, M.; Braic, V.; Vladescu, A.; Negrila, C. C. Surface Chemistry of Plasma Deposited ZrC Hard Coatings. *J. Optoelectron. Adv. Mater.* **2005**, *7* (5), 2557–2560.

(3) NIST Chemistry WebBook, NIST Standard Reference Database Number 69.

(4) Weng, W. Z.; Chen, M. S.; Wan, H. L. Mechanistic Study of Partial Oxidation of Methane to Syngas Using in Situ Time-Resolved FTIR and Microprobe Raman Spectroscopies. *Chem. Rec.* **2002**, *2* (2), 102–112.

(5) Aoki, Y.; Tominaga, H.; Nagai, M. Hydrogenation of CO on Molybdenum and Cobalt Molybdenum Carbide Catalysts - Mass and Infrared Spectroscopy Studies. *Catal. Today* **2013**, *215*, 169–175.

(6) Chuang, C.-C.; Wu, W.-C.; Huang, M.-C.; Huang, I.-C.; Lin, J.-L. FTIR Study of Adsorption and Reactions of Methyl Formate on Powdered TiO2. *J. Catal.* **1999**, *185* (2), 423–434.

(7) Burke, D. J.; Puletti, F.; Woods, P. M.; Viti, S.; Slater, B.; Brown, W. A. Adsorption and Thermal Processing of Glycolaldehyde, Methyl Formate, and Acetic Acid on Graphite at 20 K. *J. Phys. Chem. A* **2015**, *119* (26), 6837–6849.

(8) Yu, J.; Mao, D.; Han, L.; Guo, Q.; Lu, G. Synthesis of C2 Oxygenates from Syngas over Monodispersed SiO2 Supported Rh-Based Catalysts: Effect of Calcination Temperature of SiO2. *Fuel Process. Technol.* **2013**, *106*, 344–349.

(9) Forester, T. R.; Howe, R. F. In Situ FTIR Studies of Methanol and Dimethyl Ether in ZSM-5. *J. Am. Chem. Soc.* **1987**, *109* (17), 5076–5082.

(10) Loyd J. Burcham, †; Laura E. Briand, ‡ and; Israel E. Wachs*, §. Quantification of Active Sites for the Determination of Methanol Oxidation Turn-over Frequencies Using Methanol Chemisorption and in Situ Infrared Techniques. 1. Supported Metal Oxide Catalysts. *Langmuir* **2001**, *17* (20), 6164–6174.

(11) Ladera, R.; Finocchio, E.; Rojas, S.; Fierro, J. L. G.; Ojeda, M. Supported Niobium Catalysts for Methanol Dehydration to Dimethyl Ether: FTIR Studies of Acid Properties. *Catal. Today* **2012**, *192* (1), 136–143.

(12) Xu, L.-H.; Lees, R. M.; Wang, P.; Brown, L. R.; Kleiner, I.; Johns, J. W. C. New Assignments, Line Intensities, and HITRAN Database for CH3OH at 10μm. *J. Mol. Spectrosc.* **2004**, *228* (2), 453–470.

(13) G. N. Bondarenko, E. A. Volnina, M. A. Kipnis, A. S. Rodionov, P. V. Samokhin, G. I. L. Surface Reactions of Dimethyl Ether on γ-Al2O3. *Russ. J. Phys. Chem. A* **2016**, *90* (2), 458–465.

(14) Kecskeméti, A.; Barthos, R.; Solymosi, F. Aromatization of Dimethyl and Diethyl Ethers on Mo2C-Promoted ZSM-5 Catalysts. *J. Catal.* **2008**, *258* (1), 111–120.

(15) Chen, L.; Wang, S. Infrared Spectra of Methanol Desorption in a He Stream and under Vacuum on CeO_2 and ZrO_2 Catalyst Surfaces. *RSC Adv.* **2016**, *6* (24), 19792–19793.

(16) Senent, M. L.; Ruiz, R.; Villa, M.; Domínguez-Gómez, R. CCSD(T) Study of the Far-Infrared Spectrum of Ethyl Methyl Ether. *J. Chem. Phys.* **2009**, *130* (6).

(17) Yu, A.; Lin, K.; Zhou, X.; Wang, H.; Liu, S.; Ma, X. New C-H Stretching Vibrational Spectral Features in the Raman Spectra of Gaseous and Liquid Ethanol. *J. Phys. Chem. C* **2007**, *111* (25), 8971–8978.

(18) Drobyshev, A.; Aldiyarov, A. IR-Spectroscopy of Ethanol Formed by Recondensation from a Nitrogen Cryomatrix. *Low Temp. Phys.* **2011**, *37* (8), 718–724.

(19) Drobyshev, A.; Aldiyarov, A.; Katpaeva, K.; Korshikov, E.; Kurnosov, V.; Sokolov, D. On the Stability of Ethanol Nanoclusters in a Nitrogen Cryomatrix. *Low Temp. Phys.* **2013**, *39* (11), 961–966.

(20) Pele, L.; Šebek, J.; Potma, E. O.; Benny Gerber, R. Raman and IR Spectra of Butane: Anharmonic Calculations and Interpretation of Room Temperature Spectra. *Chem. Phys. Lett.* **2011**, *515* (1–3), 7–12.

(21) Goodman, M. A.; Sweany, R. L.; Flurry, R. L. Infrared Spectra of Matrix-Isolated, Crystalline Solid, and Gas-Phase C3-C6, N-Alkanes. *J. Phys. Chem.* **1983**, *87* (9), 1753–1757.

(22) Solymosi, F.; Nemeth, R.; Ovari, L.; Egri, L. Reactions of Propane on Supported Mo2C Catalysts. *J. Catal.* **2000**, *195* (2), 316–325.

(23) Subbotina, I. R.; Kazanskii, V. B. Use of the IR Spectra of Adsorbed Ethane and Propane Molecules to Characterize the Strength of Active Sites in Zeolites and to Analyze the Activation of C-H Bonds in These Paraffins. *Kinet. Catal.* **2008**, *49* (1), 138–148.

(24) Fisher, I. a; Bell, A. T. In-SituInfrared Study of Methanol Synthesis from H2/CO2over Cu/SiO2and Cu/ZrO2/SiO2. *J. Catal.* **1997**, *172* (1), 222–237.

(25) Gausemel, I.; Ellestad, O. H.; Nielsen, C. J. On the Use of Infrared Spectroscopy in the Study of Carbon Dioxide Decomposition on Copper Containing Methanol Synthesis Catalysts. *Catal. Letters* **1997**, *45*, 129–133.

Paper 3

Time evolution of the CO_2 hydrogenation to fuels over Cu-Zr-SBA-15 catalysts

A. Atakan, E. Erdtman, P. Mäkie, L. Ojamäe, and M. Odén

J. Catal. 362 (2018) 55
DOI: 10.1016/j.jcat.2018.03.023

ATTENTION¡¡
Pages 135 to 145 of the thesis are available at the editor's web
https://www.sciencedirect.com/science/article/pii/S0021951718301246

Paper 4

Cu and Zr modified SBA-15 as drug carriers

A. Atakan, C. Canal, P. Mäkie, M. Odén, and M. Ginebra

Submitted for publication

Cu and Zr modified SBA-15 as drug carriers

Aylin Atakan[a,b], Cristina Canal[b,c*], Peter Mäkie[a], Magnus Odén[a], and Maria-Pau Ginebra[b,c,d]

[a] *Nanostructured Materials, Department of Physics, Chemistry and Biology, Linköping University, Linköping SE-58183, Sweden.*

[b] *Biomaterials, Biomechanics and Tissue Engineering Group, Department of Materials Science and Metallurgy, Technical University of Catalonia (UPC), Av. Diagonal 647, 08028 Barcelona, Spain*

[c] *Barcelona Research Center in Multiscale Science and Engineering, Universitat Politècnica de Catalunya, Barcelona, Spain*

[d] *Institute of Bioengineering of Catalonia (IBEC) c/ Baldiri i Reixach 10-12, 08028 Barcelona, Spain*

**Corresponding author: email: cristina.canal@upc.edu*

ABSTRACT: Mesoporous silica is a potential drug carrier due to its porous network and its antibacterial activity is of interest. In this context, we have synthesized bioactive nanoassemblies of SBA-15 composed of Zr doping (Zr-SBA-15) and Cu nanoparticles (Cu-Zr-SBA-15) through self-assembly and infiltration processes. The self-assembly process yielded monodispersed cylindrical particles (rods) of SBA-15 and Zr-SBA-15 with pores running along the length of these rods with diameters larger than the traditional SBA-15 pore size (>10 nm). The infiltration process yielded Cu nanoparticles grown inside the pores of these mesoporous rods to take advantage of the high specific surface area and obtain nanoparticle diameter smaller than 10 nm. The prepared drug carriers were loaded with a 2% chlorhexidine digluconate solution. For each carrier, a loading percentage of 25-40 % [g drug/g (drug+carrier)] was achieved without destroying their porous network. Release occurred in two stages. First, a burst release of the drug weakly attached to the carrier followed by a slow desorption of the drug more strongly attached to the pore walls of the porous framework. Release profiles reveal that Zr in the SBA-15 framework and Cu nanoparticles positioned in the pores of the carrier can be used to control the release rate, i.e. restrict the burst and slow down the release, which is attributed to the enhanced acidity and possibly to increased tortuosity. The chemical bonding between the drug and the carrier is confirmed by FTIR via N-H and O-H vibration bands. Antibacterial efficiency is shown qualitatively and quantitatively by employing agar diffusion and dynamic tests against Staphylococcus aureus and Escherichia coli.

Keywords: *Zr doped SBA-15, Cu nanoparticles, mesoporous materials, chlorhexidine, drug delivery, antibacterial*

1. INTRODUCTION

Drug delivery has been one of the major application areas of mesoporous materials for more than a decade, and in many studies they are acknowledged as valuable pharmaceutical molecule hosts due to their large specific surface area and pore volume[1]. After the first report of MCM-41 molecular sieve in 1992[2], mesoporous silica stood out as a favorable bioactive drug carrier with its high mechanical and thermal stability, and hexagonal pore structure with narrow pore size distributions [3–8]. These materials can be coated with functional groups (such as methyl and amine) due to the presence of silanol groups on the their surfaces and this functionalization can be controlled independently for the outer surface of the mesoporous particles and the pore surface[9]. Later on, SBA-15 was developed with larger pore size and thicker walls than MCM-41 resulting in higher adsorption capacity and improved stability [1,10–12]. However, drug release reports with SBA-15 carriers are usually restricted to small pore sizes (below 10 nm) and to specific surface area below 600 m^2/g [11,13–16]. Moreover, it is very rare to see a good particle morphology control while maintaining a large pore size and high specific surface area, especially in the presence of additional atoms such as Zr incorporated into the framework (SiO_2-ZrO_2).

It is the objective of this work to develop hybrid materials based on SBA-15. To that aim, SBA-15, Zr-SBA-15 and Cu-Zr-SBA-15 were synthesized via a recently reported route[17]. The synthesized materials were used for delivery of an antibacterial drug: Chlorhexidine (CHX). CHX is a typically used as an antibacterial drug which is mostly used for the treatment of periodontal diseases due to its antiseptic properties against several gram-negative and gram-positive bacteria as well as fungi [18–21]and in this study it is chosen as a model cationic drug molecule to study release from the prepared SBA-15 based carriers. It is typically

The drug carrier design was chosen to provide a material with controllable and reliable characteristics including high loading diffusion capacity. To achieve this a mesoporous matrix with high specific surface area, large pore diameter and monodispersed rod particle morphology was chosen. Such kind of morphology has proven beneficial for other drug delivery systems investigated, for instance, in cancer therapy[22,23]. In our work, the addition of Zr and Cu provides additional functionalities of relevance to the aimed drug delivery application, such as polarity and antibacterial activity. Doping SBA-15 with Zr was done to enhance the acidity in order to increase the affinity to cationic molecules such as CHX, while high stability is maintained [17,24]. Zirconia has been previously reported to increase the acidity [28] of mesoporous silica when doped and favors the dispersion of Cu nanoparticles [29]. Cu nanoparticles were grown in the mesopores of Zr-SBA-15 by an infiltration method [17]. Copper has antibacterial properties and is commonly used on surfaces that are

exposed to repetitive human contact, especially in hospitals and against parasites in agriculture[30,31]. Cu has been shown to have antibacterial activity not only as a bulk material but also as nanoparticles in metal or oxide forms [30–42]. Therefore, in our work, Cu was added to enhance the antibacterial effect of CHX for potential applications. Additionally, its contribution to the polarity of the mesoporous support is investigated with regards to the drug release properties and its relationship regarding the interactions between the carrier and the drug.

Although mesoporous silica has been reported as a drug carrier[42–44], publications on the use of mesoporous silica for CHX release are rare. SBA-15 is previously shown to be a potential bone filler for dental applications [3,43,44], therefore it is of interest to study this material and its diversified forms for release of a model antibacterial drug. Hereby we report the in-vitro drug delivery performance (CHX loading, release and antibacterial activity) of a molecular sieve in its pure and modified forms: SBA-15 w/wo Zr doping and w/wo Cu nanoparticles infiltrated inside the pores

2. EXPERIMENTAL SECTION

Poly(ethylene glycol)-block-poly(propylene glycol)-block-poly(ethylene glycol) (Pluronic P123, $EO_{20}PO_{70}EO_{20}$, av. M_n~5800, Aldrich), ammonium fluoride (NH_4F) (≥98.0%, Fluka), sodium chloride (NaCl) (≥99.8%, Sigma-Aldrich), hydrochloric acid HCl (≥37.0%, Sigma-Aldrich), heptane (99%, Sigma-Aldrich), tetraethyl orthosilicate (TEOS, 98%, Sigma-Aldrich), zirconium(IV) oxychloride octahydrate ($ZrOCl_2{\cdot}8H_2O$) (≥98.0%, Sigma-Aldrich), chlorotrimethylsilane (TMCS, ≥99.0%, Aldrich), (3-aminopropyl)trimethoxysilane (APTMS, 97%, Aldrich), toluene (≥99.7%, Sigma-Aldrich) and copper(II) sulfate pentahydrate ($CuSO_4$) (≥99%, Sigma-Aldrich) were used as received in the synthesis of the mesoporous materials. Chlorhexidine digluconate solution (20% in H_2O, Sigma) was used without further purification.

2.1. Synthesis and Characterization of the Mesoporous Drug Carrier

SBA-15

SBA-15 was synthesized via a hydrothermal route reported by Johansson et. al. [45] where a TEOS-heptane mixture was stirred in the precursor solution for 4 minutes (precursor solution: P123 and NH_4F dissolved in HCl solution) at 20°C. The molar ratios in the synthesis solution were H_2O:HCl:P123:NH_4F:TEOS:heptane = 9116:356:1:1.8:54:16.5. Subsequently, the solution was left under static conditions at 20 °C for one hour and then hydrothermally treated in a PTFE bottle at 80 °C for 24 hours. The obtained slurry was filtered and washed. To remove the remaining P123 micelles in the pores of the nanoparticles, the solid material was calcinated at 550 °C for 5 hours.

Zr-SBA-15

Zr-SBA-15 was prepared as reported in Atakan et. al.[17] . Briefly, the same route as SBA-15 was used with the same molecular ratios in the synthesis solution except for two altered steps: (1) zirconium oxychloride (with Si/Zr=10 molar ratio) was premixed into the precursor solution before the TEOS-heptane mixture was added, (2) the static time after stirring was prolonged to 5 hours to obtain complete formation of Zr-SBA-15 rods.

Cu-Zr-SBA-15

Cu was added to the mesoporous matrix as nanoparticles via an infiltration route. The mesoporous particles were functionalized with chemical groups for selective Cu settlement inside the pores rather than large agglomerations on the outer surface of the particles. The outer surface of the mesoporous particles was covered with methyl groups in order to passivate the outer surface. The inner surface of the pores was functionalized with amine groups (NH_2^-) in order to enhance Cu ion (Cu^+) attachment by electrostatic forces on these surfaces.

In those cases, when an outer surface passivation was applied, calcination was not performed at the end of the (Zr-)SBA-15 synthesis in order to keep the pores filled with P123 and thereby limit the amount of methyl groups inside the pores. The methyl functionalization was obtained by stirring Zr-SBA-15 particles with 15 vol% TMCS in toluene at 80 °C for 8 hours, filtrating the solid and calcining at 300°C for 5 hours in order to remove P123 while maintaining the methyl groups. For activation of the surface of the pores, the Zr-SBA-15 powders were stirred with 6.25 vol% APTMS in toluene for 24 hours at room temperature. Subsequently, soxhlet extraction was performed to remove excess APTMS and the product was obtained after filtering and washing with toluene.

The functionalized mesoporous materials were dried at 100 °C for 2 hours and stirred with 0,06 M Copper sulfate ($CuSO_4$) solution with a concentration of 20 mg/ml for 24 hours at room temperature. The product was recovered by filtering and carefully washed with deionized water. The filtrate was stirred with $NaBH_4$ solution to reduce the Cu. Finally, the recovered solid was calcined at 550°C for 5 hours for complete micelle removal from the micropores, degradation of the functional groups, and Cu nanoparticle growth.

The synthesis routes of all three materials are schematized in Figure 1.

Characterization

The mesoporous particle morphology and pore arrangement were determined by Scanning Electron Microscopy (SEM) (LEO 1550 Gemini operated at 3 kV) and Transmission Electron Microscopy (TEM) (FEI Tecnai G2), using carbon coated copper grid sample holders. The elemental analysis (atomic ratios of Si/Zr and Si/Cu) was obtained by an EDS system (Oxford X-Max 80) coupled to the SEM. An electron accelerating voltage of 20 kV and correction factors provided by the manufacturer were used for the elemental analysis.

The pore size and shape were characterized by determining the nitrogen physisorption behavior of the material using a Micromeritics ASAP 2020 device. The Kruk-Jaroniec-Sayari (KJS) method [46] was used to compute the pore size distribution from the adsorption isotherm, and the Brunauer-Emmet-Teller (BET) method [47] was to determine the specific surface area (SSA) at a pressure ratio (P/P_0) between 0.08 and 0.16.

Small angle x-ray diffractometry (SAXRD) was performed using a Panalytical Empyrean equipped with a Cu Kα x-ray source operated in line focus. The recorded data was used to determine the pore arrangement of the materials. A Panalytical X'Pert Pro diffractometer and also equipped with a Cu Kα x-ray source was used for phase identification and size determination of the Cu nanoparticles. The particle size was extracted using the Scherrer equation [48].

2.2. Drug loading

The mesoporous materials were loaded with CHX by the following procedure: 20 mg of each material were vortexed in 6 ml of a 2% CHX solution for 1 minute followed by 30 minutes of ultrasonic treatment. The dispersed powders were further vortexed during 1 more minute and left to impregnate for 4 h with 50 rpm shaking (IKA KS 260 basic orbital shaker). The final suspensions were centrifuged, and freeze dried. The CHX loaded samples are referred to as CHX-[sample name] where the [sample name] is [SBA-15], [Zr-SBA-15] or [Cu-Zr-SBA-15].

The drug-loaded powders were analyzed by thermogravometric analysis using a Mettler-Toledo TGA/STDA 851^e device. 3 mg of sample were analyzed in a 70 ml aluminium crucible and heated at 10 °C/min from 25 to 800 °C under a flow of 50 ml/min N_2. Liofilized CHX digluconate was analyzed as reference. The final CHX loading of the samples was calculated by the formula below based on the mass loss between 120 and 800 °C. The mass loss before 120 °C is due to water desorption from the mesoporous matrix.

$$CHX\ loading = \frac{\%\ mass\ loss\ loaded\ samples - \%\ mass\ loss\ empty\ samples}{\%\ mass\ loss\ pure\ drug} * 100 \quad (1)$$

The drug loading was further investigated by transmission Fourier-transform infrared spectroscopy by preparing KBr pellets that contained 0.8-1.0 mg of sample. Measurements were conducted by a Bruker Vertex 70 spectrometer equipped with a water cooled MIR source and a DLaTGS detector. Spectra were acquired with 2 cm^{-1} resolution and each spectrum is the averaged from 16 scans. Final spectra were normalized against the characteristic Si-O-Si band of SBA-15 for each sample.

2.3. Drug release

CHX loaded powder samples were liofilized and pressed into flakes in a uniaxial isostatic press by applying 8 tons for 8 minutes at room temperature. In vitro release tests were performed by immersing 20 mg of the prepared flakes in 40 ml of MilliQ H_2O at 37 °C and 350 rpm stirring rate. Flakes were contained in USP baskets to prevent impact with the stirring magnet. 1 ml aliquots were withdrawn at predetermined time points and replaced by 1 ml of MilliQ H_2O to keep the volume constant. The concentration of each aliquot was measured by UV-Vis Spectroscopy at λ_{max}=254 nm using a UV-visible-NIR Shimadzu ISR-3100 device. The obtained concentration values were corrected taking into account the evaporation occurred during the experiment, the drug amount in the withdrawn solution, and the dilution introduced by the additions of H_2O after sampling. The release results are presented as cumulative release fractions, and M_t/M_{inf} where M_t is the cumulative drug concentration in the solution at a specific time t and M_{inf} is the maximum amount of drug released when stationary conditions was reached.

The release kinetics was evaluated over four replicates by fitting the M_t/M_{inf} vs. time plot to the suitable mathematical models using Matlab software (The Mathworks Inc., USA).

2.4. Antibacterial activity

The antibacterial activity of the drug-loaded materials was tested against two bacterial strains commonly found in nosocomial infections: *Staphylococcus aureus* (CCUG 15915) and *Escherichia coli* (CECT 101).

Qualitative antibacterial testing

To evaluate the qualitative antibacterial effectiveness the agar diffusion test was employed. This test qualitatively determines the effectiveness of a diffusible antimicrobial agent to inhibit bacterial growth, while being a relatively quick and easy assay. The culture media was prepared by dissolving 15 g/l agar bacteriological (Scharlau, ref.no. 07-004-500) and 37 g/l brain heart infusion (Scharlau, ref.no. 02-599-500) in 1 L water which was then sterilized by autoclaving. The test was performed by plating 10^7 colony forming units (CFU) on agar plates. A flake of each sample weighing between 1 and 2 mg was gently placed on the seeded agar plate. After 24 hours of incubation at 37°C digital images were recorded. The software Photoshop's quick selection tool was used to determine the total number of pixels at the bacteria-free zone around each flake and it is presented as inhibition zone (I).

The results are presented by normalizing the I values by mass: I/m (cm/g). 3 replicates of each sample type were evaluated.

Quantitative antibacterial testing

For quantitative antibacterial assessment, continuous measurement of the growth curves of bacterial suspensions were employed. The test briefly consisted of placing the samples in a suspension of either S. aureus or E. coli adjusted to an optical density of 0.02, and measuring the evolution of the optical absorbance (Synergy HTX Multimode Reader, BioTek Instruments, Inc.) every 10 min for 24 h at 37°C. To avoid interference from the materials in the readings, the test was performed in 48 well plates, where the wells had been connected in groups of 2. 2 ml of bacterial suspension media were added in each group of 2 wells, the drug containing flakes of around ~20 mg were placed in one of the wells and the readings were made in the other well. The % of the bacterial inhibition of S. aureus and E. coli at each time point are presented along with the fitted curve to data in order to show the trend.

The resulting optical density values are converted to percent inhibition I(%) with the formula below [49–51]:

$$I(\%) = \left(1 - \frac{OD_{St} - OD_{S0}}{OD_{Ct}}\right) * 100 \quad (2)$$

OD_{St} : Optical density of a sample loaded test well at a time point t

OD_{S0} : Optical density of a sample loaded test well at the time point 0

OD_{Ct} : Optical density of a positive control (bacterial suspension) well at a time point t.

The results are averaged over three replicates.

2.5. Statistics

The overall statistical differences between test groups were analyzed by applying Tukey's post hoc method via one way ANOVA (Minitab 16 software, Minitab Inc., USA) with 95% significance level.

3. RESULTS and DISCUSSIONS

Characterization of the Mesoporous Drug Carriers

In this study, three types of mesoporous carriers were investigated: SBA-15, Zr-SBA-15 and Cu-Zr-SBA-15. All the carriers are monodispersed rods with ordered single sized pores throughout each sample, which offer means to obtain controlled release. The SEM and TEM micrographs (Supporting information Figure S1(a-i)) confirm the targeted morphology where the obtained rods are observed to have a diameter between 200 and 500 nm and being 400-600 nm long. Zr-SBA-15 has the largest rod dimensions. The cylindrical pores are extended along the long dimension of the rods and they run parallel to each other. Pore size distributions of the carrier materials prior to loading are presented in Figure S1(j) in the supporting information, and all samples have a narrow pore size distribution, with a maximum between 10 and 20 nm. The hexagonal pore packing of all the materials is confirmed by three distinct x-ray diffraction peaks representing the planes 100, 110 and 200 and also observed by TEM (Figure S1(k)).

Cu infiltration resulted in Cu nanoparticles with sizes below 10 nm within the pores (Figure S1 (i) – darkest dots/areas). Moreover, Cu infiltration did not change the hexagonally pore structure (Figure S1(k)). EDS analysis revealed the mesoporous carrier composition as: Si/Zr = 12.6±0.2 for Zr-SBA-15, and Si/Zr = 19.6±0.9 and Si/Cu = 2.5±0.0 for Cu-Zr-SBA-15.

SSA of SBA-15 increases with Zr doping from 570 m^2/g to 723 m^2/g caused by a change of the synthesis environment in the presence of a Zr salt. Cu nanoparticles in the pores result in decreased SSA (336 m^2/g) and pore volume due to blockage (from 1.07 cm^3/g in SBA-15 and 1.32 cm^3/g in Zr-SBA-15 to only 0.58 cm^3/g).

Drug Loading

The mass loss measured by TGA between 25-800°C of as-synthesized carriers: SBA-15, Zr-SBA-15 and Cu-Zr-SBA-15, without any drug loading, display only one distinct mass decrease due to water loss between 25-120 °C (Figure 2(a)) when tested up to 800°C. This mass decrease is attributed to evaporation of physisorbed water and H_2O molecules that are formed when –OH surface groups react with each other [52]. The loss of water is more pronounced for the carriers without drugs (Figure 2(a)). Loss of water may occur during drug loading, as drug molecules penetrate the pores, and force water molecules out. Another contributing factor is entrapment of –OH groups by the drug molecules, which suppresses their evaporation. No mass change due to reactions involving carbon is expected since the carriers are calcined as the final step of their synthesis at 550°C for 5 hours. The slight mass loss at temperature values above 120°C, is due to dehydroxilation i.e. depletion of the remaining –OH surface groups [52]. The mass losses due to dehydroxilation are 3.6% for SBA-15, 5.5% for Zr-SBA-15 and 5.9% for Cu-Zr-SBA-15. The ratio of mass loss percentage per unit surface area (mass loss%/m^2) between the samples is SBA-15 : Zr-SBA-15 : Cu-Zr-SBA-15 = 1:1.2:2.7. The marked difference in Cu-Zr-SBA-15 can be related to a greater density of surface –OH groups on this material, which *a priori* can result in an enhanced surface activity for drug attachment, enabling higher drug retention. This complies with the improved surface acidity (resulting from more –OH attachment) of Zr and Cu integrated mesoporous materials[28,53,54].

Two distinct mass loss steps in the TGA curves of CHX digluconate (Supporting information Figure S2) and loaded mesoporous materials (Figure 2(a)) are observed. This mass loss due to complete CHX decomposition between 120 and 800°C, is determined to be 80.01 %. This value is used in Equation (1) to calculate the CHX loading. The CHX loading (as defined by Eq. 1) in the different materials is between 26.7 ± 1.0 % and 40.0 ± 0.1 % (Figure 2(b)). The loadings were also normalized by the SSA in order to elucidate any carrier-drug interactions. The loading performance of Cu-Zr-SBA-15 per unit surface area is higher than the other two carrier types where Zr-SBA-15 also shows better loading characteristics per unit SSA than SBA-15. The differences in loading per SSA can be attributed to an enhanced acidity of the mesoporous carrier by the addition of metal atoms (Zr or Cu) [28,53,54]. Moreover, it has been reported that merging of multiple metal atoms in the same system enables synergetic effects between different acid sites (Lewis and Brönsted) and therefore enhancing the acidity of the material [55]. This acidity could account for weak acid/base interactions between the drug and the substrate, which would be enhanced by having two elements, Cu and Zr simultaneously present in the mesoporous material.

The physisorption test results showed that the N_2 adsorption isotherms (Figure S3 (a)) are type IV isotherms displaying a type 1 hysteresis loop that indicates well-defined open cylindrical pores with and without the drug loading [56]. Micropore volumes (which were of 0.2 cm^3/g in SBA-15 and in Cu-Zr-SBA-15 & 0.5 cm^3/g in Zr-SBA-15) become zero upon drug loading, which indicates penetration of the drug into the micropores. The drug loaded mesoporous particles show a distinct drop in pore volume due to drug occupation. The size of this drop follows the same trend as loading per SSA. Drug infiltration did not modify the pore structure as seen in the SAXRD results when comparing the drug loaded samples in Figure S3 (b) with the materials prior to loading in Figure 1(k). For further investigation of drug attachment, FTIR spectroscopy measurements were performed on the loaded samples as well as the materials without any drug loading (Supporting Information Figure S4).

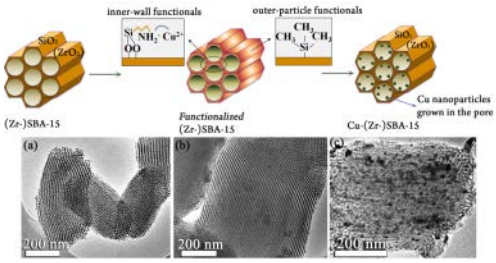

Figure 1. Synthesis route of SBA-15, Zr-SBA-15 and Cu-Zr-SBA-15

The FTIR results (normalized) of the carriers before and after drug loading allowed detecting the characteristic bands of the mesoporous material at 3400 cm^{-1} for OH vibration, 1627 cm^{-1} for water deformation δH_2O; 1240 cm^{-1}, 1086 cm^{-1}, 800 and 465 cm^{-1} as Si-O-Si bands, 960 cm^{-1} for Si-OH vibrations, and 980 cm^{-1} as Zr-O-Si band [57–60].

The drug loaded samples exhibit additional bands characteristic for CHX digluconate: 1680-1510 cm^{-1} for multiple vibrations of C-C, $C=C^{aromatic}$, N-H, C-O and C-N; 1493 cm^{-1} for C-Cl stretching; 1417 cm^{-1} for COO stretching; 824 cm^{-1} CH bending of the aromatic group; and 726 cm^{-1} for C-N stretching [28,59,61–65]. The chlorhexidine digluconate drug spectrum is presented in the supporting information Figure S5.

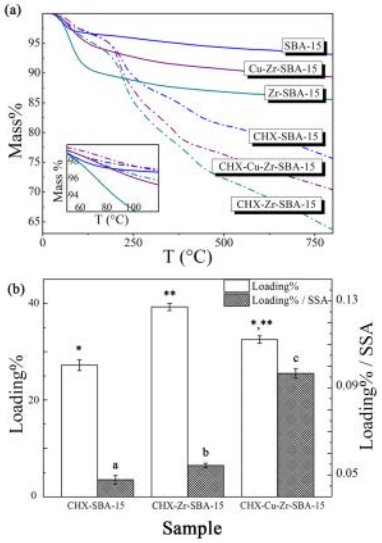

Figure 2. Thermogravimetric mass loss of (a) of the different samples prior to and after drug loading and (b) drug loading % and drug loading % / SSA calculated from the TGA data. Different symbols (*, **) and (a,b,c) indicate statistically significant differences

The band between 3430-3412 cm^{-1} corresponding to OH vibrations on the surface of the carriers prior to drug loading, shifts to lower vibrational wavenumbers upon CHX addition, especially in Cu-Zr-SBA-15. This shift is 10 cm^{-1} for SBA-15, 11 cm^{-1} for Zr-SBA-15 and 73 cm^{-1} for Cu-Zr-SBA-15. The -OH vibrations originate from the OH end surface groups of the mesoporous carrier as well as the physisorbed water. This shift can be attributed to two reasons: (i) Molecular attachment of drug on the surface via OH groups, and (ii) increase in the amount of the NH stretching band of the drug that normally occurs at 3340 cm^{-1}, due to their overlap (Figure S4 and S5). Additional data on the pore characteristics of the drug carriers after loading are included in Supporting Information Table S1.

Drug Release

The cumulative CHX release data is presented in Figure 3(a) as cumulative released % vs. time, and the corresponding final values are presented in Table 1. The release kinetics of the three materials display similar profile, with a burst release in the first hours, followed by stabilization. The three materials reach the stationary state after 10-20h depending on the sample, so in all cases a certain fraction of the drug remains trapped in the material. The relatively fast release in water in 10-20 h can be expected to be translated to a much more gradual release in PBS, as shown in an earlier study also dealing with CHX release[66]. It can be observed that the cumulative released % follows: SBA-15 > Zr-SBA-15 > Cu-Zr-SBA-15. Cu-Zr-SBA-15 releases the lowest final amount (M_{inf}) while Zr-SBA-15 releases the most (Table 1). This result is consistent with the specific surface area values of the carriers prior to drug loading presented in the previous section. The fact that the CHX released % from SBA-15 is higher than Zr-SBA-15 (Figure 3(a), Table 1), while the released amount (M_t) follows an opposite order, being lower for SBA-15 compared to Zr-SBA-15 (Figure 3(b), Table 1), indicates less strong bonding between the drug and the mesoporous material in SBA-15. Cu-Zr-SBA-15 having the lowest released % and M_t may indicate the strongest bonding between the drug and the carrier. As mentioned earlier, TGA results showed that –OH surface group density was higher for Cu-Zr-SBA-15 compared to other carriers, so the electronegative surface attachment between the carrier and the cationic drug is possibly related to the low percentage (28.2 ± 0.7 %) of the drug loaded being released after 72h (Table 1), in addition to increased tortuosity due to the presence of the Cu nanoparticles partially blocking the pores. Similarly, the total released percentage of CHX-Zr-SBA-15 is around 15% lower than that of CHX-SBA-15, which is consistent with TGA results that indicated similar surface OH group concentrations for Zr-SBA-15 and SBA-15, although slightly higher for Zr-SBA-15.

Table 1. Drug release final percentage, cumulative amount released and modelling results.

Sample		**Final CHX Released %**	**Final CHX M_{inf} (mg)**
CHX-SBA-15		64.5 ± 2.3%	2.78 ± 0.10
CHX-Zr-SBA-15		50.5 ± 1.4 %	4.09 ± 0.09
CHX-Cu-Zr-SBA-15		28.2 ± 0.7 %	1.68 ± 0.14
CHX-SBA-15			
Phase	**k (1/h)**	**P**	**M_t (mg CHX)**
fast	8.46 ± 0.80	84.53 ± 2.76 %	2.35
slow	0.30 ± 0.13	13.95 ± 2.87 %	0.39
CHX-Zr-SBA-15			
Phase	**k (1/h)**	**P**	**M_t (mg CHX)**
fast	5.70 ± 1.94	34.87 ± 5.69 %	1.43
slow	0.49 ± 0.08	62.58 ± 6.18 %	2.56
CHX-Cu-Zr-SBA-15			
Phase	**k (1/h)**	**P**	**M_t (mg CHX)**
fast	13.36 ± 4.30	39.33 ± 3.85 %	0.66
slow	0.43 ± 0.07	56.64 ± 3.90 %	0.95

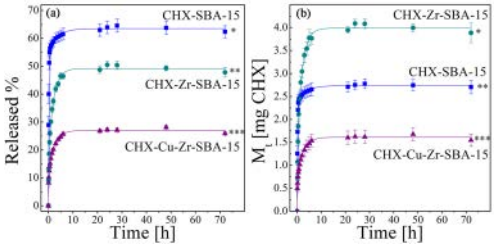

Figure 3. Cumulative CHX (a) released % and (b) released amount (M_t) from CHX-SBA-15, CHX-Zr-SBA-15 and CHX-Cu-Zr-SBA-15. Different symbols (*, **, ***) indicate statistically significant differences.

To reveal the kinetics behind the release trend of each sample the sum of two exponential functions was fitted to the data according to:

$$\frac{M_t}{M_{inf}} = P_1(1 - e^{-k_1 t}) + P_2(1 - e^{-k_2 t}) \qquad (3)$$

where P_1 is the percentage of release in the first phase, P_2 is the percentage of release in the second phase, k_1 is the rate constant at the first phase and k_2 is the rate constant at the second phase. The fits are given in the supporting information Figure S6. The inserts show the early-time release behavior. CHX-Zr-SBA-15 and CHX-Cu-Zr-SBA-15 release the drug in a slower manner (Figure 3) and the stationary stage is reached after 26 hours, which should be compared to CHX-SBA-15 where a strong burst occurs in the first hour where more than 60% of the drug is released and the stationary stage is reached after 10 hours.

The release from our mesoporous carriers can be explained by two phases: release of the drug molecules loosely held on the surface and in the void volume of the pores (first phase) and the drug molecules attached to the mesoporous framework/walls (second phase). The molecules attached to the walls release less easily compared to the loosely held ones. The first phase can be seen as the initial release burst and second one as slow release over a long time period. Previous works [67] studying the release of a dye (Rhodamine G) from mesoporous silica nanoparticles at different pHs, found similar two-phase release profiles. In line with our observations Ng et al [68] stated that a cationic molecule can have a second phase of release (following a simple diffusion phase) due to strong attachment to the anionic mesoporous silica surface, which was referred to as a 'self-rate-limiting mechanism' and therefore the whole release process cannot be described by simple diffusion activity.

The CHX amounts released during two phases of drug release (fast and slow) were determined by multiplying the M_{inf} value for each sample by the percentages (P) in either phase 1 or 2 (Table 1). Accordingly, drug release from SBA-15 can be observed to be dominated by the fast regime and only 14% of the released drug corresponds to the slow regime. For Zr-SBA-15 and Cu-Zr-SBA-15 the slow regime dominates the release behavior, during which more than 50% of the release occurs. The stronger anionic character of the metal containing carrier surfaces and thus a stronger connection between the carrier and the drug causes this change in behavior. The anionic character of Cu-Zr-SBA-15 surface is explained with a high OH surface group density. However, for Zr-SBA-15 this is likely caused by a negative charge on the surface generated by the presence of Zr.

Antibacterial Activity

Qualitative antibacterial activity of the drug-loaded mesoporous materials was tested against staphylococcus aureus and escherichia coli (Figure 4) since chlorhexidine has bactericidal effect and broad-spectrum efficacy [69]. Empty carriers were used as negative control and they demonstrated no inhibition zone. Accordingly, all CHX-loaded carriers display antibacterial activity, showing greater efficiency vs. E. coli (Figure 6(a)). It is interesting to note that the inhibition areas of the different materials are in direct correlation with the % released, being CHX-SBA-15 the material showing more inhibition and CHX-Cu-Zr-SBA-15 the one showing less inhibition (Figure 4(b)). It was previously described[69] that E. coli and S. aureus uptake chlorhexidine very fast depending on the chlorhexidine concentration and pH. The minimum inhibitory concentration of CHX for S. aureus is reported in 4 μg/mL, and that of E.coli in 2.67 μg/mL [70]. This lower susceptibility for S. aureus can explain the smaller inhibition areas found for S. aureus than for E.coli.

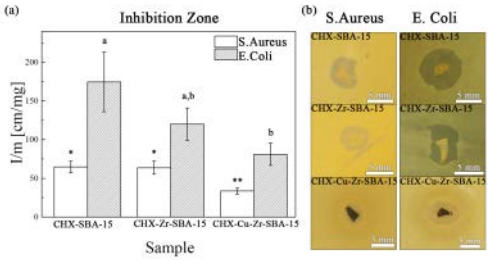

Figure 4. Inhibition zone normalized per unit mass (a) and images of the inhibition areas of the different materials (b). Different symbols (*, **) and (a,b) indicate statistically significant differences.

The maximum antibacterial efficiency during the quantitative antibacterial testing was reached between the first 2-6 hours for E. coli depending on the material tested and in 2 hours for S. aureus for the three samples and remained stable (Figure 5). SBA-15 and Zr-SBA-15 showed converging profiles in the quantitative antibacterial tests. The inhibition percentages of SBA-15 and Zr-SBA-15 reached 93% and 90% for S. aureus and of 73% and 97% for E.coli, respectively. Cu-Zr-SBA-15 displayed a slightly different behavior: while it initially displayed similar % of inhibition than the other materials, the % of bacterial inhibition decreased with time. This can probably be explained by the fact that CHX-Cu-Zr-SBA-15 displays much less CHX amount released: only 135.5 μg/mg carrier (Table 1, Figure 3), compared to other samples, which in turn, is related to the SSA. As a result, the antibacterial efficiency of the material is progressively reduced with time. Despite this, the maximum value of inhibition % (Figure 5), which was reached at around the time point of 250 min for S. aureus and 160 hours for E. coli, is almost the same for Cu-Zr-SBA-15 as Zr-SBA-15 which has a release amount of more than double of Cu-Zr-SBA-15. This could be due to fact that an antibacterial agent: Cu was integrated into the carrier.

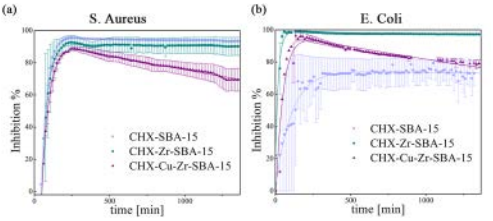

Figure 5. Inhibition percentage of SBA-15, Zr-SBA-15 and Cu-Zr-SBA-15 against staphylococcus aureus (a) and escherichia coli (b).

4. CONCLUSIONS

The potential of 3 different mesoporous carriers (SBA-15, Zr-SBA-15 and Cu-Zr-SBA-15) as drug delivery systems was studied with an antibacterial drug (chlorhexidine digluconate). Zr doping and Cu infiltration was shown to affect the morphology of the SBA-15 particles as well as its porous properties. As a result different CHX loading and release behaviors were obtained for the modified mesoporous materials. All samples displayed burst release profile at first, and good antibacterial activity.however significant differences in release % have been observed, being SBA-15 the sample with the highest release (65%) and Cu-Zr-SBA-15 the lowest (25%). BothZr-SBA-15 and Cu-Zr-SBA-15 show slower initial release profiles, possibly conferred by the stronger interactions carrier-drug due to the additions of Zr and Cu on the mesoporous network. While not all drug is released from the mesoporous materials, the fact that the stationary stage is reached in all cases and that the materials designed are not resorbable can avoid potential problems of bacterial resistance.

AUTHOR INFORMATION

Corresponding Author

* E-mail: cristina.canal@upc.edu

Notes

The authors declare no competing financial interest.

ACKNOWLEDGMENT

This work was financially supported by:
EU's Erasmus-Mundus program: The European School of Materials - Doctoral Programme - DocMASE;
Project MAT2015-65601-R, co-funded by the EU through European Regional Development Funds, and Ramon y Cajal fellowship of CC; Support for the research of MPG was received through the "ICREA Academia" prize for excellence in research, funded by the Generalitat de Catalunya.

REFERENCES

[1] M. Moritz, M. Geszke-Moritz, Mater. Sci. Eng. C 49 (2014) 114–151.

[2] J.S.C. Kresge, C. T. Leonowicz, M. E.Roth, W. J.Vartuli, J.Beck, Nature 359 (1992) 710–712.

[3] H. Fullriede, N. Timpe, L. Borchers, M. Stiesch, H. Menzel, P. Behrens, A. Chemie, L.U. Hannover, T. Chemie, T.U. Braunschweig, Z. Prothetik, 58 (2013) 9–10.

[4] E. Aznar, M.D. Marcos, R. Martínez-Máñez, F. Sancenón, J. Soto, P. Amorós, C. Guillem, J. Am. Chem. Soc. 131 (2009) 6833–43.

[5] A. Bernardos, L. Mondragon, E. Aznar, M.D. Marcos, R. Martinez-Mañez, F. Sancenon, J. Soto, J.M. Barat, E. Perez-Paya, C. Guillem, P. Amoros, ACS Nano 4 (2010) 6353–68.

[6] C.-P. Tsai, C.-Y. Chen, Y. Hung, F.-H. Chang, C.-Y. Mou, J. Mater. Chem. 19 (2009) 5737.

[7] C.-Y. Lai, B.G. Trewyn, D.M. Jeftinija, K. Jeftinija, S. Xu, S. Jeftinija, V.S.-Y. Lin, J. Am. Chem. Soc. 125 (2003) 4451–9.

[8] V. Mamaeva, C. Sahlgren, M. Lindén, Adv. Drug Deliv. Rev. 65 (2013) 689–702.

[9] E. Escalera, M.A. Ballem, J.M. Córdoba, M.-L. Antti, M. Odén, Powder Technol. 221 (2012) 359–364.

[10] D. Zhao, J. Feng, Q. Huo, N. Melosh, G.H. Fredrickson, B.F. Chmelka, G.D. Stucky, Science (80-.). 279 (1998) 548–552.

[11] a L. Doadrio, E.M.B. Sousa, J.C. Doadrio, J. Pérez Pariente, I. Izquierdo-Barba, M. Vallet-Regí, J. Control. Release 97 (2004) 125–32.

[12] G.D. Mihai, V. Meynen, M. Mertens, N. Bilba, P. Cool, E.F. Vansant, J. Mater. Sci. 45 (2010) 5786–5794.

[13] M. Van Speybroeck, V. Barillaro, T. Do Thi, R. Mellaerts, J. Martens, J. Van Humbeeck, J. Vermant, P. Annaert, G. Van den Mooter, P. Augustijns, J. Pharm. Sci. 98 (2009) 2648–2658.

[14] M. Moritz, M. Łaniecki, Appl. Surf. Sci. 258 (2012) 7523–7529.

[15] S.-Y. Park, P. Pendleton, Powder Technol. 223 (2012) 77–82.

[16] J.M. Rosenholm, A. Penninkangas, M. Lindén, Chem. Commun. (Camb). (2006) 3909–11.

[17] A. Atakan, P. Mäkie, F. Söderlind, J. Keraudy, E.M. Björk, M. Odén, Phys. Chem. Chem. Phys. 19 (2017) 19139–19149.

[18] A.D. Russell, M.J. Day, J. Hosp. Infect. 25 (1993) 229–238.

[19] A. Kovtun, D. Kozlova, K. Ganesan, C. Biewald, N. Seipold, P. Gaengler, W.H. Arnold, M. Epple, RSC Adv. 2 (2012) 870.

[20] T. Attin, T. Abouassi, K. Becker, A. Wiegand, M. Roos, R. Attin, Clin. Oral Investig. 12 (2008) 189–96.

[21] A.M. Young, P.Y.J. Ng, U. Gbureck, S.N. Nazhat, J.E. Barralet, M.P. Hofmann, Acta Biomater. 4 (2008) 1081–8.

[22] D. Karaman, D. Desai, R. Senthilkumar, E.M. Johansson, N. Råtts, M. Odén, J.E. Eriksson, C. Sahlgren, D.M. Toivola, J.M. Rosenholm, Nanoscale Res. Lett. 7 (2012) 358.

[23] D. Şen Karaman, S. Sarwar, D. Desai, E.M. Björk, M. Odén, P. Chakrabarti, J.M. Rosenholm, S. Chakraborti, J. Mater. Chem. B 4 (2016) 3292–3304.

[24] Y. Usami, T. Hongo, A. Yamazaki, J. Porous Mater. 19 (2011) 897–902.

[25] M. Hisbergues, S. Vendeville, P. Vendeville, J. Biomed. Mater. Res. - Part B Appl. Biomater. 88 (2009) 519–529.

[26] E. Asadpour, M.T. Boroushaki, A. Ghorbani, H.R. Sadeghnia, Iran. J. Pharm. Res. 13 (2014) 1141–1148.

[27] X. Wang, D. Chen, L. Cao, Y. Li, B.J. Boyd, R. a Caruso, ACS Appl. Mater. Interfaces 5 (2013) 10926–32.

[28] L.F. Chen, X.L. Zhou, L.E. Noreña, J. a. Wang, J. Navarrete, P. Salas, a. Montoya, P. Del Angel, M.E. Llanos, Appl. Surf. Sci. 253 (2006) 2443–2451.

[29] Á. Reyes-Carmona, A. Arango-Díaz, E. Moretti, A. Talon, L. Storaro, M. Lenarda, A. Jiménez-López, E. Rodríguez-Castellón, J. Power Sources 196 (2011) 4382–4387.

[30] J. Konieczny, Z. Rdzawski, Arch. Mater. Sci. Eng. 56 (2012) 53–60.

[31] G. Grass, C. Rensing, M. Solioz, Appl. Environ. Microbiol. 77 (2011) 1541–1547.

[32] L. Argueta-Figueroa, R.A. Morales-Luckie, R.J. Scougall-Vilchis, O.F. Olea-Mejía, Prog. Nat. Sci. Mater. Int. 24 (2014) 321–328.

[33] G. Borkow, J. Gabbay, R. Dardik, A.I. Eidelman, Y. Lavie, Y. Grunfeld, S. Ikher, M. Huszar, R.C. Zatcoff, M. Marikovsky, Wound Repair Regen. 18 (2010) 266–275.

[34] G. Borkow, S.S. Zhou, T. Page, J. Gabbay, PLoS One 5 (2010).

[35] A.K. Chatterjee, R. Chakraborty, T. Basu, Nanotechnology 25 (2014) 135101.

[36] N. Cioffi, L. Torsi, N. Ditaranto, G. Tantillo, L. Ghibelli, L. Sabbatini, T. Bleve-Zacheo, M. D'Alessio, P.G. Zambonin, E. Traversa, Chem. Mater. 17 (2005) 5255–5262.

[37] A. Esteban-Cubillo, C. Pecharromán, E. Aguilar, J. Santarén, J.S. Moya, J. Mater. Sci. 41 (2006) 5208–5212.

[38] J. Gabbay, J. Ind. Text. 35 (2006) 323–335.

[39] S. Jadhav, S. Gaikwad, M. Nimse, A. Rajbhoj, J. Clust. Sci. 22 (2011) 121–129.

[40] G. Ren, D. Hu, E.W.C. Cheng, M. a. Vargas-Reus, P. Reip, R.P. Allaker, Int. J. Antimicrob. Agents 33 (2009) 587–590.

[41] M. Raffi, S. Mehrwan, T.M. Bhatti, J.I. Akhter, A. Hameed, W. Yawar, M.M. Ul Hasan, Ann. Microbiol. 60 (2010) 75–80.

[42] R.J.B. Pinto, S. Daina, P. Sadocco, C.P. Neto, T. Trindade, Biomed Res. Int. 2013 (2013).

[43] S.P. Samuel, S. Li, I. Mukherjee, Y. Guo, A.C. Patel, G. Baran, Y. Wei, Dent. Mater. 25 (2009) 296–301.

[44] L. Wei, N. Hu, Y. Zhang, Materials (Basel). 3 (2010) 4066–4079.

[45] E.M. Johansson, M.A. Ballem, J.M. Cordoba, M. Oden, Langmuir 27 (2011) 4994–4999.

[46] M. Jaroniec, L.A. Solovyov, Langmuir 22 (2006) 6757–6760.

[47] S. Brunauer, P.H. Emmett, E. Teller, J. Am. Chem. Soc. 60 (1938) 309–319.

[48] A.L. Patterson, Phys. Rev. 56 (1939) 978–982.

[49] Y. Sultanbawa, a. Cusack, M. Currie, C. Davis, J. Rapid Methods Autom. Microbiol. 17 (2009) 519–534.

[50] T. Patton, J. Barrett, J. Brennan, N. Moran, J. Microbiol. Methods 64 (2006) 84–95.

[51] J.T. Casey, C. O'Cleirigh, P.K. Walsh, D.G. O'Shea, J. Microbiol. Methods 58 (2004) 327–334.

[52] T. López, O.-I. Emma, M. López, J. Flores, T. Corona, J. Nanomater.

Mol. Nanotechnol. 2 (2013) 2–7.

[53] S. Xin-Chao, D. Lin-Hai, W. Yu-Ye, Q. Wen-Guang, Y.-C. YU, W. Yuan, L. Huai-Lei, S. Zhao-Lin, S. Li-Juan, 28 (2012) 1467–1473.

[54] D. Zhao, Y. Wan, W. Zhou, in:, Ordered Mesoporous Mater., Wiley-VCH Verlag GmbH & Co. KGaA, 2013, pp. 219–242.

[55] S. Telalović, A. Ramanathan, J.F. Ng, R. Maheswari, C. Kwakernaak, F. Soulimani, H.C. Brouwer, G.K. Chuah, B.M. Weckhuysen, U. Hanefeld, Chem. - A Eur. J. 17 (2011) 2077–2088.

[56] K.S.W. Sing, Pure Appl. Chem. 54 (1982) 2201–2218.

[57] L. White, C. Tripp, J. Colloid Interface Sci. 232 (2000) 400–407.

[58] M.L. Martínez, M.B. Gómez Costa, G. a. Monti, O. a. Anunziata, Microporous Mesoporous Mater. 144 (2011) 183–190.

[59] E.M.G. Raso, M.E. Cortes, K.I. Teixeira, M.B. Franco, N.D.S. Mohallem, R.D. Sinisterra, J. Incl. Phenom. Macrocycl. Chem. 67 (2010) 159–168.

[60] a. Alizadeh, M.M. Khodaei, D. Kordestani, a. H. Fallah, M. Beygzadeh, Microporous Mesoporous Mater. 159 (2012) 9–16.

[61] M. Badea, R. Olar, M. Iliş, R. Georgescu, M. Călinescu, J. Therm. Anal. Calorim. (2012) 1763–1770.

[62] M. Călinescu, T. Negreanu-Pîrjol, R. Georgescu, O. Călinescu, Cent. Eur. J. Chem. 8 (2010) 543–549.

[63] B.V. Reddy, G.R. Rao, Indian J. Pure Appl. Phys. 46 (2008) 611–616.

[64] T. Tanaka, S. Murayama, N. Tuda, M. Nishiyama, K. Nakagawa, Y. Matsuo, Y. Isohama, Y. Kido, J. Heal. Sci. 51 (2005) 357–361.

[65] J. Coates, R. a M. Ed, Encyclopedia of Analytical Chemistry, John Wiley & Sons, Ltd, Chichester, UK, 2006.

[66] D. Luo, S. Shahid, R.M. Wilson, M.J. Cattell, G.B. Sukhorukov, ACS Appl. Mater. Interfaces 8 (2016) 12652–12660.

[67] P. Demuth, M. Hurley, C. Wu, S. Galanie, M.R. Zachariah, P. Deshong, Microporous Mesoporous Mater. 141 (2011) 128–134.

[68] J.B.S. Ng, P. Kamali-Zare, H. Brismar, L. Bergstr??m, Langmuir 24 (2008) 11096–11102.

[69] G. McDonnell, A.D. Russell, Clin. Microbiol. Rev. 14 (2001) 227–228.

[70] C.V.G. do Amorim, C.E. Aun, M.P.A. Mayer, Braz. Oral Res. 18 (2004) 242–246.

Supporting Information

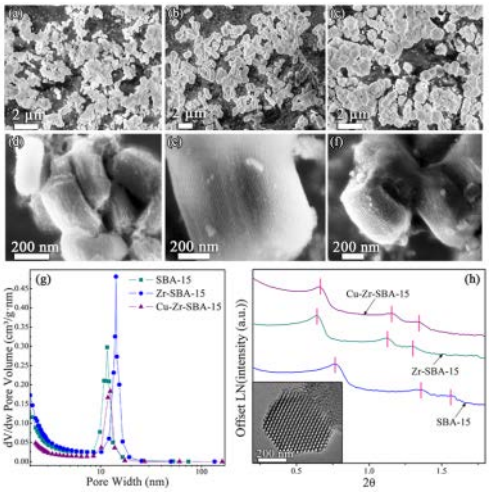

Figure S1. SEM micrographs of (a,d) SBA-15, (b,e) Zr-SBA-15, (c,f) Cu-Zr-SBA-15, at different magnification and, (j) Pore size distributions by N2 sorption, (k) SAXRD diffractograms with marks on the peaks and TEM micrograph of the cross-section of an SBA-15 particle.

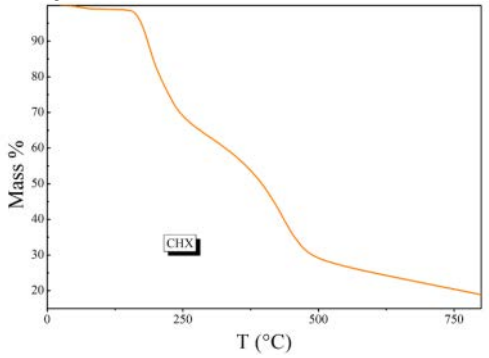

Figure S2. Thermogravimetric mass loss of pure CHX

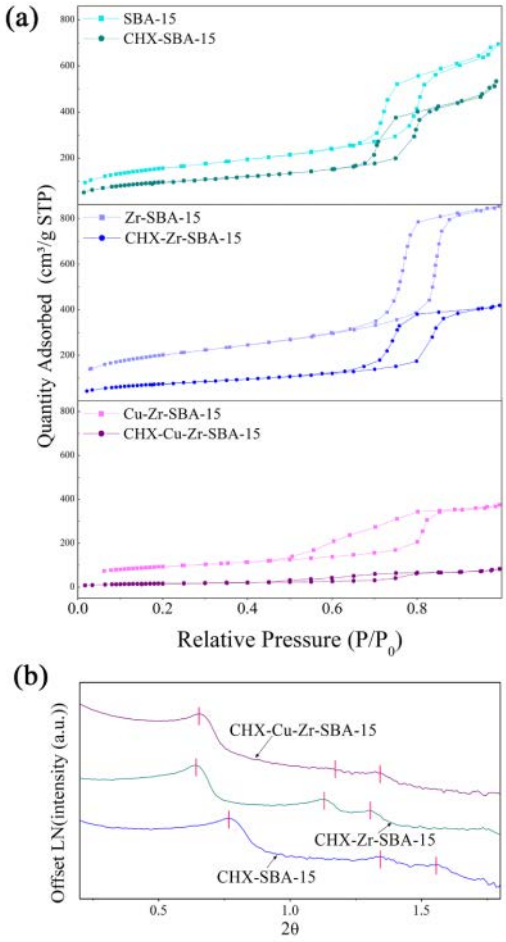

Figure S3. N_2 adsorption isotherms of the particles before and after CHX loading (a), and SAXRD of drug loaded samples (b).

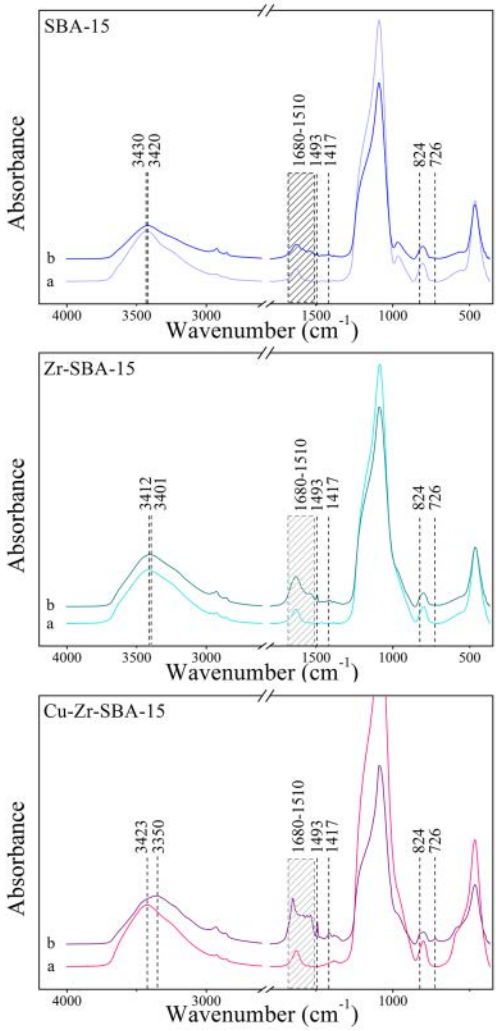

Figure S4. Normalized FTIR spectra of SBA-15, Zr-SBA-15 and Cu-Zr-SBA-15 with and without CHX loading ((a) drug loaded samples, (b) samples prior to drug loading)

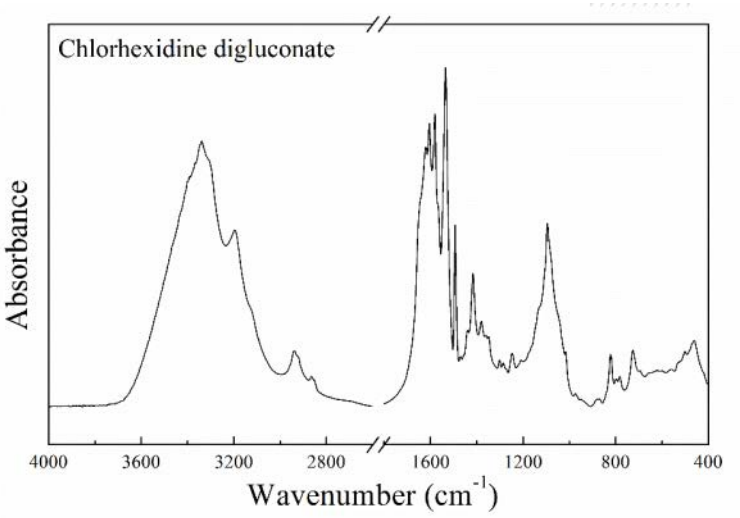

Figure S5. FTIR spectrum of CHX digluconate

Table S1. Pore characteristics of the drug carriers before and after the drug loading

Sample	SSA (m2/g)		Pore Volume* (cm3/g)		Micropore Volume (cm3/g)	
	Not loaded	CHX loaded	Not loaded	CHX loaded	Not loaded	CHX loaded
SBA-15	570	356	1.07	0.84	0.2	0
Zr-SBA-15	723	278	1.32	0.65	0.5	0
Cu-Zr-SBA-15	336	64	0.58	0.13	0.2	0

* Single point adsorption total pore volume of pores less than 289,7731 nm width at P/P0 = 0,993354442

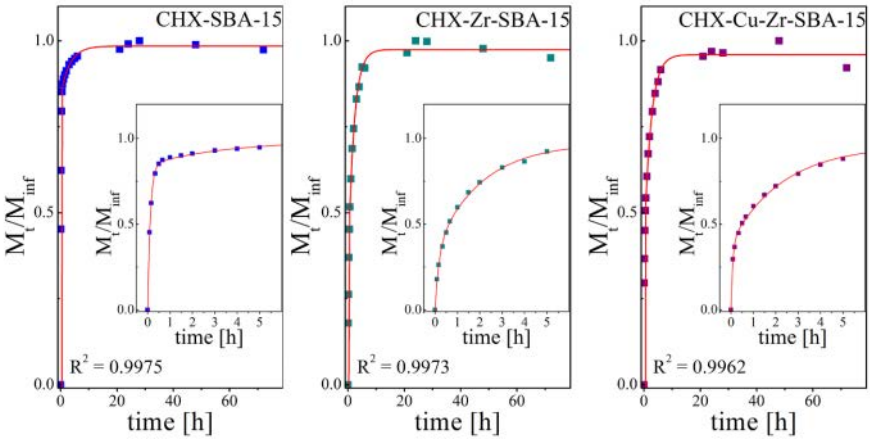

Figure S6. Fractional release as M_t/M_{inf} of CHX-SBA-15, CHX-Zr-SBA-15 and CHX-Cu-Zr-SBA-15 with the corresponding fitting curves (zoomed in the embedded graphs).

Paper 5

Tuning the pore size of a mesoporous carrier as means for control of antibiotic release

A. Atakan, C. Canal, P. Mäkie, M. Odén, and M. Ginebra

In manuscript

Tuning the pore size of a mesoporous carrier as means for control of antibiotic release

Aylin Atakan[a,b], Cristina Canal[b,c*], Peter Mäkie[a], Magnus Odén[a], and Maria-Pau Ginebra[b,c,d]

[a] *Nanostructured Materials, Department of Physics, Chemistry and Biology, Linköping University, Linköping SE-58183, Sweden.*

[b] *Biomaterials, Biomechanics and Tissue Engineering Group, Department of Materials Science and Metallurgy, Technical University of Catalonia (UPC), Av. Diagonal 647, 08028 Barcelona, Spain*

[c] *Barcelona Research Center in Multiscale Science and Engineering, Universitat Politècnica de Catalunya, Barcelona, Spain*

[d] *Institute of Bioengineering of Catalonia (IBEC) c/ Baldiri i Reixach 10-12, 08028 Barcelona, Spain*

**Corresponding author: email: cristina.canal@upc.edu*

SBA-15, pore size, doxycycline, drug delivery, antibacterial

ABSTRACT: Mesoporous silica is a bioactive material with favorable pore properties, which makes it attractive for applications in the biomedical field. In this study we employ SBA-15 with different pore sizes as a carrier for an antibiotic drug, doxycycline hyclate. We use the antibiotic as a model to evaluate the influence of porosity in the design of dosage forms. The influence of the pore size of SBA-15 is studied in terms of drug loading, drug release, and antibacterial activity. It was observed that the pore size is directly related to the drug loading amount as well as the fraction and amount of the drug released. The release profile is affected by the microporosity. During loading and release, the effects from interactions between the drug molecules and the SBA-15 support were small compared to drug-drug interactions, due to the large pore sizes compared to the size of the drug molecule. The antibacterial activity against staphylococcus aureus and Escherichia coli was observed to follow the drug release amounts.

1. INTRODUCTION

Since the discovery of mesoporous silica in 1990s [1,2], it has been of interest for application areas such as drug delivery, catalysis and adsorption[3,4]. This interest is due to their capacity for carrying and releasing molecules, e.g. drugs, in various sizes and shapes. One of the characteristics of mesoporous silica is that it can have high micro- and mesoporosity, which can collectively yield specific surface areas larger than 1000 m^2/g. Moreover, it typically has a narrow pore size distribution with tunable size. The framework of mesoporous silica is chemically and mechanically stable, bioactive and it allows chemical surface modifications. Among many types of mesoporous silica, SBA-15 has been studied extensively due to the fact that it possesses larger pores and thicker pore walls compared to the traditional mesoporous silica, MCM-41[4–7]. Moreover, the unidirectional pores of SBA-15 with the same cross-sectional diameter throughout the material facilitate good mass transfer of the load. Thus, SBA-15 is a candidate for drug encapsulation and has been reported as carriers for molecules such as ibuprofen, gentamicin, chlorhexidine etc[8].

Tuning the pore size of SBA-15 is a strategy to control drug loading and release in order to maintain the therapeutical level of the drug [9,10] for a chosen amount of time. However, it is not common to analyze the pore size effect in a large pore size range such as between 6 nm to 15 nm by maintaining the cylindrical pore shape and similar particle morphology. For example, a study was reported earlier for MCM-41 in terms of ibuprofen for a pore diameter range of 2.5-3.6 nm [11].

Nosocomial infections are still a battle field following open surgeries, for instance in bone applications. SBA-15 was earlier reported as a potential bone filler [12–14]. In this paper we report on the effect of the pore size of SBA-15 on the release of doxycycline hyclate (referred to as 'Doxy'). Doxy is an antibiotic utilized for bone and dental infections [15,16]. This paper elucidates the effect of SBA-15's most important textural property (pore size) in terms of loading and delivering drugs. For this purpose, a range of large pore sizes was synthesized with the same chemistry and their loading capacity and release profiles were evaluated.

2. MATERIALS AND METHODS

Poly(ethylene glycol)-block-poly(propylene glycol)-block-poly(ethylene glycol) (Pluronic P123, $EO_{20}PO_{70}EO_{20}$, av. M_n~5800, Aldrich), ammonium fluoride (NH_4F) (≥98.0%, Fluka), sodium chloride (NaCl) (≥99.8%, Sigma-Aldrich), HCl (≥37.0%, Sigma-Aldrich), heptane (99%, Sigma-Aldrich), tetraethyl orthosil-

icate (TEOS, 98%, Sigma-Aldrich), doxycycline hyclate (doxycycline hydrochloride hemiethanolate hemihydrate, MW:1025.89, Sigma-aldrich) were used as received.

Synthesis

SBA-15 was synthesized with three different pore sizes using two different versions of the self assembly method: the classical route [17] and a more rapid route [18]. The amounts of the chemicals used in the synthesis are listed in Table 1. According to the classical route, a micellar solution was prepared by stirring P123 in a HCl solution at 35 °C for at least 8 hours. Afterwards, the silica source (TEOS) was added to the micellar solution and stirred for 20 hours. Finally the maturation was achieved by hydrothermal treatment at 60 °C for 24 hours. The more rapid route, on the other hand, was conducted by stirring the micellar solution composed of P123 and NH_4F in a HCl solution and 28 mg NH_4F, at 20 °Cfor at least 3 hours. Upon full dissolution of P123, a mixture of TEOS and heptane was added into the micellar solution followed by 4 minutes of vigorous stirring and a static duration. For maturation, the solution was kept in an oven at 100°C for 24 hours. In the end, all the materials were calcined at 550 °C for 5 hours to remove the P123 from the pores.

Table 1. Synthesis conditions of different materials

Pore Size (route)	6.5 nm (classic route)	11.5 nm (rapid route)	14 nm (rapid route)
Sample name	PS6.5	PS11.5	PS14.0
Synthesis Parameters			
Micellar Solution			
Concentration of HCl in water and total volume	1.4 M - 80 mL	1.84 M - 80 mL	1.84 M - 80 mL
P123	2 g	2.4 g	2.4 g
NH_4F	-	28 mg	28 mg
Stirring temperature and time	35 °C overnight	20 °C until the polymer is fully dissolved (2-3 hours)	20 °C until the polymer is fully dissolved (2-3 hours)
Precursor Addition			
TEOS	4.25 mL	5.5 mL	5.5 mL
Heptane	-	1 mL	17 mL
Stirring temperature and time	35 °C for 20 hours	20 °C for 4 minutes	20 °C for 4 minutes
Static time	-	40 minutes	3 hours
Maturation (Hydrothermal Treatment)			
Temperature	60 °C	100 °C	100 °C
Time	24 hours	24 hours	24 hours

Characterization

Scanning Electron Microscopy (SEM) (LEO 1550 Gemini operated at 3 kV) and Transmission Electron Microscopy (TEM) (FEI Tecnai G2 operated at 200 kV and using carbon coated copper grids as sample holder) were used for imaging the particle morphology.

A Micromeritics ASAP 2020 device was employed for measuring N_2 physisorption isotherms. The pore size distribution was obtained by the Kruk-Jaroniec-Sayari (KJS) method [19] and the specific surface area (SSA) at P/P_0 between 0.08 and 0.16 by the the Brunauer-Emmet-Teller (BET) method [20]. The internal SSA (pore surface area) was calculated by subtracting the external SSA from SSA and external SSA was obtained by t-plot method at P/P_0 between 0.24-0.54 corresponding to 0.46-0.68 nm film thickness of adsorbed N_2.

The pore packing structure of the mesoporous framework was investigated by small angle x-ray diffractometry (SAXRD) using a Panalytical Empyrean equipped with Cu Kα x-ray source operated at 45 kV and 40 mA in line focus. The results of SAXRD measurements were employed to calculate unit cell parameter (d-spacing), which was later used together with the pore size to obtain the wall thickness of the SBA-15 frameworks.

2.1. Drug loading

The drug-loading procedure included dispersion of 20 mg of mesoporous particles in a 50 mg/mL doxycycline hyclate solution by 1 minute vortexing followed by 30 minutes in an ultrasonic bath. The suspensions were resuspended again by vortexing and then agitated by an IKA KS 260 basic orbital shaker for ~3.5 hours at 50 rpm. Finally, the drug-loaded powders were recovered by centrifugation where the supernatant was collected, and the materials were freeze-dryed.

Drug loading was taken as the weight difference of the particles before and after the described procedure.

Fourier-transform infrared spectroscopy (FTIR) was used to investigate the drug attachment to the mesoporous framework. For this, a Bruker Vertex 70 spectrometer equipped with a water-cooled MIR source and a DLaTGS detector was used. Spectra were acquired with 2 cm^{-1} resolution and each spectrum is the average of 16 scans. The peak areas were calculated following a baseline correction.

2.2. Drug release

The *in vitro* drug release tests were performed by immersing 1 mg of drug loaded SBA-15 sample into 1 mL of phosphate buffer saline (PBS) in an eppendorf. Independent samples were employed for each time point. All the eppendorfs were sealed tight, then loaded on floating micro-centrifuges and placed in water filled beakers to allow for the release experiments to perform the at 37 °C whilst mildly stirring. At each time point the powder and the liquid in this eppendorf were centrifuged and the drug concentration in the receptor media was measured by UV spectroscopy analysis at 351 nm wavelength using a Microplate Reader (TECAN Infinite H200 Pro Microplate Reader). Three replicates were studied for each sample. The final concentration values were used to calculate the cumulative release % (the released drug amount/total amount of loaded drug), released drug amount M_t (mg Doxy/mg carrier) and M_t/M_{inf} (M: mg Doxy/mg carrier) where M_t is the amount of drug in the solution at a specific time t, and M_{inf} is the maximum amount of drug released after infinite time. These values are graphically presented vs. time. The released percentage value after infinite time was approximated with the value recorded for the sample with the longest release time. At this point the (cumulative) released value had reached the stationary stage.

The release kinetics were evaluated by fitting a mathematical function to the M_t/M_{inf} vs. time plot using the MATLAB® software.

2.3. Antibacterial activity

The drug-loaded samples were tested against two common bacteria in nosocomial infections. i.e. *Staphylococcus aureus* (CCUG 15915) and *Escherichia coli* (CECT 101) by agar diffusion tests. Such test determines the effectiveness of a diffusible anti-microbial agent to inhibit bacterial growth. For preparation of the culture

media, 15 g/l agar bacteriological (Scharlau, ref.no. 07-004-500) and 37 g/l brain heart infusion (Scharlau, ref.no. 02-599-500) were dissolved in 1liter water and then sterilized by autoclaving. The test was performed by seeding the bacteria uniformly on the petri dishes. The samples for this test were prepared by weighing 0.5 mg of a drug-loaded SBA-15 powder into an eppendorf and filling it with 0.5 mL PBS. Then 50 µL of these solutions were carefully dropped on the prepared agar plates at different areas and they were then incubated at 37 °C for 24 hours. Each drop caused a spherical inhibition zone and the diameters of these apertures were measured in terms of pixels by the aid of an Adobe® Photoshop software and then converted to mm. The reported result is the average inhibition zone obtained from three test areas for the each sample.

2.4. Statistics

The overall statistical differences between test groups were analyzed by applying Tukey's post hoc method via one way ANOVA (Minitab 16 software, Minitab Inc., USA) with 95% significance level.

3. RESULTS and DISCUSSIONS

Materials chemistry

In this study, two methods were employed to obtain SBA-15 with large but different pore sizes which are a classical high-temperature self-assembly route and a low-temperature rapid self-assembly route. The influence of pore size is investigated for Doxycycline incorporation and release from SBA-15. The classical high temperature synthesis, conducted at 35° C, yielded a particle morphology of mono-dispersed platelets (Figure 1(a)) with a pore size of 6.5 nm (Table 2). The platelet morphology is a result of using a long static time during the synthesis [17,18]. In the low-temperature rapid route heptane was used as swelling agent[21] to obtain two different pore sizes (11.5 and 14 nm) by adding 1 or 17 mL of heptane to the synthesis solution, see Table 2. These two samples (PS11.5 and PS14.0), have rod morphology and the same pore length as PS6.5, i.e. the length of the PS11.5 and PS14 rods are the same as the thickness of the PS6.5 platelets. The difference between the two morphologies is seen in the diameters of the circular cross-section of the particles (D), which is smaller for the rods (Table 2 and Figure 1(a-c)). Keeping the pore length constant is important for this study as it has been shown that pore length can be a crucial variable for the access of a drug molecule in and out of the pores[22]. The physisorption properties of all the SBA-15 materials prepared here reveal a narrow pore size distribution with a type IV isotherm and a type 1 hysteresis loop (Figure 1(d)). This is typical for mesoporous materials with open cylindrical pores[23]. According to the SAXRD results, all the synthesized SBA-15 frameworks were observed to have a hexagonal pore packing order indicated by the 100, 110 and 200 diffraction lines (Figure 1(e)). The hexagonal packing order suggests the pores to be parallel to each other, which enables easy access of molecules to be adsorbed.

The physical properties of the synthesized SBA-15 materials such as specific surface area (SSA), pore volume (PV), micro-pore volume (µ-PV), particle diameter, and wall thickness (nm) are presented in Table 2. The thickness of the pore walls increases as the pore size decreases. Consequently, the microporosity is largest for the smallest pore size, i.e. the µ-PV of PS6.5 was observed to be almost double of that of PS11.5 and PS14. Micropores (pores smaller than 2 nm[24]) are important since small drug molecules can also be accommodated in the micropores, so this parameter is expected to affect the drug loading and release characteristics.

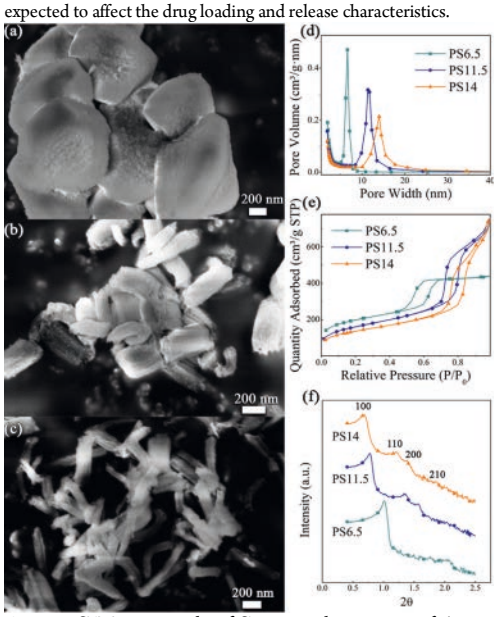

Figure 1. SEM micrographs of SBA-15 with pore sizes of 6.5 nm (PS6.5) **(a)**, 11.5 nm (PS11.5) **(b)**, and 14 nm (PS14.0) **(c)**, pore size distributions **(d)**, BET isotherms **(e)** and small angle x-ray diffractograms (SAXRD) **(f).**

Table 2. Physical properties of the produced SBA-15 materials.

Sample name	Pore size (nm)	SSA (m^2/g)	PV (cm^3/g)	µ-PV (cm^3/g)	Particle diameter	Wall thickness (nm)
PS6.5	6.5	706	0.68	0.134	1 µm	3.6
PS11.5	11.5	584	1.16	0.064	150 nm	1.7
PS14.0	14.0	495	1.18	0.059	90 nm	0.8

Drug Loading

The ordered cavities within the material are expected to act as reservoirs for relatively high amounts of the drug, which in this study is doxycycline. The amount of drug loaded is presented as a function of pore size in Figure 2.

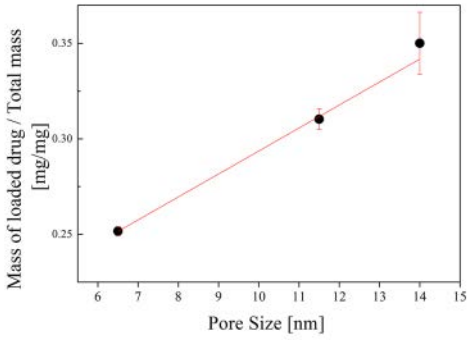

Figure 2. Relative amount of drug loaded as function of the pore size. Different symbols (*, **, and ***) indicate statistically significant differences.

The loading capacity of the mesoporous carrier increases with increasing pore size while SSA and μ-PV increase do not seem to favor the loading capacity.

FTIR measurements of the mesoporous carrier before and after being loaded with Doxy are presented in Figure 3. The characteristic peaks of the mesoporous material are detected at 3400 cm^{-1} (OH), 1627 cm^{-1} (water deformation), 1240 cm^{-1} (δH_2O), 1086 cm^{-1}, 800 and 465 cm^{-1} (Si-O-Si), and 960 cm^{-1} (Si-OH) [10,25–27]. The Doxy peaks are concentrated between 1700-1300 cm^{-1}, except for O-H and N-H band contribution to the wide H_2O peak at 3400 cm^{-1} [28,29]. These spectra confirm the presence of Doxy in the three cases.

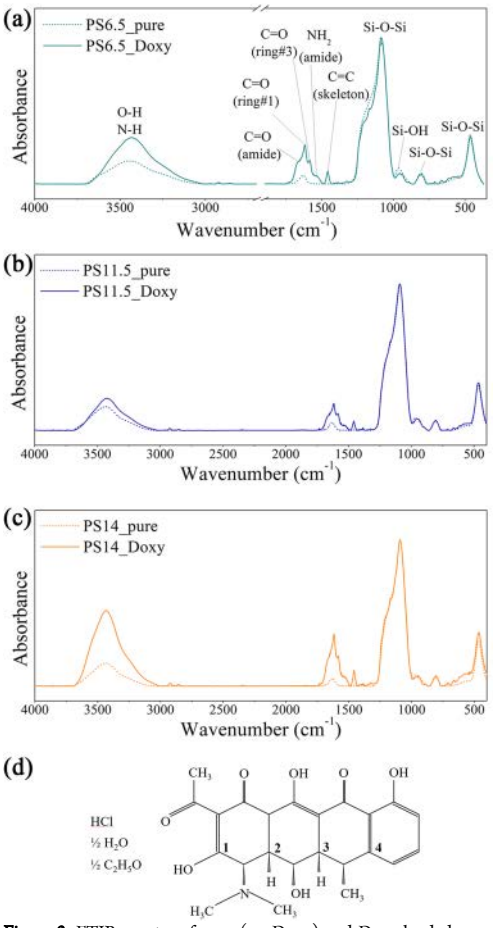

Figure 3. FTIR spectra of pure (no Doxy) and Doxy loaded samples: (a) PS6.5, (b) PS11.5, and (c) PS14. (d) shows the chemical structure of doxycycline hyclate (Doxy).

Drug Release

Figure 4(a) shows the cumulative release percentage of Doxy from the three mesoporous carriers. All the carriers display a burst release during the first hour, which is more significant for PS11.5 & PS14.0 than PS6.5. Instead, carrier PS6.5 displays a more restricted release. All the drug content is released from PS14 by the time it reaches the stationary stage, whereas PS11.5 has released ~86% and PS6.5 ~76% of its initial Doxy content within the same timeframe which appears to be a function of the pore size (Fig. 4b). This is attributed to the increasing μ-PV with decreasing pore size resulting in some drug molecules being trapped in the micropores. Doxy is a low molecular weight drug and its size is estimated to be between 1.5-2 nm based on bond length values [30]. Hence, some Doxy molecules are expected to be trapped in the micropores (or diffuse slower), which have a size of 2 nm or less.

We also note that all samples have completed their release within 1-2 hours, which is too fast for most medical applications and the release system needs to be improved such that a slower release rate is achieved. However, this system displays an improved and slower release profile compared to earlier studies where a similar mesoporous silica (MCM-41) released all its Doxy content in the first 10 minutes in a similar PBS solution [28]. Our results show that the pores are easily accessible for the receptor media, and therefore the exchange of drug from the material is favorable. Future strategies may consider capping or partial blocking of the pores, chemical gate keeping at the pore openings, and enhancing the chemical interactions between the drug and the substrate to better control the drug release.

The total amount of Doxy released (M_t) decreases with decreasing pore size, i.e. $M_{t,PS6.5} < M_{t,PS11.5} < M_{t,PS14}$ (Figure 4(a)). This is expected based on the decreasing pore volume with decreasing pore size, which is magnified by the decreasing fraction of the loaded drug released as the pore size decreases (insert in Fig. 4b). This indicates that the drug release was only affected by the pore size. In contrast to previously studied materials[15], the release does not follow the trend of the SSA. The specific surface changes following $SSA_{PS6.5} > SSA_{PS11.5} > SSA_{PS14}$, while the release has the opposite trend. Moreover, the release trend as a function of the pore size (Figure 4(b)) is similar to the trend of the drug loading (Figure 2). These observations indicate that in this system drug-carrier interactions are weak, which is also confirmed by the fast release recorded. Consequently, the amount of drug released is proportional to the amount of drug loaded.

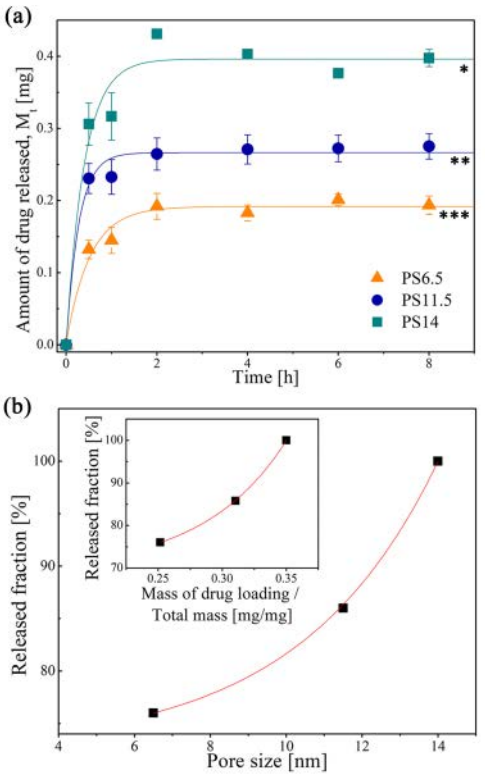

Figure 4. Amount of drug released, M_t[mg] vs. time [h] **(a),** and released fraction of Doxy [%] vs pore size and vs. mass of drug loading / mass of support [mg/mg] **(b)**. Different symbols (*, **, ***) indicate statistically significant differences.

The release of the drug, Mt as a function of time can be described by a function that takes into account both a burst release (through diffusion) and a self-rate-limiting stage (slow out-leaching)[31]. Equation (1) has previously been shown to describe the release process well for SBA-15 mesoporous systems.

$$\frac{M_t}{M_{inf}} = P_1(1 - e^{-k_1 t}) + P_2(1 - e^{-k_2 t}) \quad (1)$$

where M_{inf} is the amount drug released after infinite time (here approximated with M_{8h} where the stationary stage has already been reached), P_1 and P_2 are the fraction of drug released during stage one and two, and k_1 and k_2 are the rate constants during the two stages. Equation (1) is then fitted to the experimental data to yield the following relationships for the different samples as shown in Eq (2,3, and 4). In all three cases the self-rate-limiting step has been detected very low and thus almost all the release was observed to be diffusion-controlled, i.e. P_1=1 and P_2=0 .

PS6.5 $$\frac{M_t}{M_{inf}} = (1 - e^{-1.69t}) \quad (2)$$

PS11.5 $$\frac{M_t}{M_{inf}} = (1 - e^{-3.12t}) \quad (3)$$

PS14 $$\frac{M_t}{M_{inf}} = (1 - e^{-1.94t}) \quad (4)$$

According to the release rates of the different carriers, k_1, were observed to follow the order of $k_{1,PS6.5} < k_{1,PS14} < k_{1,PS11.5}$ which interestingly does not correlate to any of the structural parameters presented in Table 2, instead it is reversely related to the drug loading per pore volume values which are 0.51, 0.40 and 0.50 for PS6.5, PS11.5 and PS14, respectively. This indicates that when there is a higher drug concentration (drug amount per volume) in a carrier, a tighter packing of the drug molecules can be observed which intensifies inter-molecular interactions. As a result, the release becomes slower. This can be attributed to the fact that the drug-drug interactions dominate this system whereas drug-carrier interactions remain unaffected.

Antibacterial Activity

The antibacterial activity of the drug-loaded carriers was tested against *Staphylococcus aureus* and *Escherichia coli* (Figure 5) given their incidence in nosocomial infections. The inhibition zones were observed to follow the trend of the release amount released drug M_t and the pore size for both bacteria. The controls indicate no antibacterial activity of empty carriers, i.e. SBA-15 materials without being loaded with Doxy. The inhibition zones were clean in the case of *Escherichia coli* while they contained some colonization in case of *Staphylococcus aureus*. This suggests a higher activity for *Escherichia coli*, which is attributed to the higher minimum inhibitory concentration of Doxy against *Staphylococcus aureus* compared to *Escherichia coli*[32].

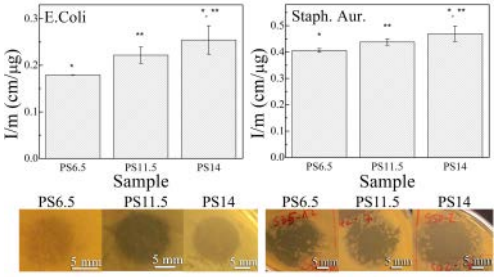

Figure 5. Inhibition zone size I (cm) graph normalized to the mass of nanoparticles tested and sample images of PS6.5, PS11.5 and PS14 against staphylococcus aureus and escherichia coli. Different symbols (*, **) indicate statistically significant differences.

4. CONCLUSIONS

In this study, an antibiotic of use in bone and dental infections, doxycycline hyclate, was loaded into SBA-15 mesoporous supports with the same chemistry. The influence of the supports' pore size on loading and release performance was evaluated. The pore size directly affects the drug loading and released amount of the drug. All carriers display a burst release profile, which can be controlled by the pore size. The drug showed antibacterial efficiency upon loading and inhibition was proportional to the pore size, and thus the released amount.

AUTHOR INFORMATION

Corresponding Author

* E-mail: cristina.canal@upc.edu

Notes

The authors declare no competing financial interest.

ACKNOWLEDGMENT

This work was financially supported by EU's Erasmus-Mundus program: The European School of Materials - Doctoral Programme - DocMASE; MINECO, through Project MAT2015-65601-R, co-funded by the EU through European Regional Development Funds, and Ramon y Cajal fellowship of CC; Support for the research of MPG was received through the "ICREA Academia" prize for excellence in research, funded by the Generalitat de Catalunya.

REFERENCES

(1) Beck, J. S.; Vartuli, J. C.; Roth, W. J.; Leonowicz, M. E.; Kresge, C. T.; Schmitt, K. D.; Chu, C. T. W.; Olson, D. H.; Sheppard, E. W. A New Family of Mesoporous Molecular Sieves Prepared with Liquid Crystal Templates. *J. Am. Chem. Soc.* **1992**, *114* (27), 10834–10843.

(2) Kresge, C. T. Leonowicz, M. E.Roth, W. J.Vartuli, J.Beck, J. S. C. Ordered Mesoporous Molecular Sieves Synthesized by a Liquid-Crystal Template Mechanism. *Nature* **1992**, *359* (6397), 710–712.

(3) Alothman, Z. A Review: Fundamental Aspects of Silicate Mesoporous Materials. *Materials (Basel).* **2012**, *5* (12), 2874–2902.

(4) Moritz, M.; Geszke-Moritz, M. Mesoporous Materials as Multifunctional Tools in Biosciences: Principles and Applications. *Mater. Sci. Eng. C* **2014**, *49*, 114–151.

(5) Zhao, D.; Feng, J.; Huo, Q.; Melosh, N.; Fredrickson, G. H.; Chmelka, B. F.; Stucky, G. D. Triblock Copolymer Syntheses of Mesoporous Silica with Periodic 50 to 300 Angstrom Pores. *Science (80-.).* **1998**, *279* (5350), 548–552.

(6) Doadrio, A. L.; Sousa, E. M. B.; Doadrio, J. C.; Pérez Pariente, J.; Izquierdo-Barba, I.; Vallet-Regí, M. Mesoporous SBA-15 HPLC Evaluation for Controlled Gentamicin Drug Delivery. *J. Control. Release* **2004**, *97* (1), 125–132.

(7) Mihai, G. D.; Meynen, V.; Mertens, M.; Bilba, N.; Cool, P.; Vansant, E. F. ZnO Nanoparticles Supported on Mesoporous MCM-41 and SBA-15: A Comparative Physicochemical and Photocatalytic Study. *J. Mater. Sci.* **2010**, *45* (21), 5786–5794.

(8) Izquierdo-Barba, I.; Martinez, A.; Doadrio, A. L.; Pérez-Pariente, J.; Vallet-Regí, M. Release Evaluation of Drugs from Ordered Three-Dimensional Silica Structures. *Eur. J. Pharm. Sci.* **2005**, *26* (5), 365–373.

(9) Vallet-Regí, M.; Balas, F. Silica Materials for Medical Applications. *Open Biomed. Eng. J.* **2008**, *2*, 1–9.

(10) Raso, E. M. G.; Cortes, M. E.; Teixeira, K. I.; Franco, M. B.; Mohallem, N. D. S.; Sinisterra, R. D. A New Controlled Release System of Chlorhexidine and Chlorhexidine:βcd Inclusion Compounds Based on Porous Silica. *J. Incl. Phenom. Macrocycl. Chem.* **2010**, *67* (1–2), 159–168.

(11) Horcajada, P.; Rámila, A.; Pérez-Pariente, J.; Vallet-Regí, M. Influence of Pore Size of MCM-41 Matrices on Drug Delivery Rate. *Microporous Mesoporous Mater.* **2004**, *68* (1–3), 105–109.

(12) Fullriede, H.; Timpe, N.; Borchers, L.; Stiesch, M.; Menzel, H.; Behrens, P.; Chemie, A.; Hannover, L. U.; Chemie, T.; Braunschweig, T. U.; Prothetik, Z. A NTIBACTERIAL SILICA NANOPARTICLES WITH P H-SENSITIVE RELEASE PROPERTIES AS FILLERS FOR DENTAL DENTA L COMPOSITE MATERIALS. **2013**, *58*, 9–10.

(13) Samuel, S. P.; Li, S.; Mukherjee, I.; Guo, Y.; Patel, A. C.; Baran, G.; Wei, Y. Mechanical Properties of Experimental Dental Composites Containing a Combination of Mesoporous and Nonporous Spherical Silica as Fillers. *Dent. Mater.* **2009**, *25*, 296–301.

(14) Wei, L.; Hu, N.; Zhang, Y. Synthesis of Polymer—Mesoporous Silica Nanocomposites. *Materials (Basel).* **2010**, *3* (7), 4066–4079.

(15) Canal, C.; Pastorino, D.; Mestres, G.; Schuler, P.; Ginebra, M.-P. Relevance of Microstructure for the Early Antibiotic Release of Fresh and Pre-Set Calcium Phosphate Cements. *Acta Biomater.* **2013**, *9* (9), 8403–8412.

(16) Caton, J. G.; Ciancio, S. G.; Blieden, T. M.; Bradshaw, M.; Crout, R. J.; Hefti, a F.; Massaro, J. M.; Polson, a M.; Thomas, J.; Walker, C. Subantimicrobial Dose Doxycycline as an Adjunct to Scaling and Root Planing: Post-Treatment Effects. *J. Clin. Periodontol.* **2001**, *28* (8), 782–789.

(17) Sayari, A.; Han, B. H.; Yang, Y. Simple Synthesis Route to Monodispersed SBA-15 Silica Rods. *J. Am. Chem. Soc.* **2004**, *126* (44), 14348–14349.

(18) Johansson, E. M.; Ballem, M. A.; Cordoba, J. M.; Oden, M. Rapid Synthesis of SBA-15 Rods with Variable Lengths, Widths, and Tunable Large Pores. *Langmuir* **2011**, *27* (8), 4994–4999.

(19) Jaroniec, M.; Solovyov, L. A. Improvement of the Kruk–Jaroniec–Sayari Method for Pore Size Analysis of Ordered Silicas with Cylindrical Mesopores. *Langmuir* **2006**, *22* (16), 6757–6760.

(20) Brunauer, S.; Emmett, P. H.; Teller, E. Adsorption of Gases in Multimolecular Layers. *J. Am. Chem. Soc.* **1938**, *60* (2), 309–319.

(21) Johansson, E. M.; Córdoba, J. M.; Odén, M. The Effects on Pore Size and Particle Morphology of Heptane Additions to the Synthesis of Mesoporous Silica SBA-15. *Microporous Mesoporous Mater.* **2010**, *133* (1–3), 66–74.

(22) Wang, Y.; Zhang, F.; Wang, Y.; Ren, J.; Li, C.; Liu, X.; Guo, Y.; Guo, Y.; Lu, G. Synthesis of Length Controllable Mesoporous SBA-15 Rods. *Mater. Chem. Phys.* **2009**, *115*, 649–655.

(23) Sing, K. S. W. Reporting Physisorption Data for Gas/solid Systems with Special Reference to the Determination of Surface Area and Porosity (Provisional). *Pure Appl. Chem.* **1982**, *54* (11), 2201–2218.

(24) McCusker, L. B.; Liebau, F.; Englehardt, G. Nomenclature of Structural and Compositional Characteristics of Ordered Microporous and Mesoporous Materials with Inorganic Hosts (IUPAC Recommendations 2001): Physical Chemistry Division Commision on Colloid and Surface Chemistry Including Catalysis. *Microporous Mesoporous Mater.* **2003**, *58* (1), 3–13.

(25) White, L.; Tripp, C. Reaction of (3-Aminopropyl)dimethylethoxysilane with Amine Catalysts on Silica Surfaces. *J. Colloid Interface Sci.* **2000**, *232* (2), 400–407.

(26) Martínez, M. L.; Gómez Costa, M. B.; Monti, G. a.; Anunziata, O. a. Synthesis, Characterization and Catalytic Activity of AlSBA-3 Mesoporous Catalyst Having Variable Silicon-to-Aluminum Ratios. *Microporous Mesoporous Mater.* **2011**, *144* (1–3), 183–190.

(27) Alizadeh, a.; Khodaei, M. M.; Kordestani, D.; Fallah, a. H.; Beygzadeh, M. The Successful Synthesis of Biguanide-Functionalized Mesoporous Silica Catalysts: Excellent Reactivity Combined with Facile Catalyst Recyclability. *Microporous Mesoporous Mater.* **2012**, *159*, 9–16.

(28) Petrescu, M.; Mitran, R. A.; Luchian, A. M.; Matei, C.; Berger, D. Mesoporous Ceria-Silica Composites as Carriers for Doxycycline. *UPB Sci. Bull. Ser. B Chem. Mater. Sci.* **2015**, *77* (3), 13–24.

(29) Silva, H. F. O.; Lima, K. M. G.; Cardoso, M. B.; Oliveira, J. F. a.; Melo, M. C. N.; Sant'Anna, C.; Eugênio, M.; Gasparotto, L. H. S.

Doxycycline Conjugated with Polyvinylpyrrolidone-Encapsulated Silver Nanoparticles: A Polymer's Malevolent Touch against Escherichia Coli. *RSC Adv.* **2015**, *5* (82), 66886–66893.

(30) Legendre, A. O.; Silva, L. R. R.; Silva, D. M.; Rosa, I. M. L.; Azarias, L. C.; de Abreu, P. J.; de Araujo, M. B.; Neves, P. P.; Torres, C.; Martins, F. T.; Doriguetto, A. C. Solid State Chemistry of the Antibiotic Doxycycline: Structure of the Neutral Monohydrate and Insights into Its Poor Water Solubility. *Crystengcomm* **2012**, *14* (7), 2532–2540.

(31) Ng, J. B. S.; Kamali-Zare, P.; Brismar, H.; Bergstr??m, L. Release and Molecular Transport of Cationic and Anionic Fluorescent Molecules in Mesoporous Silica Spheres. *Langmuir* **2008**, *24* (19), 11096–11102.

(32) Cunha, B. A.; Domenico, P.; Cunha, C. B. Pharmacodynamics of Doxycycline. *Clin. Microbiol. Infect.* **2000**, *6* (5), 270–273.

Supporting Information

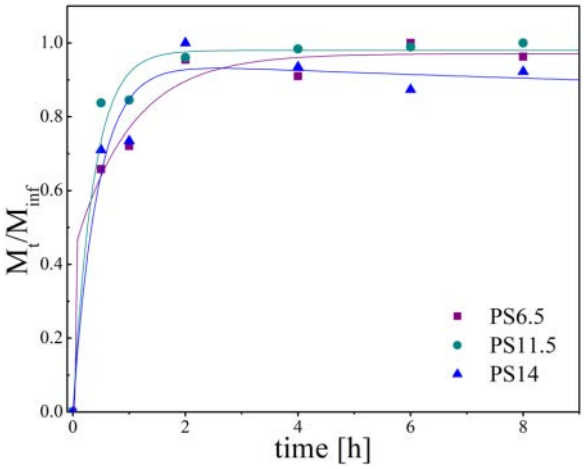

Figure S1. M_t/M_{inf} vs. time (scatter graph) and the fitting curves